RELATIONSHIP BETWEEN ELECTRON DELOCALIZATION AND ASYMMETRY OF THE PAIR DISTRIBUTION FUNCTION AS DETERMINED BY X-RAY ABSORPTION SPECTROSCOPY

by

SCOTT CALVIN

A dissertation submitted to the Graduate Faculty in Physics in partial fulfillment of the requirements for the degree of Doctor of Philosophy, The City University of New York

2001

This manuscript has been read and accepted for the Graduate Faculty in Physics in satisfaction of the dissertation requirement for the degree of Doctor of Philosophy.

6/30/01 — Date

Chair of Examining Committee

6/30/01 — Date

Executive Officer

Supervisory Committee:

Marten denBoer

Steven Greenbaum

Azzam Mansour

Lou Massa

THE CITY UNIVERSITY OF NEW YORK

ABSTRACT

RELATIONSHIP BETWEEN ELECTRON DELOCALIZATION AND ASYMMETRY OF THE PAIR DISTRIBUTION FUNCTION AS DETERMINED BY X-RAY ABSORPTION SPECTROSCOPY

by

Scott Calvin

Adviser: Professor Marten denBoer

Electron delocalization, whether over an entire solid or a local environment of a few atoms, contributes to many macroscopic properties of materials, including conductivity, malleability, ductility, optical properties, and chemical reactivity. Despite its importance, few existing techniques can directly determine the degree of delocalization within a particular bond. In this work, it is hypothesized that, for otherwise similar systems, asymmetry in the pair distribution function (PDF) as determined by extended x-ray absorption fine structure (EXAFS) spectroscopy is correlated to the degree of electron delocalization.

The accuracy of using EXAFS curve-fitting with theoretical standards to determine the asymmetry of the PDF is first established by finding thermal expansion,

harmonic Debye-Waller factor, and EXAFS third cumulant for two FCC metals, nickel and copper. The results yield a temperature dependence that agrees well with theory, although the third cumulant shows an offset that indicates that absolute values determined by this method are not reliable. Fortunately, only relative values, which appear to be quite accurate, are necessary for exploring the hypothesis presented.

The technique is then used to find the bond responsible for the semiconductor-metal transition of titanium sesquioxide, to establish the presence of charge-transfer in solid iodine, and to rank the relative amount of stabilizing charge available to the carbon-bromine bond of butyl bromide isomers. In the latter case, the role of hyperconjugation and the inductive effect is discussed. In all cases, the EXAFS third cumulant is found to increase with increasing electron delocalization for systems that are otherwise similar.

General considerations of EXAFS analysis are also discussed, including background subtraction, constraint schemes for multiple-scattering paths, the effects of the finite and discrete Fourier transforms used, and the effects of sample inhomogeneity.

ACKNOWLEDGEMENTS

This dissertation would not have been possible without the help, support, and advice of many people. First among them is my adviser, Marten denBoer, who encouraged me to take my idea and explore it to the fullest, and then provided the support (scientific and otherwise!) to do just that. The other members of the Hunter College X-Ray Spectroscopy Group, including Svilen Kostov, Jihane Mimih, Theanne Schiros, Mike Benjamin, John Ciannella, Adama Diene, Todd Horne, Roman Iskhakov, Vitaly Kishinyovsky, Hershie Mehta, Mike Rivlin, Jason van Sluytman, Marc Bacuyag, David Lipton, Jackson Lin, and James Waters, were likewise invaluable: they prepared samples, collected and analyzed data, and provided key insights into the issues I have explored. At the National Synchrotron Light Source, Johnny Kirkland, Erik Nelson, Zugen Fu, and Joe Woicik answered countless late-night phone calls when a monochromator was stuck or a key not turned; when they could not diagnose the problem over the phone, they came in person.

Of course, I would not be conducting scientific research at all if I had not come to Hunter College. Hunter has provided an extraordinarily supportive and vibrant environment. A very few of the people who helped make it that way: Steve Greenbaum, Bob Marino, Pam Mills, Marilyn Rothschild, and Bill Sweeney.

At the Graduate Center of the City University of New York, a few professors stand out as excellent teachers. Professors Diem, Ferrari, Gunner, Koplik, Pollak, and Tomkiewicz make coursework interesting, relevant, and accessible.

Five years as a graduate student, with little money and less free time, would make it easy to lose touch with the larger world. I thank my family and friends for grounding

me, providing encouragement, and understanding each time I dropped out of sight for a while. My parents have both been through this themselves, and gave me sage advice and lots of love. My siblings, Duif, Kris, and Bufo each supported me in their own unique way. Kristine Barbieri, whom I met as an undergraduate at Berkeley, led by example, and Eric Goodman, whom I have known for much longer, always lent a sympathetic ear and an insightful word. Finally, many thanks to Janna, who gave me just what I needed when I needed it: support, distraction, inspiration, and love.

TABLE OF CONTENTS

Chapter 1: Electron Delocalization 1
1.1 Introduction 1
1.2 Macroscopic Manifestations of Electron Delocalization 2
1.3 Microscopic Forms of Electron Delocalization 4
1.4 Survey of Experimental Determinations of Electron Delocalization 8

Chapter 2: Electron Delocalization and Asymmetry of the Pair Distribution Function 11

Chapter 3: EXAFS Spectroscopy 16
3.1 Theory 16
3.1.1 X-ray Absorption Spectroscopy 16
3.1.2 Background 17
3.1.3 EXAFS 19
3.2 Experimental 21
3.3 Analysis: The Curve-Fitting Method 25
3.3.1 Approximate Atomic Positions for Model Compound 30
3.3.2 Model EXAFS Using FEFF/Model of Paths in K-Space 30
3.3.3 Collect and Average Data Over All Scans 30
3.3.4 Subtract Background/Convert Data to K-Space 31
3.3.5 Fourier Transform Data and Model to R-Space 32
3.3.6 Perform Least-Squares Refinement of Model to Data 32
3.3.7 Check Fit for Stability and Physical Sense 34
3.4 Cumulant Expansion 35
3.5 Sources of Error 37
3.6 Statistics of the Curve-Fitting Method 39
3.7 Radial Asymmetry Parameter 45

Chapter 4: Accuracy of Cumulant Determinations by EXAFS Curve-Fitting 46
4.1 Temperature Dependence of EXAFS Cumulants 46
4.2 Data 49
4.3 Analysis and Constraints 56
4.4 Results 57
4.5 Comparison to Theory 68
4.6 Validity of the Cumulants Determined by the Curve-Fitting Method 73

Chapter 5: Titanium-Sesquioxide: A Semiconductor-Metal Transition 74
5.1 Structure 74
5.2 Experimental 75
5.3 Analysis 78
5.4 Results 91

Chapter 6: Iodine: Charge Transfer **96**
6.1 Structure and Properties 96
6.2 Experimental—Vapor 96
6.3 Analysis—Vapor 99
6.4 Results—Vapor 102
6.5 Experimental—Solid 102
6.6 Analysis—Solid 104
6.7 Results—Solid 113
6.8 Comparison of Vapor and Solid Results 114

Chapter 7: Butyl Bromides: Delocalization Within Molecules **116**
7.1 Structure and Electronic Delocalization 116
7.2 Experimental 118
7.3 Analysis 120
7.4 Results 129

Chapter 8: Conclusions **132**

Appendix A: Fourier Transforms **137**
A.1 Fourier transforms of finite, discrete data sets 137
A.2 Windowing 141
A.3 k-Weighting 143
A.4 Statistical Effect of Windowing and k-Weighting 144
A.5 Suggestions for future development 144

Appendix B: Sample Preparation **146**

Appendix C: Multiple Scattering **152**
C.1 Multiple Scattering Paths and Constraints 152
C.2 Assumptions 153
C.3 Classification and Constraints for Multiple-Scattering Paths 153
C.3.1 Double 154
C.3.2 Conjoined 154
C.3.3 Focused 155
C.3.4 Triangle 155
C.3.5 Flattened 157
C.3.6 Reverse 158
C.3.7 Other path types 158

Appendix D: Using K-Dependence to Reduce Correlations **159**

Bibliography **163**

LIST OF FIGURES

Figure 1.1: Charge transfer 5
Figure 1.2: Charge transfer for ions 5
Figure 1.3: 1,3-butadiene 6
Figure 1.4: Lewis structure of 1,3-butadiene 6
Figure 1.5: Benzene 7
Figure 1.6: Ethyl carbocation 7
Figure 1.7: Hyperconjugation 8
Figure 2.1: Typical interatomic potential 14
Figure 2.2: Typical pair distribution function 14
Figure 3.1: XAS spectral features 17
Figure 3.2: XAS experimental schematic 22
Figure 3.3: Schematic of curve-fitting method of EXAFS analysis 29
Figure 4.1: XANES of elemental metals: a) nickel at 100 K; b) copper at 200 K. 50
Figure 4.2: Background for elemental metals: a) nickel at 100 K; b) copper at 200 K 52
Figure 4.3: *k*-space spectra of elemental metals with *k*-weight 3: a) nickel; b) copper 53
Figure 4.4a: Low-*k* peak of nickel spectra 55
Figure 4.4b: High-*k* peak of nickel spectra 55
Figure 4.5: Fit for elemental copper at 250 K 62
Figure 4.6: Temperature dependence of nearest-neighbor nickel cumulants 71
Figure 4.7: Temperature dependence of nearest-neighbor copper cumulants 72
Figure 5.1: Corundum structure 74
Figure 5.2: Ti_2O_3 XANES at 392 K 78
Figure 5.3: Ti_2O_3 background at 392 K 79
Figure 5.4: *k*-space spectra of Ti_2O_3 with *k*-weight 3 86
Figure 5.5a: Low-*k* peak of Ti_2O_3 spectra 87
Figure 5.5b: High-*k* peak of Ti_2O_3 spectra 87
Figure 5.6: Real part of the Fourier transform of Ti_2O_3 data 89
Figure 5.7: Fit of 392 K Ti_2O_3 91
Figure 5.8. Radial asymmetry parameter for axial titanium-titanium bond in Ti_2O_3 93
Figure 6.1a: L edges of iodine vapor 98
Figure 6.1b: L_{III} edge of iodine vapor 98
Figure 6.2: Background subtraction for iodine vapor 99
Figure 6.3: *k*-space spectrum for iodine vapor with *k*-weight 1 100
Figure 6.4: Fit of iodine vapor 101
Figure 6.5: 120 K solid iodine L_I edge 103
Figure 6.6: Background for 120 K solid iodine 104
Figure 6.7: *k*-space spectra of solid iodine with *k*-weight 1 109

Figure 6.8: Real part of Fourier transform of solid iodine data 110
Figure 6.9a: Fit of iodine solid at 120 K 112
Figure 6.9b: Fit of iodine solid at 220 K 112
Figure 6.10: Temperature dependence of bond length in solid iodine 114
Figure 6.11: Radial asymmetry parameter in iodine 115
Figure 7.1: Isomers of butyl bromide 117
Figure 7.2: White line of *n*-butyl bromide spectra 119
Figure 7.3: Background for *t*-butyl bromide 120
Figure 7.4: Unweighted *k*-spectra for butyl bromide spectra 124
Figure 7.5: *k*-spectra for butyl bromide spectra with *k*-weight 2 125
Figure 7.6: Real part of Fourier transform of butyl bromide data 126
Figure 7.7: Butyl bromide fits 128
Figure A.1: a) Discrete Fourier transform of $\chi(k) = \cos\left(3\frac{2\pi k}{\Delta k}\right)$; b) Backtransform 140
Figure A.2: a) Discrete Fourier transform of $\chi(k) = \cos\left(3.5\frac{2\pi k}{\Delta k}\right)$; b) Backtransform .. 140
Figure A.3: a) Discrete Fourier transform of $\chi(k) = \cos\left(3\frac{2\pi k}{\Delta k}\right)$ padded with zeroes; b) Backtransform 141
Figure A.4: a) Discrete Fourier transform of $\chi(k) = \cos\left(3\frac{2\pi k}{\Delta k}\right)$ padded with zeroes and windowed with a Hanning function; b) Backtransform 142
Figure A.5: Discrete Fourier transform of $\chi(k) = \cos\left(3\frac{2\pi k}{\Delta k}\right)$ padded with zeroes and windowed with a Gaussian function; b) Backtransform 143
Figure C.1: Double multiple-scattering path 154
Figure C.2: Conjoined multiple-scattering path 154
Figure C.3: Focused multiple-scattering path 155
Figure C.4: Triangle multiple-scattering path 155
Figure C.5: Flattened multiple-scattering path 157
Figure C.6: Reverse multiple-scattering path 158
Figure D.1: Correlation chart for S_o^2 vs. nearest-neighbor second cumulant (nickel) 162

LIST OF TABLES

Table 4.1: Scattering paths for elemental nickel 58
Table 4.2a: Statistical quality of elemental nickel fits 63
Table 4.2b: Statistical quality of elemental copper fits 63
Table 4.3a: Results for fits of elemental nickel. 65
Table 4.3b: Results for fits of elemental copper. 66
Table 4.4a: Morse potential parameters for elemental nickel 69
Table 4.4b: Morse potential parameters for elemental copper 69
Table 5.1: Ti_2O_3 temperatures 77
Table 5.2: Model for Ti_2O_3 80
Table 5.3: Scattering paths for Ti_2O_3. 81
Table 5.4: Quality of Ti_2O_3 fit 90
Table 5.5: Results of Ti_2O_3 fit 92
Table 5.6: Results of alternate Ti_2O_3 fit 94
Table 6.1: Results of iodine vapor fit. 102
Table 6.2: Model for solid iodine 105
Table 6.3: Scattering paths for solid iodine. 106
Table 6.4: Statistical quality of solid iodine fits 111
Table 6.5: Results of solid iodine fit 113
Table 7.1: Bond dissociation energies for alkyl bromides 118
Table 7.2: Scattering paths for butyl bromides 122
Table 7.3: Statistical quality of butyl bromide fits 127
Table 7.4: Results of butyl bromide fits. 129

Chapter 1

ELECTRON DELOCALIZATION

1.1 Introduction

Physicists, chemists, engineers, and materials scientists often refer to "electron delocalization," but this label actually covers a rich variety of phenomena, both on the microscopic and macroscopic levels. For example, an electrical engineer might think of electrons in a conduction band, while an organic chemist might think of hyperconjugation or the inductive effect. In the first case, electric charge may move on a scale of meters or more, while in the latter case, electron mobility is limited to atoms a few Angstroms apart. Is there a single empirical tool that can be used to probe all of these phenomena? I believe the answer is yes; in this work, I demonstrate an experimental technique that is sensitive to, and gives similar results for, electron delocalization on a wide variety of scales.

One use of the term "electron delocalization" will *not* be covered by this technique, however. As electrons are fundamentally indistinguishable, it is technically not possible to specify the wave function of each individual electron within a material in a unique way. Solid state physicists often take advantage of this to express electron density in terms of Bloch functions, in which the wave functions of even core electrons are expressed in terms of wave functions that spread throughout the material.

With the exception of this solid state terminology (not used in the remainder of this work), electron delocalization concerns the ability of the electron wave function to distort in response to a change in conditions. If, in response to a small perturbation, electron density in the vicinity of one atom increases and another decreases, then there

are delocalized electrons present. The stimulus could be an externally imposed electric field, as in metallic conduction, or the stretching of a bond, as in chemical delocalization. Although this interpretation motivates the use of a single term, it does not address whether the various phenomena are the same or merely analogous. Do conductors that respond to external electric fields also respond to the stretching of an individual bond? Similarly, do the electrons that stabilize carbocations also respond to external electric fields? Often, the answers seem to be yes. Metals, for example, are ductile because of the ability of electrons to respond to local distortions of the lattice. Likewise, chemists extending delocalization from the molecular to the macroscopic scales when they synthesize organic conductors [1]. If all forms of delocalization share common properties, then a single technique should be capable of probing the degree of delocalization present.

In this work, I first describe the phenomena of delocalization on both a microscopic and macroscopic level. Next, I discuss how EXAFS spectroscopy can be used to probe electron delocalization. Finally, I describe the results of experiments using this technique on a wide variety of materials. Details of the analysis are included in the appendices.

1.2 Macroscopic Manifestations of Electron Delocalization

Macroscopic manifestations of electron delocalization include:

- **Conductivity**: if electron delocalization extends across an entire material, then an externally applied electric field can cause a current to flow. Although conductivity is always an indication of electron delocalization, there may be delocalization on some scale without conductivity. As an extreme example,

consider two cubes of copper 10 cm on a side separated by a piece of paper. Although little or no current can be made to flow from one side of the device to the other (under moderate fields), it is clear that the overwhelming majority of the material contains delocalized electrons. Similarly, electrons may be delocalized on an interatomic scale and yet not be macroscopically delocalized. For example, benzene molecules contain six electrons that are almost completely delocalized within the molecule, and yet benzene is an insulator because electrons are not free to jump from one molecule to the next. In fact, unlike in the example of the copper blocks and the paper separator, the *entire* volume of a benzene sample contains delocalized electron wave functions of significant amplitude, and yet the sample does not conduct.

- **Ductility**: If electrons are free to flow between neighboring bonds, then the stretching of a bond can be stabilized by electron density donated from elsewhere. If sufficient density is available for atoms that define the structural backbone of the material, then the material can be pulled out into wires. Again, although ductility is generally symptomatic of some degree of electron delocalization, it is not a necessary consequence of delocalization. To again use benzene as an example, consider the solid form. Although distortions of individual benzene molecules should be enhanced by the electron delocalization, this has no effect on the interactions between molecules. Thus, benzene cannot be formed into wires, even at temperatures at which it is a solid.

- **Malleability**: This phenomenon is similar to ductility, except it is more closely related to distortions perpendicular to the bond than to bond stretching (although the distortion of the lattice that results necessitates some stretching as well).
- **Optical effects**: If electrons are able to respond to high-frequency electric fields, then the material will reflect electromagnetic radiation at that frequency. This ability is clearly enhanced by electron delocalization. In addition, electron delocalization can clearly enhance the dielectric constant of a material, and thus increase its index of refraction.
- **Reactivity**: To the chemist, the main interest in electron delocalization is in its effect on reaction rates and pathways, and perhaps on molecular structure. For example, why do carbocations form over a million times more rapidly from tertiary alkyl halides in water than the primary form [2]? Why is benzene so much more stable than cyclohexane (or 1,3,5-hexatriene)? Unlike the other macroscopic effects given above, which are strong indicators of delocalization, reactivity is influenced by many factors, and delocalization can either enhance or suppress a particular reaction. Thus, although delocalization is an important concept for a chemist trying to explain the properties of a reaction, the role that it plays and the degree to which it is present is sometimes a matter of controversy for many years [3].

1.3 Microscopic Forms of Electron Delocalization

Although the basic properties of electron delocalization on a microscopic scale are generally similar, they may conveniently be grouped into several categories:

- **Metallic**: electron delocalization over a macroscopic chain, net, or lattice of atoms. This generally results in conductivity, although if the delocalization is over chains, the presence of even occasional defects will destroy the conductivity. With this definition, metallic conductivity may occur without the presence of metal atoms, as in organic conductors.
- **Charge transfer**: in ionic compounds, electrons are transferred between neighboring atoms to form charged ions. In molecular compounds, individual molecules are held together by a variety of intermolecular attractions (such as dipole-dipole, London dispersion, and hydrogen bonding forces). In neither case is it necessary for electron delocalization to occur. If, however, an ionic compound type transfer is only partial, it is possible for the electrons to be delocalized over the donating and accepting atoms. This is sometimes indicated by the following Lewis diagram:

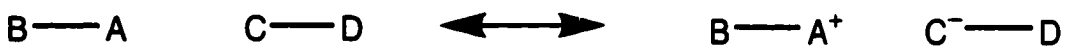

Figure 1.1: Charge transfer

In this case, an electron is delocalized over atoms A and C. This kind of delocalization is known as *charge transfer* [4]. It is also possible to have charge transfer in which both of the resonance structures are charged, e.g.:

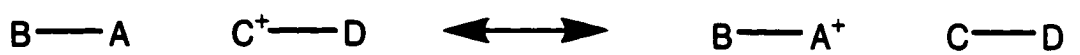

Figure 1.2: Charge transfer for ions

- **Conjugation**: When neighboring π-orbitals overlap and there is only one electron available per orbital, a *conjugated* system is created in which the electrons are delocalized over all of the orbitals. For example, consider 1,3-butadiene:

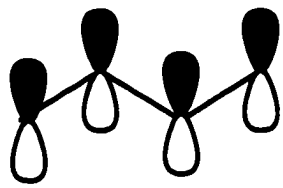

Figure 1.3: 1,3-butadiene

Four electrons occupy the depicted π-orbitals, and thus are delocalized across the entire molecule. This is somewhat awkward to depict with Lewis structures, although this is one possibility:

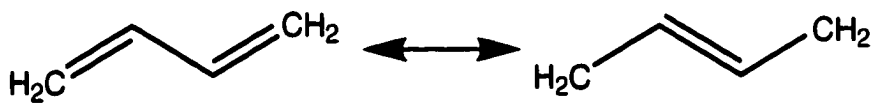

Figure 1.4: Lewis structure of 1,3-butadiene

This kind of delocalization is primarily noteworthy for its stabilizing effect.

- **Aromaticity**: A conjugated ring system with $4n + 2$ delocalized electrons (n an integer) is referred to as *aromatic*. Aromatic systems are particularly stable. Benzene is the archetype of an aromatic compound:

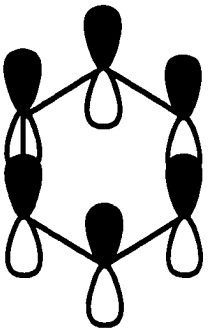

Figure 1.5: Benzene

- **Inductive Effect**: transfer of electron density through polarization of σ-bonds.

  For example, consider the ethyl carbocation:

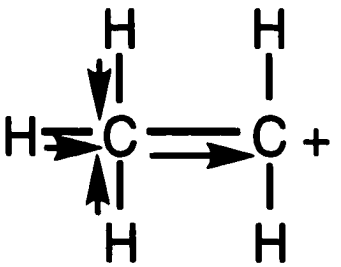

Figure 1.6: Ethyl carbocation

Since carbon is more electronegative than hydrogen, the C-H bonds on the neutral carbon deposit a small excess of negative charge on the carbon. This in turn polarizes the C-C bond. In effect, a small amount of electron density is transferred from the hydrogens to the carbocation through the medium of the σ-bonds. This causes the carbocation to be slightly more stable than it would otherwise be, and the hydrogens to be slightly more acidic (i.e. they have lowered electron density). Since this effect can be enhanced or suppressed by

changing the conditions (e.g. by solvation), it fits the description of electron delocalization given above, and is often described in those terms.

- **Hyperconjugation**: transfer of electron density because of overlap of σ-bonding orbitals. Consider again the ethyl carbocation:

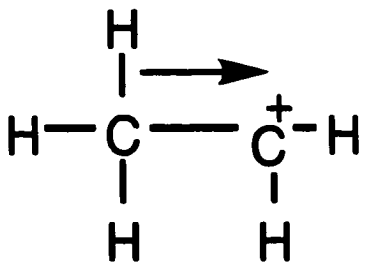

Figure 1.7: Hyperconjugation

In this mechanism, overlap of the C-H bond with the empty orbital on the neighboring carbon provides stabilization. Thus, both hyperconjugation and the inductive effect contribute to the stabilization of carbocations with alkyl substituents [3].

The above list is meant to be representative, rather than exhaustive. For example, three-center bonds, in which a two-electron wave function is the sole bond between an aggregation of three atoms, also represent a variety of electron delocalization.

1.4 Survey of Experimental Determinations of Electron Delocalization

In this section, I will briefly mention some of the experimental tools used to determine electron delocalization, along with their areas of application and limitations:

- **Conductivity measurements** provide information on whether macroscopically delocalized electrons are present. For single crystals, anisotropic conductivity can give clues to the bonds involved in delocalization. Temperature-dependent measurements of semiconductors can give considerable information on the band structure of the material, which, in combination with theoretical band-structure calculations, yields additional information on the structure of the delocalization. Conductivity measurements, however, give little or no information about delocalization on the sub-macroscopic scale (such as conjugation, aromaticity, charge transfer, the inductive effect, and hyperconjugation).
- **Nuclear magnetic resonance**. This form of spectroscopy can yield some information on the presence of delocalized electrons in the vicinity of nuclei with favorable gyromagnetic ratios. This information is generally quite indirect, since the effect is minor compared to the effect, for example, of reduced electron density on the resonant nucleus.
- **Microwave, infrared, and Raman spectroscopies**. These spectroscopies can yield considerable information in the gas phase, where spectra are relatively easy to interpret. In solids, however, the complex splitting introduced by the phonon spectrum often makes assignments difficult. The stabilization related to conjugation and aromaticity can often be detected, but this is only indirectly related to electron delocalization.

- **Visible and ultraviolet spectroscopies.** These spectroscopies yield accurate bond energies, which allow stabilization to be determined. Stabilization is, however, only indirectly related to electron delocalization.

In summary, no existing experimental technique can determine in which bonds electron delocalization is occurring over a wide range of substances. Delocalization must instead be deduced from theoretical measures such as band structure calculations, *ab initio* quantum mechanical computations, and proposed reaction mechanisms. When these theoretical predictions agree with other measurable aspects of the system, it is reasonable to believe that the conclusions reached regarding delocalization are also valid. Nevertheless, a relatively direct experimental probe of delocalization is clearly desirable.

Chapter 2

ELECTRON DELOCALIZATION AND ASYMMETRY OF THE PAIR DISTRIBUTION FUNCTION

In this section, I will discuss how electron delocalization can often be detected as an increase in the asymmetry of the pair distribution function (PDF), and I will introduce a technique for detecting that asymmetry.

For simplicity, begin by considering an isolated diatomic molecule, as in a gas. In this case, an unambiguous interatomic potential can be graphed by plotting potential energy as a function of atomic separation, with infinite separation being assigned the value zero. Without needing to know any details of this potential, it must have certain features:

- The potential must go to zero as the separation approaches infinity (using the conventional choice for the zero of potential)
- The potential must increase asymptotically as the separation approaches zero, both because complete overlap of the electron wave functions is prohibited by the Pauli exclusion principle, and because of Coulomb repulsion between the nuclei. These factors are collectively referred to as *hard core repulsion.*
- There must be a minimum (or minima) of the interatomic potential, since otherwise the bond could not be stable.
- Because of the asymptotic behavior, the potential cannot be symmetric about any value of the separation, including the value corresponding to the minimum potential.

- Because of the Heisenberg uncertainty relationship between position and momentum, the lowest energy eigenstate must be at a somewhat higher energy than the minimum of the interatomic potential.

See Figure 2.1 (page 14) for a typical potential fulfilling these requirements.

Although a harmonic potential may be an appropriate approximation to such a potential for many applications, it is highly unlikely to be completely accurate in any real diatomic molecule. Unlike the harmonic potential, the actual interatomic potential is inherently asymmetric (as can be seen from the asymptotic behavior). A Taylor series expansion about the minimum could certainly give harmonic behavior at that point, but even the ground state must be at a somewhat higher energy, assuring that anharmonic terms are needed for a complete description.

In more complicated systems, a precise definition of interatomic potential becomes problematic. If the separation between two atoms in a solid is increased, for example, other atoms will shift as well. A phonon description is thus more accurate than a description in terms of pair potentials.

Nevertheless, pair potential models are easy to conceptualize and lend themselves well to the interpretation of certain experimental data (such as EXAFS, the tool used in this work). In cases where interactions between certain pairs of atoms are particularly strong compared to the background field of the lattice (e.g. when covalent bonds are involved), the accuracy of the description is increased. In the case of iodine solid, for example, the interaction between the covalently bond pairs of atoms can be reasonably well described by a pair potential.

In any case, accurate effective pair potentials will have some anharmonicity, because the gross qualitative features of the diatomic gas potential described above will still be present: asymptotically large potential energy at low separation, asymptotically small potential energy at high separation (in the extreme limit, this corresponds to vaporizing the solid), and a ground state energy somewhat above the minimum of the potential. Indeed, without anharmonicity there would be no thermal expansion [5].

How would the availability of delocalized electrons modify the effective pair potential? For bonds shorter than the equilibrium length, there would be very little effect: only valence electrons can be delocalized, so the hard core repulsion would be unchanged. For bonds longer than the equilibrium length, however, electron density would be available to compensate for the lengthening of the bond. The effective interatomic potential would thus be reduced at separations above the minimum (see Figure 2.1), indicating that it would be easier to stretch the bond than would be otherwise possible. Thus, stretching would be enhanced over compression and the anharmonicity increased. A probability distribution for the separation (the pair distribution function or PDF) would thus be skewed more toward the positive side, as in Figure 2.2. If this asymmetry in the PDF could be detected, it would serve as a marker for electron delocalization.

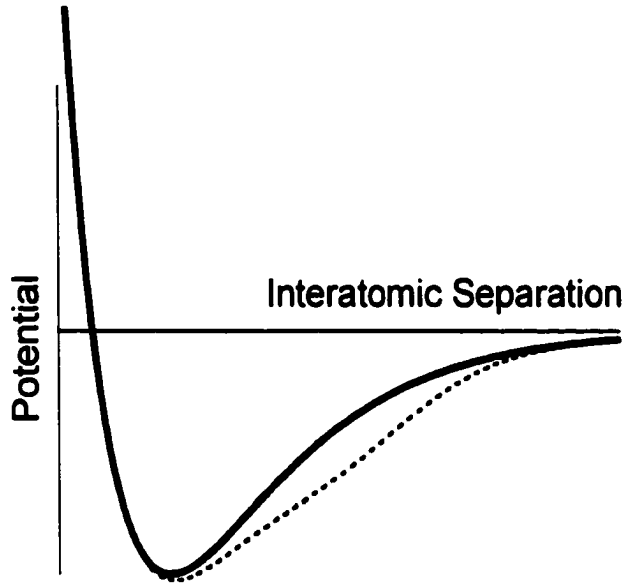

Figure 2.1: Typical interatomic potential. The dashed line shows the qualitative effect of electron delocalization.

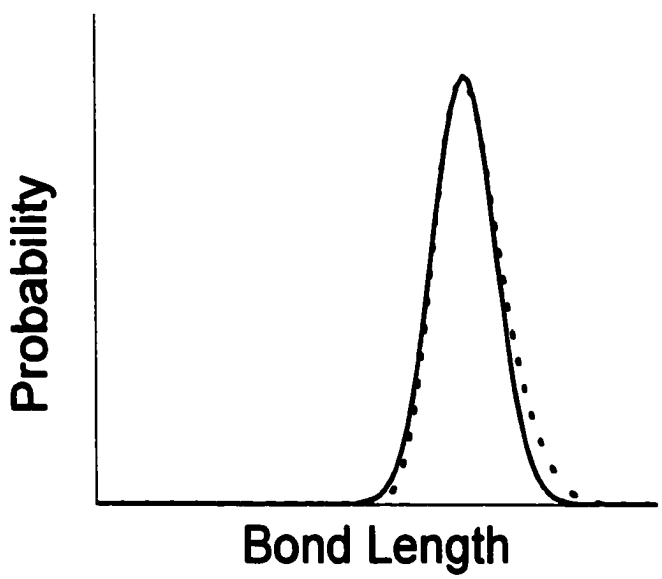

Figure 2.2: Typical pair distribution function. Dashed line shows effect of electron-delocalization.

Real solids are not perfectly crystalline; because of defects of various sorts, corresponding atom pairs in different unit cells will not have exactly identical equilibrium separations. This *static disorder* will also be affected by electron delocalization; electron delocalization will help stabilize distances that are greater than the mean, but will not stabilize distances short enough to involve substantial hard core repulsion. This does not mean that electron delocalization will necessarily increase the mean separation; rather, the PDF will have a longer positive tail and a shorter negative tail than a Gaussian with the similar mean and variance. (Figure 2.2).

Both the anharmonicity and the static disorder are thus impacted in a similar fashion by static disorder, with the primary effect being an increase in the skew of the PDF.

In the next section, I will examine the relationship between EXAFS and the PDF, focussing particularly on the ability of EXAFS to detect PDF skews of this type.

Chapter 3

EXAFS SPECTROSCOPY

3.1 Theory

3.1.1 X-ray Absorption Spectroscopy

In x-ray absorption spectroscopy (XAS), the absorption of a sample is measured as a function of x-ray energy. Over much of the energy range, the absorption decreases with increasing energy, smoothly and monotonically. When the photon energy approaches the energy necessary to lift a core electron of an element present in the sample above the Fermi level, the absorption jumps markedly (typically by a factor of 2-10 for K-shell electrons); this is known as an *absorption edge* of that element. Superimposed on that basic structure are features that vary rapidly with energy. They are generally classified as *pre-edge*, *edge*, *near-edge* (*x-ray absorption near edge structure*, or XANES), and *extended x-ray absorption fine structure* (EXAFS). See Figure 3.1 for examples of these features. Features in regions other than EXAFS are generally due to intra-atomic transitions, particularly those which are dipole-forbidden (the lowest allowed transition will be responsible for the edge itself). XANES features are best defined as those spectral features above the edge energy that are caused by intra-atomic transitions. For experimental purposes, however, the XANES region is often considered to extend some fixed amount of energy above the edge (often 30 eV).

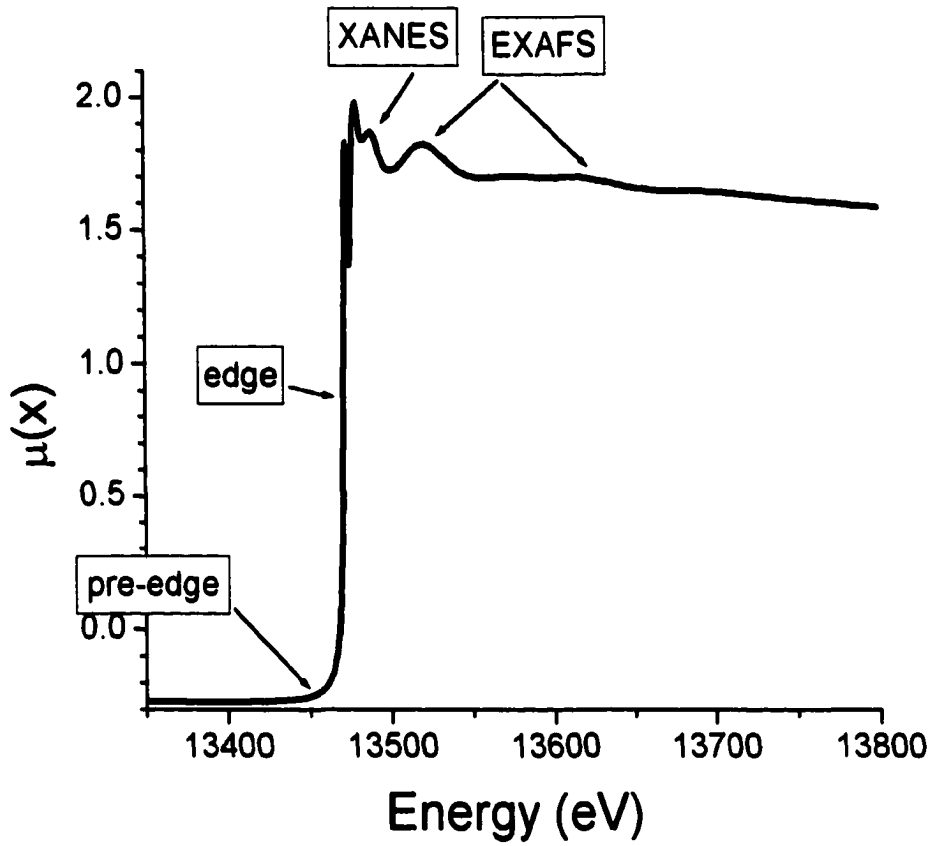

Figure 3.1: XAS spectral features

3.1.2 Background

Since EXAFS comprises features that vary rapidly in energy, it is necessary to subtract or divide by a slowly varying background function. Accurate theoretical calculations of backgrounds have not yet been developed, and a theoretical calculation would in any case necessitate chemical knowledge of all the materials in the path of the x-ray beam (such as windows); therefore, it is necessary to use an empirical technique. Unfortunately, the background is due primarily to two mechanisms: absorption by electrons other than those responsible for the edge (either other electrons in the same element, or electrons in other elements; taken together, I will refer to this as the *extrinsic* background) and the slowly-

varying portion of the absorption due to the electrons responsible for the edge (I will refer to this as the *intrinsic* background). Because absorption by a core electron of the target element and absorption by some other mechanism are mutually exclusive events, background subtraction is appropriate for the extrinsic background. For the intrinsic background, on the other hand, the EXAFS is a modulation of the smoothly varying absorption of the core electron in quest. The magnitude of the EXAFS therefore scales with the magnitude of the intrinsic background, and division by this background is the appropriate method for isolating the EXAFS. For division to be meaningful, however, absorption must be measured on a ratio scale (so that there is a true zero). Subtraction merely requires a difference scale; using this scheme, the absorption may be shifted by any convenient amount and still yield the same EXAFS signal. In the typical XAS experiment, such offsets are present (see section 3.2); thus subtraction is more likely to yield a consistent result from one experiment to the next. The EXAFS signal $\chi(k)$, where k is the wave number of the photoelectron, is therefore defined by:

$$\chi(k) = \frac{\mu(k) - \mu_o(k)}{\Delta\mu_o(0)} \tag{3.1}$$

In this equation, $\mu(k)$ is the total absorption, $\mu_o(k)$ is the background, and $\Delta\mu_o(0)$ is a normalization equal to the amount by which the background absorption jumps at the edge. (The normalization is necessary to compensate for different concentrations of the absorbing element.)

When following this procedure, $\chi(k)$ shows a systematic error because the intrinsic background has been handled incorrectly. Fortunately, this part of the background is fully transferable for a given shell of a given element, since, except for a slight shift in energy, it is almost completely insensitive to the chemical environment. In

addition, the background subtraction and normalization procedure outlined produces a ratio scale with a true zero, regardless of offsets present in the original signal (any offsets are subtracted out). Thus, division by the intrinsic background of the absorbing element can be performed on $\chi(k)$ (this is known as the *McMaster correction* [6, 7, 8]), leading to a function fully corrected for both intrinsic and extrinsic factors.

3.1.3 EXAFS

EXAFS features are created by a different mechanism than those in other energy regimes. At energies this far above the edge, the core electron is ejected from the absorbing atom, and is thus free to scatter off neighboring atoms. Applying Fermi's Golden Rule, the probability of absorption is proportional to the square of the overlap between the initial and final states of the system, and thus depends on interference between the ground state electronic wave function and the component backscattered from the neighboring atoms. This overlap depends on both the wavelength of the photoelectron and the distance between the absorbing and scattering atom, as well as the potentials of both atoms. Considering these factors, EXAFS is given by:

$$\chi(k) = \sum_j \frac{F_j(k,r)}{k} \int \sin(2kr + \delta_j(k,r)) \frac{P_j(r)}{r^2} dr \qquad (3.2)$$

In this equation, k is the photoelectron momentum, r is the distance between the absorbing and scattering atoms, F and δ are the scattering amplitude and phase shift of the scattering atom, and P is the PDF of the absorber scatter pair. The sum over j allows for more than one scattering atom in the neighborhood of the absorbing atom (and can also be used to account for *multiple scattering*; see Appendix C). The integration over r is necessary because, in any given experiment, a macroscopic number of atoms will be

absorbing, each of which may have a slightly different instantaneous environment. Since a single absorption and scattering event takes place on a time scale much less than that of thermal motion of nuclei, vibration and static disorder both contribute to these differences in the local environment.

The ideal EXAFS equation (3.2) is generally modified in two ways to account for processes other than the single-electron coherent scattering described above. To account for the finite lifetime of the core hole, a mean-free path factor, $e^{-2r/\lambda(k)}$, is added inside the integral, where $\lambda(k)$ is the mean-free path of the photoelectron. A more subtle adjustment is due to multi-electron processes; for example, those in which the incident photon provides its energy to both the core electron and a valence electron. These processes do not contribute to the EXAFS signal, since the variable amount of energy given to the valence electron shifts the EXAFS signal by a continuously variable amount. (The background subtraction process yields an EXAFS signal that has an average value of zero; therefore, random energy shifts will create a signal that is uniformly zero.) In effect, the EXAFS signal is reduced by a factor known as $S_o^2(k)$. Although this factor could be considered part of the intrinsic background, it also involves valence electrons and is thus not necessarily transferable between compounds. For this reason, it is generally included as a parameter in the EXAFS equation. With these two corrections, (3.2) becomes:

$$\chi(k) = \sum_j \frac{F_j(k,r)}{k} S_0^2(k) \int e^{-2r/\lambda(k)} \sin(2kr + \delta_j(k,r)) \frac{P_j(r)}{r^2} dr \qquad (3.3)$$

This equation is the basis of almost all EXAFS analysis.

3.2 Experimental

Although it is possible to collect EXAFS spectra using laboratory x-ray sources, a single scan requires days, if not weeks, and even then only major features (such as the bond length of nearest neighbor atoms) can generally be determined. To determine the shape of the PDF, much higher resolution (and thus, higher intensity) is needed.

Synchrotron radiation is an excellent source of high-intensity, broad spectrum, x-rays. At the National Synchrotron Light Source (NSLS) at Brookhaven National Laboratories, for example, brightnesses of 10^{14} photons/s/mm^2/mrad^2/0.1% bandwidth are routinely achieved, as compared to 10^9 photons/s/mm^2/mrad^2/0.1% bandwidth for a typical discharge tube. Thus, high resolution EXAFS can be collected, typically in under an hour.

A cartoon of a transmission experiment is shown in Figure 3.2. The white x-ray beam from the synchrotron is passed through a computer-controlled monochromator. Conceptually, monochromators work via Bragg diffraction, causing the beam to experience an energy-dependent angular dispersion. A second crystal is then positioned so that x-rays of the desired energy are diffracted back toward the sample. The Bragg condition, however, specifies that each angle will contain not only photons of the desired frequency, but also higher harmonics. If these harmonics were allowed to pass, any XAS measurement would be contaminated by photons of higher energy.

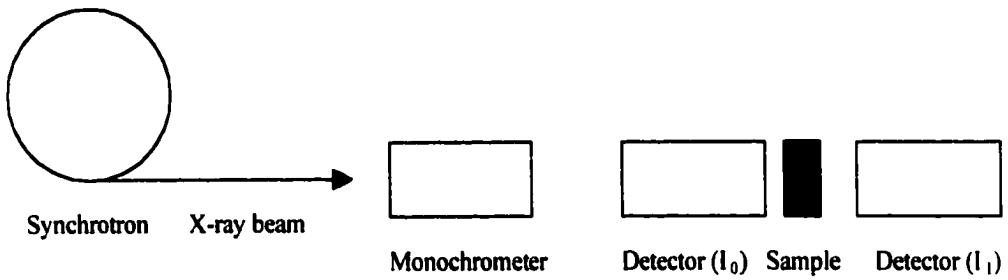

Figure 3.2: XAS experimental schematic

To reduce the impact of these harmonics, three strategies are used:

- Proper choice of the crystal plane can eliminate even harmonics
- The "white" beam produced by a synchrotron decreases in intensity significantly as a function of energy. Thus, higher harmonics are automatically of lower intensity
- The angular spread of the fundamental frequency is greater than that of the higher harmonics. To take advantage of this, the second crystal is aligned with the desired face at a slight angle to the beam produced by the first crystal. In this way, a large fraction (typically 50% or more) of the fundamental frequency is passed while more than 95% of the higher harmonics are rejected.

Exit slits can then be used to improve the energy resolution of the beam. The resolution of EXAFS is inherently limited, since the lifetime of the core hole will introduce some broadening into the spectrum. The exit slits should therefore be narrowed until the EXAFS spectrum shows no further improvement in resolution.

The intensity of the x-ray beam is typically measured by ion chambers. The gas present in these chambers is partially ionized by the x-ray beam. The resulting ions and electrons undergo further collisions, creating a cascade of charged particles that are swept

transverse to the beam by an applied voltage. This creates a current which can then be amplified by conventional means (a typical amplification is 7 to 9 orders of magnitude). It is important that the gas used is inert, so that chemical reactions do not introduce nonlinearities (air, for example, forms some oxides of nitrogen under these conditions; the resulting energy release could alter the kinetics of the cascade and distort the measurements).

A minimum of two ion chambers is required to measure absorption: in a transmission geometry as shown in Figure 3.2, one is placed just before the sample and one just after. The gas used must be chosen so that the pre-sample chamber absorbs enough photons to get good counting statistics, but not so many that the beam is attenuated significantly: 10% absorption is a typical target. The post-sample chamber, on the other hand, can be constructed so that the absorption is somewhat greater, since the beam is no longer required. (Sometimes, a third ion chamber is inserted after the post-sample chamber. This allows insertion of a reference material between the second and third chambers.)

Absorption by the sample follows a Bouguer law [9]:

$$I_t = I_0 e^{-\mu(E)x} \tag{3.4}$$

where I_t and I_0 are the intensities of the post- and pre-sample chambers respectively, x is the thickness of the sample, and $\mu(E)$ is the energy-dependent absorption coefficient of the sample. (Occasionally, this equation is written with $-\mu(E)\rho x$ in the exponential, where ρ is the density of the material.)

The absorption of the sample is thus given by:

$$\mu(E)x = \ln \frac{I_o}{I_t} \tag{3.5}$$

The thickness of the sample, if uniform, is then generally absorbed into the definition of $\mu(E)$, so that the equation then reads:

$$\mu(E) = \ln \frac{I_o}{I_t} \tag{3.6}$$

It is unfortunate that convention dictates that the symbol $\mu(E)$ is used for three distinct quantities: absorption, absorption per unit thickness, and absorption per unit thickness and density. I will attempt to maintain the distinction by context: in all discussions of the analysis of EXAFS data, the definition used in equation 3.6 will be used, while in discussions of sample preparation, where one of the other meanings might be more useful, the definition in use will be explicitly indicated.

It is not necessary for the ion chambers to be calibrated so that they read on the same scale; indeed, it is quite common for the post-sample chamber to be amplified a factor of 10 (or 100) more than the pre-sample chamber, to compensate for intensity lost in the sample itself. This introduces a constant offset in the absorption, which is then removed by the process of background subtraction (see section 3.3.4). It is also generally the case that the response of an ion chamber is a function of energy, both because the absorption of the gas is energy dependent and because the current generated by a single absorption event is proportional to the energy of the photon. As long as the energy response of both the pre- and post-sample chambers is identical, this will not affect the results.

3.3 Analysis: The Curve-Fitting Method

If only low-precision information is required (e.g. first-shell coordination number, the presence or absence of a particular heavy element in the first shell, or a first-shell bond distance to 1% precision), equation 3.3 can be used directly. In these cases, only the contribution from the nearest-neighbors is being considered, and, if a simple form (such as a Gaussian) is assumed for $P(r)$ and $F(k)$ and $S_o^2(k)$ are somehow known (from an analysis of known compounds with similar absorbers and scatterers, for example), a Fourier transform can be used to extract the desired information. In cases for which the PDF's of various absorber-scatterer pairs overlap, however, direct interpretation of the Fourier transform is subjective at best. For the kind of high-precision analysis of complex systems envisioned in Chapter 2, a more reliable method is called for. The "curve-fitting" method, first advanced in the 1970's, has become the method of choice for EXAFS analysis of complex materials.

Rather than try to interpret the Fourier transform of $\chi(k)$ directly, this method requires an *ab initio* calculation of $\chi(k)$ for a model compound of similar structure. This has the advantage of yielding the contribution $\chi_j(k)$ from each scattering path individually, whereas an empirical standard would give only the total $\chi(k)$. FEFF, a software program developed by John Rehr's group at the University of Washington, has proven highly reliable for calculating $F_j(k,r)$ and $\delta_j(k,r)$; details of the algorithms used by this program can be found in the references [10, 13]. $\lambda(k)$ can be determined directly from measured core-hole lifetimes; FEFF contains this information in a look-up table, which is opaque to the user. Other factors in (3.3) can then be varied in a systematic fashion so as to produce the closest match to the data. The parameters determined in this

manner are then thought to be reflective of the structure of the sample itself. This is the essence of the curve-fitting method.

Many objections can (and should) be raised to structures found by this method. For one thing, more than one structure can yield a particular spectrum. As an example, consider an iron atom surrounded by an unknown number of oxygen atoms at a fixed distance. Suppose the theoretical calculation is based on four oxygen atoms, and a value of S_o^2 (assumed, for the moment, to be independent of k) is arrived at by fitting to the data. If the calculation is repeated with an assumption of six oxygen atoms, the fit will be equally good, with a value of S_o^2 that is two-thirds of that found in the previous case. Thus, without some *a priori* knowledge (such as the expected value of S_o^2), it is not possible to use EXAFS to determine coordination number at all! For this reason, EXAFS analysis must always be combined with some *a priori* assumptions about the structure of the material (in the previous example, if the coordination number were known, S_o^2 could be found, or vice-versa, but one of these factors must be known independently). The requirement for some additional information about the system does not invalidate EXAFS as a structural probe, and is indeed a feature of most spectroscopies. Infrared spectra of solids, for example, are nearly meaningless without a fairly detailed knowledge of the system being studied (or, at least, candidates for the system). In fact, it is generally true that the more that is already known about a system, the more new information that EXAFS can provide.

As developed by the University of Washington group, the curve-fitting method incorporates several simplifications:

- $S_o^2(k)$ has been shown to be reasonably constant (typically less than 10% variation) except in regions below $k = 2$ Å^{-1} [11, 12]. For very low values of k, the photon does not have sufficient energy to eject both a core electron and a valence electron, and S_0^2 should approach 1. EXAFS analysis already excludes the low-k region, thus $S_o^2(k)$ is assumed to be constant for these analyses.
- $\lambda(k)$ is assumed to be completely transferable for a specified element and core hole. This is justified by the claim that the core hole is largely unaffected by the chemical environment. For precision work this may be questionable: it is well-known that the energy of the core hole relative to the Fermi level may vary by several electron volts, depending on the oxidation state of the atom. Since this variation in energy is generally less than one part in a thousand, any deviations in $\lambda(k)$ are likely to be small.
- FEFF evaluates $F_j(k,r)$ and $\delta_j(k,r)$ for the model only once, using the assumption that $P_j(r)$ is a delta function at the atomic positions given by the model. If r is varied significantly in the fit, this may introduce errors into the fit. In particular, certain multiple-scattering paths involving collinear atoms have particularly high values of $F_j(k,r)$. Even small deviations from collinearity should suppress these paths substantially. Care must be taken, therefore, when using FEFF multiple-scattering paths for samples that are known to incorporate distortions from the model compound. Likewise, this procedure may introduce measurable errors when analyzing compounds

exhibiting extreme disorder, such that $P_j(r)$ has significant amplitude over more than a tenth of an Angstrom.

- $P_j(r)$ is assumed to be *approximately* Gaussian. The nature of this assumption will be examined more carefully in section 3.3.4.
- Several simplifying assumptions are used in the calculation of $F_j(k,r)$ and $\delta_j(k,r)$; these are detailed in the references [10, 13, 14]. For example, the atomic potentials are somewhat simplified by utilizing spherical atomic potentials with a constant potential in the resulting interstitials between atoms (a "muffin-tin" potential). Also, FEFF uses several criteria to filter out multiple-scattering paths that are likely to contribute very little to the EXAFS signal.

A schematic for the curve-fitting method is shown in Figure 3.3. Further detail is given in the following sections.

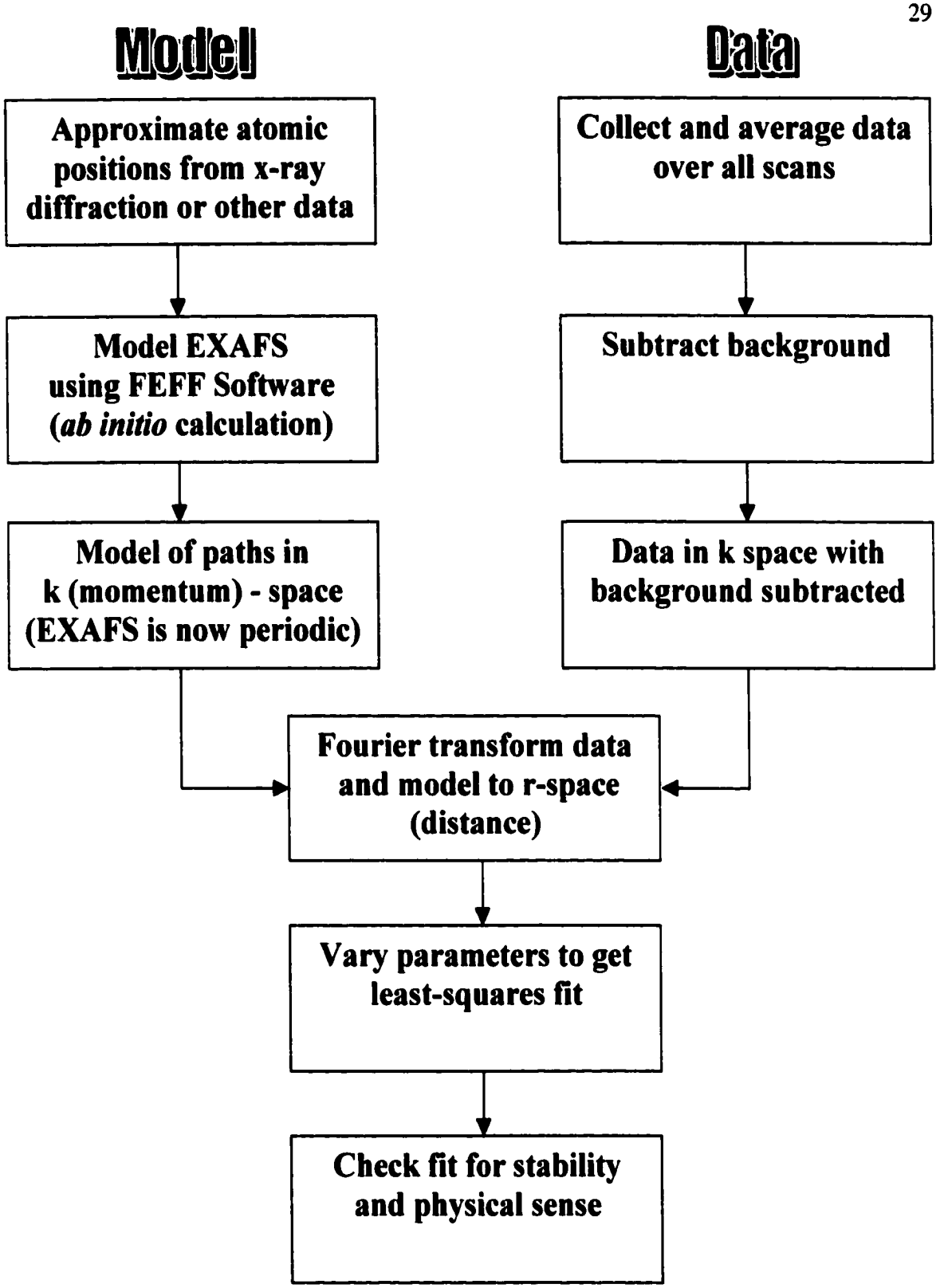

Figure 3.3: Schematic of curve-fitting method of EXAFS analysis

3.3.1 Approximate Atomic Positions for Model Compound

FEFF requires atomic positions in order to compute theoretical path contributions. Because of the limitations described above, it is important that the atomic positions used to calculate these paths be similar to the atomic positions in the material being studied. These positions may be provided by x-ray diffraction studies of a similar material, semi-empirical computations, or any other convenient method.

3.3.2 Model EXAFS Using FEFF/Model of Paths in K-Space

FEFF 8 is used for all materials in this study, with a self-consistent field calculation out to 5.0 Angstroms.

3.3.3 Collect and Average Data Over All Scans

At least two scans were collected for each spectrum evaluated in this study. By comparing multiple scans, the signal to noise ratio can be estimated and certain systematic errors, such as drifts in monochromator calibration, can be detected and corrected for.

The first large peak in the first derivative of the spectrum is then identified as "E_o." The symbol E_o is used for a bewildering variety of different quantities in the EXAFS literature. These include:

- The first large peak in the first derivative spectrum
- The energy of the Fermi level relative to the core hole
- The energy of the conduction band relative to the core hole
- The energy of the Fermi level (or conduction band) relative to the core hole for the pure element

- The differences between two of the above definitions

In practice, the difference between these various definitions is accounted for by allowing the energy origin to float during fitting.

3.3.4 Subtract Background/Convert Data to K-Space

Background subtraction is accomplished by the program AUTOBK [15]. This software performs several related functions:

- A linear function is fitted to the region of the spectrum before the edge (typically 200 eV to 20 eV below E_o). This function is then extrapolated to E_o.
- A quadratic function is fitted to a post-edge region, typically from 100 eV to 300 eV above E_o. This function is then extrapolated to E_o. The difference in this post-edge function and the pre-edge line at E_o is used as $\Delta\mu_o(0)$ in equation 3.1.
- Conversion to k-space is performed using $k = \frac{1}{\hbar}\sqrt{2m(E - E_o)}$ where m is the actual electron mass. Note that E_o as used in this formula is properly the energy of the Fermi level relative to the core hole, which often differs by several electron volts from the peak of the derivative spectrum. FEFF 8 estimates this difference through a self-consistent field calculation, and adjusts $\chi(k)$ accordingly. Nevertheless, a few eV of difference may remain, which should then be corrected for during fitting.
- A modified cubic spline is fit over the EXAFS region to provide $\mu_o(k)$. The number of knots in this spline is determined by a user-adjustable parameter

r_{bkg}, so that the Fourier transform of the EXAFS region will be minimized for values less than r_{bkg}, and largely unaffected for values above. In practice, r_{bkg} is chosen small enough so that no oscillations at EXAFS frequencies are seen in the energy spectrum. Further background refinement may be performed as part of the fitting process.

3.3.5 Fourier Transform Data and Model to R-*Space*

This process is described more fully in Appendix A. In brief, a portion of the *k*-space data is selected, weighted so as to avoid dominance by low-*k* data, windowed so as to reduce truncation effects, and then Fourier transformed to give $\tilde{\chi}(r)$. As long as the same operations are performed on both the data and the FEFF-generated theoretical standards, this process does not produce any systematic errors. This is one of the strengths of the curve-fitting method: the results of a Fourier transform on data depend on the parameters used for the transform, but the results should affect the theoretical standards in the same way. This allows transform parameters to be chosen so as to optimize desirable properties (e.g. resolution of peaks in *r*-space, high-*k* features, etc.) without regard to the distortions introduced into the transform.

3.3.6 Perform Least-Squares Refinement of Model to Data

This step is performed with the aid of the program FEFFIT, written by Matthew Newville [14, 16]. The desired parameters are varied so as to minimize the function

$$\sum_i \left(\tilde{\chi}_{model}(r_i; \text{varied parameters}) - \tilde{\chi}_{data}(r_i)\right)^2 \qquad (3.7)$$

using a Levenberg-Marquardt algorithm. (*i* is an index for the individual points at which the function is evaluated.)

During this stage additional background refinement was generally performed. The background subtraction performed by AUTOBK, although visually acceptable in the energy spectrum, often allows large components to persist in the low *r* range of the Fourier transform. Although this range is not directly fit, spectral leakage is a concern (see Appendix A for a discussion of the cause of this phenomenon). For cases such as these, FEFFIT is capable of refining the background further (the effect has been referred to as "largely cosmetic" by Newville [17]). At an intermediate stage in the fitting process, the backgrounds in this work were generally refined in this way. This has the benefit of providing estimates of the correlation between the background and the fitting parameters (see section 3.6). The newly refined background was then fixed and used for subsequent fits.

Since most of the fits in this work involve multiple spectra simultaneously (e.g. spectra for the same substance at different temperatures), the question arises as to whether a single background should be used, or a separate one for each spectrum. It is my belief that the background remaining after AUTOBK completes its initial refinement is primarily intrinsic. I base this on the observation that the Fourier transform of the remaining function generally has isolated spurious peaks at non-zero *r*, which correspond to fairly rapid variations in $\mu(E)$ (although not, of course, as rapid as the EXAFS signal itself). It is unlikely that structure on this scale would be caused by other elements or even by instrumental effects. The intrinsic background, on the other hand, includes effects such as scattering off of the absorbing atom's own valence electrons (sometimes called atomic x-ray absorption fine structure [18]) which could give structure on this scale. Because this intrinsic background should be reasonably transferable between

similar compounds, I opted for using one standard background for all spectra in each group. In fact, fitting a separate background refinement to each spectrum has a significant disadvantage in studies such as this one: using a single background may introduce a systematic error (e.g. all the amplitudes in the region of spectrum dominated by the second scattering path might be slightly low), while using multiple backgrounds introduces a random error (some spectra have additional amplitude in a region, others have less). Since I intend to compare similar spectra and observe their differences, the consistent systematic error is vastly preferable. In general, the background selected to apply to all the samples was one with particularly low correlations to the parameters being determined.

3.3.7 Check Fit for Stability and Physical Sense

Equation 3.3 is highly nonlinear, and thus it can never be known with certainty that the best set of fit parameters has been found. In addition, as discussed above, it is possible that more than one structure could produce very similar spectra. Because of the simplifying assumptions present in FEFF as well as experimental error, the incorrect structure could actually minimize the function slightly better than the correct structure. For these reasons, it is imperative that some independent method of verifying the quality of the fit be used.

To detect minima that are close together in parameter space, a stability check is performed. The fits are repeated under slightly different conditions (different ranges of k-values or r-values, for example). If there are two nearby minima, these changes should randomly push the fit into one or the other. If, on the other hand, the parameters being fit

maintain constant values (to within calculated uncertainties) during this process, we can be confident that only one minimum lies in that region of parameter space.

Minima that are more distant in parameter space will, by definition, yield parameters that are substantially in error (e.g. an atomic position in a well-defined crystal might be shifted by half an Angstrom). These errors can be recognized and the fit rejected on that basis.

If the stability check covers a large enough region of parameter space so that any minima missed in this process would yield values that are physically unreasonable, then we can be confident that the minimum found is a true representation of the structure of the material (to within calculated uncertainties and the limitations of FEFF and experimental procedure).

3.4 Cumulant Expansion

If the pair distribution function $P_j(r)$ is *approximately* Gaussian, then it is helpful to expand the integral in equation 3.3 using this definition of the *cumulants* C_{nj}:

$$\int e^{i2k(r-r_{oj})} P_j(r)dr = \exp\left(\sum_{n=0}^{\infty} \frac{(2ik)^n}{n!} C_{nj}\right) \tag{3.8}$$

In this definition, r_{oj} is any convenient reference point for the j^{th} path. Common choices include the minimum of the interatomic potential for the absorber-scatterer pair in question, the zero-temperature value of the distance between the pair, the centroid of $P_j(r)$, and the absorber-scatterer distance initially used in the model. In this work, the last definition will be used.

It can be seen that this expression for the cumulants is a natural one by considering the case of purely Gaussian disorder with mean r_{oj} and variance σ^2:

$$\int e^{i2k(r-r_{0j})} \frac{1}{\sqrt{2\pi\sigma_j}} \exp\left(-\frac{\left(r-r_{1j}\right)^2}{2\sigma_j^2}\right) dr = \exp\left[2ik\left(r_{1j}-r_{0j}\right)-2k^2\sigma_j^2\right] \quad (3.9)$$

In this case, the first cumulant $C_{1j} = r_{1j} - r_{0j}$ and the second cumulant $C_{2j} = \sigma_j^2$, with all other cumulants being zero. The first cumulant thus gives the deviation of the centroid of the PDF from the model position, while the second cumulant gives the variance in the absorber-scatterer distance. This interpretation of the meaning of the first two cumulants turns out to hold even when the distribution is not Gaussian [13, 19]. The third cumulant has a similarly straightforward meaning:

$$C_{3j} = \left\langle \left(r_j - \left\langle r_j \right\rangle\right)^3 \right\rangle \quad (3.10)$$

Higher cumulants do *not* follow this simple pattern, but for our purposes, the third cumulant is sufficient. It provides a measure of the skew of the PDF, which, as hypothesized in Chapter 2, is related to the degree of electron delocalization in the bond joining the absorber-scatterer pair.

Using this expansion and the approximations inherent in using FEFF and FEFFIT in the curve-fitting process, the EXAFS equation becomes (out to the third cumulant, based on [20]):

$$\chi(k) = \sum_j \mathrm{Im}\left\{ \frac{F_j(k, r_{oj})}{k\left(r_{oj}+C_{1j}\right)^2} S_o^2 \times \exp\left[-2\frac{r_{oj}}{\lambda(k)} - 2\left[k - \frac{i}{\lambda(k)}\right]^2 C_{2j} + i\left\{ 2k\left(r_{oj}+C_{1j}\right) + \delta_j(k, r_{oj}) - \left[k - \frac{i}{\lambda(k)}\right]\left[\frac{4C_{2j}}{r_{oj}}\right] - \frac{4}{3}\left[k - \frac{i}{\lambda(k)}\right]^3 C_{3j} \right\} \right] \right\} \quad (3.11)$$

The cumulants interact in a rather complicated way, but that is largely the effect of the mean-free path. In the limit for which the mean-free path is long, the following observations may be made:

- In this limit, the third cumulant affects only the *phase* of the oscillation
- The first cumulant affects primarily the phase, with the effect on the amplitude resting solely in the pre-exponential term.
- For typical values found in the EXAFS of materials with low to moderate disorder, the second cumulant affects primarily the amplitude. For example, consider $k = 10$ Å^{-1}, $r_{0j} + C_{1j} = 2.0$ Å, and $\lambda(k)$ large. The coefficient of the second cumulant term in the amplitude expression is then ten times as large as the coefficient of the second cumulant term in the phase expression.
- The effect of the third cumulant on phase can be separated from that of the first and second cumulants by examining the dependence on k. The contribution of the third cumulant term is proportional to k^3, while the other two phase terms are proportional to k.

In summary, the third cumulant should be readily distinguishable from the first two through its strongly k-dependent effect on the phase.

3.5 Sources of Error

Let us now consider sources of error in EXAFS analysis. These are conveniently divided into those that affect the phase and those that affect the amplitude.

Phase effects:

- Difficulty in determining the proper E_0. Although this can be partially corrected for in the fitting process, it is probably the most significant source of error for the phase.
- Errors in monochromator calibration. This is generally easily detectable at the time of data collection.
- Errors in FEFF's calculation of $\delta j(k,r)$.
- Errors in FEFF's calculation of $\lambda(k)$.
- False minima in the least-squares minimization.

Amplitude effects:

- Poor background subtraction.
- Incorrect normalization.
- Detector nonlinearities. This creates an energy dependence in the measurement of μ. Although this seems as if it should affect the phase, the effect will vary slowly with energy and thus primarily distort the normalization of the data.
- Sample inhomogeneities or self-absorption effects. See Appendix C.
- Errors in FEFF's calculation of $Fj(k,r)$.
- Errors in FEFF's calculation of $\lambda(k)$.
- False minima in the least-squares minimization.

Because sample and detector quality and the somewhat subjective process of background subtraction affect amplitude rather than phase, it is not unreasonable to expect that phase information can be determined with greater accuracy than amplitude information. In the case of an error in amplitude determination, the primary impact would be on the second cumulant. This would in turn introduce error into the first cumulant, since the first cumulant and second cumulant both appear weighted by k in the phase expression. Determination of the third cumulant would be least affected by this kind of error, due to its distinctive k^3 weighting in the phase expression. Thus, a primary obstacle to third cumulant determinations is the proper choice of E_0. Appendix D contains a discussion of one technique for minimizing this error.

3.6 Statistics of the Curve-Fitting Method

In order to evaluate the quality of the resulting fit, FEFFIT uses two distinct strategies. The first is based on the conventional statistical definition of χ^2 (the notation is unrelated to the EXAFS $\chi(k)$):

$$\chi^2 = \sum_{i=1}^{N} \left(\frac{f_i}{\epsilon_i} \right)^2 \tag{3.12}$$

where f_i is the function being minimized (the square of the difference between model and data) and ϵ_i is the uncertainty in that measurement. Dividing by the degrees of freedom then gives χ^2_ν, the "reduced chi-square." For fits in which noise is the dominant error, χ^2_ν should approach one.

These definitions present some challenges when applied to EXAFS measurements. They assume, for example, that all measurements are "statistically independent." This is evidently not the case: two measurements 0.25 eV apart are

obviously correlated. This in turn raises the question of how to define degrees of freedom. Doubling the number of points for which f_i is calculated by sampling points more closely together, for example, clearly does not provide twice the information. Indeed, there are basic questions of information content: is a ten-parameter fit on a single k-space oscillation meaningful?

A reasonable approach to these questions is to consider the minimum resolvable difference in peaks of the Fourier transform: if two points could correspond to resolvable peaks, then they can reasonably be asserted to constitute independent measurements. If two peaks are separated by Δr_{peak} in the Fourier transform, beats in the k-spectrum will occur with spacing $\frac{2\pi}{2\Delta r_{peak}}$. (The 2 in the denominator is due to the fact that the EXAFS r is meant to approximate the absorber-scatterer distance, while the scattering path represents the electron wave-function making a round trip from absorber to scatterer and back. For this reason, the basic EXAFS equation is a function of $2kr$, and the Fourier conjugates are k and $2r$.) It is reasonable that the beat pattern is easily visible if half a period is present, so that the two frequencies shift from constructive to destructive interference. Thus, two peaks in the Fourier transform can be resolved if

$$\Delta k \geq \frac{\pi}{2\Delta r_{peak}}. \tag{3.13}$$

This suggests that independent points in r-space should be given a spacing $\Delta r_{indep} = \frac{\pi}{2\Delta k}$. If r-space is then divided into bins of this size, then for a fitting range of Δr, this gives $\frac{2\Delta r \Delta k}{\pi} + 2$ bins at least partially within the range. (The "+2" assumes the

maximum and minimum r-values being fit are not on the boundary between bins. Technically, if the number of independent points calculated in this manner is an exact integer, it should be reduced by one. In practice, this numerical coincidence is unlikely to occur.) Accordingly, a common definition of the number of independent points present in EXAFS data is:

$$N_{idp} = \frac{2\Delta r \Delta k}{\pi} + 2 \tag{3.14}$$

This is the definition used in the present work. (A somewhat different argument for this formula is found in [21].)

In practice, it is not necessary to interpolate the discrete Fourier transform $\chi(r)$ on to a grid with the spacing described above. Instead, χ^2 is found using *all* points in the transform, and then scaled by a factor $\frac{N_{idp}}{N}$, where N is the number of points in the transform.

The other difficulty with evaluating χ^2 for EXAFS data is estimating ε_i, the uncertainty. If the uncertainties were solely due to counting statistics, it could be determined by either of two methods: the inverse square root of the number of counts could be used to give a fractional uncertainty (in accord with Poisson statistics), or multiple scans could be run under identical conditions, so that uncertainties could be estimated from the variations between scans. Unfortunately, for EXAFS of concentrated samples using intense x-ray sources, counting statistics is never the primary source of error. Instead, systematic factors such as those described in section 3.5 dominate. Many of these sources of error are hard to quantify; since known systematic effects can generally be compensated for, those that remain are of course unknown.

If the errors due to systematic factors are evenly distributed in *r*-space ("white"), then the magnitude of the Fourier transform at large *r*, where the EXAFS signal is expected to be negligible, provides an estimate of ε. This is how FEFFIT evaluates ε, using the Fourier transform from 15 Å–25 Å for this purpose. This assumption of "white" systematic errors should be viewed with considerably suspicion. Errors introduced through background subtraction, for example, will be concentrated at low values of *r*. If the feedback mechanism for keeping the monochromator properly detuned is too lax and the detectors are slightly nonlinear, on the other hand, the resulting noise could easily be concentrated only in the high *r* region. Finally, errors in FEFF have no effect at all on the data and are thus not included in this estimate of ε.

Because only a very rough estimate of ε can be made, the χ^2 values obtained in EXAFS curve-fitting should be taken with a rather large grain of salt. χ^2, and particularly χ^2_ν are still useful for *comparing* fits, however. Suppose, for example, that the same data with the same background subtraction is fit using two different sets of constraints. Although ε (and thus χ^2_ν) may easily be off by a factor of 10, this (unknown) scaling factor will be exactly the same for the two fits. Thus if one fit yields a significantly smaller χ^2_ν we can reasonably express a preference for it on that basis. Even if the fits are on different data sets, as long as the data were collected on the same equipment during the same time period and subjected to equivalent background subtractions, then it is reasonable to compare χ^2_ν's.

The reported uncertainty in each fitting parameter is based on the second derivative of χ^2 with respect to the parameter (this is a *total* derivative; it includes the relaxation of the other fitting parameters). These values can be used to approximate the

change in the parameter necessary to change χ^2 by one, a reasonable definition of uncertainty. Unfortunately, the uncertainty is then directly proportional to the poorly-known ε. To compensate for this, FEFFIT uses a trick. Suppose the fit is actually a good one, so that χ^2_ν *should* be one. This would then imply that χ^2 had been overestimated by a factor of χ^2_ν. Since χ^2 is proportional to ε, reducing χ^2 by a factor of χ^2_ν is equivalent to reducing ε by a factor of $\sqrt{\chi^2_\nu}$ and, finally, the uncertainties in the parameter by the same factor. This is how FEFFIT calculates uncertainties; it has the notable advantage of making the uncertainties independent of ε. Because the fit is probably not quite so good that χ^2_ν should be one, this procedure actually *overestimates* the uncertainty in the parameters, and is thus quite conservative. Feffit also calculates correlations between variables, with a correlation of 1 or −1 indicating that the two variables cannot be distinguished in the fit. Correlations with magnitude less than 0.80 are generally considered benign, and values as high as 0.95 can be tolerated in some fits. For further information on statistics calculated by FEFFIT, including correlations between variables, see reference 14.

Since χ^2_ν is primarily useful for comparing fits to data taken under similar conditions, rather than determining whether a fit is valid, then how can the validity of a fit be established? This question is closely related to the problem of false minima discussed in section 3.3.7. As in that case, the quality of a fit can be judged by whether it is physically reasonable.

This criterion runs the risk of being circular: if the only fit that is considered acceptable is one that shows the expected result, then of course the analysis is seriously biased. One solution to this is to fit structural parameters *other than those of interest to the study.* In practice, this must generally be done anyway. For example, this study is

primarily concerned with EXAFS third cumulants. But to accurately determine these cumulants, it is necessary to fit bond lengths as well. Bond lengths are well known for some substances (through x-ray diffraction, for example), and for other substances can be roughly estimated by heuristic chemical procedures. A fit with bond lengths well outside these ranges can be rejected regardless of the statistical measures.

Nevertheless, it would be helpful to have a quantitative measure of the quality of fit that does not depend on the estimation of measurement and analysis uncertainties. A particularly simple measure is the fractional misfit between data and fitted model, known as the EXAFS $\mathcal{R}$–factor:

$$\mathcal{R} = \frac{\sum_i \left(\tilde{\chi}_{model}(r_i; \text{varied parameters}) - \tilde{\chi}_{data}(r_i)\right)^2}{\sum_i \left(\tilde{\chi}_{data}(r_i)\right)^2} \tag{3.15}$$

In summary, differences between the fitted model and the data can be divided into three types: random errors (such as the statistics of counting), systematic errors (such as background subtraction or approximations in FEFF), and fitting errors (inaccurate constraints and failure of FEFFIT to find a true minimum). χ^2_ν attempts to measure the fitting error relative to the other two, but does not generally due this with much accuracy. The $\mathcal{R}$–factor, on the other hand, simply includes all three sources of misfit without making an attempt to separate them. $\mathcal{R}$–factors of less than 0.02 (meaning that 98% of the EXAFS signal is accounted for by the fit) are widely considered to signal acceptable agreement between data and fit.

Finally, it should be noted that the risk of rejecting an unexpected but correct fit in favor of one that is expected is not as great as it might seem. For this to happen, the

expected fit would have to correspond to a false minimum. Since false minima correspond to only a small fraction of parameter space, the probability of one falling at any particular combination of parameters is quite small. Using parameters with known values or temperature dependence to check the results reduces this risk yet further.

3.7 Radial Asymmetry Parameter

Although the third cumulant provides a measure of the asymmetry of the PDF, it is not dimensionless. Therefore, if the entire interatomic potential were larger, the third cumulant would increase even though the shape of the PDF was exactly the same. To address this, Miyanaga and Fujikawa defined a dimensionless parameter proportional to the third cumulant [22]. Their definition, however, was part of a theoretical study and assumed a Morse potential with known parameters. It is thus not useful for experimental work on novel substances. Accordingly, I have defined a dimensionless *radial asymmetry parameter* ρ_j:

$$\rho_j = \frac{C_{3j}}{\bar{r}_j^3} \tag{3.16}$$

where r_j is the mean-internuclear distance ($r_{oj} + C_{1j}$) for the j^{th} path.

Chapter 4

ACCURACY OF CUMULANT DETERMINATIONS BY EXAFS CURVE-FITTING

4.1 Temperature Dependence of EXAFS Cumulants

In 1997 Van Hung and Rehr, using a correlated Einstein model, found analytically simple results for the temperature dependence of the first three cumulants of FCC metals [23]. Because elemental metals such as nickel and copper have been extremely well characterized, and because they exhibit high-quality EXAFS out to large k, this provides an ideal method for verifying the validity of cumulant data determined by the curve-fitting method. This is particularly important for the third cumulant, since it has only rarely been evaluated using this method [24, 25, 26].

It should be noted that Gaussian disorder is assumed in many EXAFS studies. Those that do evaluate the third cumulant have most commonly examined only the first shell, using a technique generally known as the "phase-difference" method [27-32]. This method, although adequate for finding the temperature-dependence of well-isolated first-shell scatterers, is not applicable to scatterers for which the PDF's overlap. In addition, this method determines *only* temperature-dependence, yielding no information about either zero-point values or comparisons between different materials or bonds within the same material.

Using a phenomenological Morse potential of the form

$$V(x) = De^{-\alpha x}\left(e^{-\alpha x} - 2\right), \tag{4.1}$$

Van Hung and Rehr derived results for the second cumulant in terms of the dissociation energy D, a scaling parameter α, and temperature T, with the first and third cumulants written in terms of the second cumulant (x is the interatomic distance relative to the minimum of the potential). This formulation has two important limitations.

First, the model accounts only for thermal disorder, while it is well known that many systems also exhibit static disorder. (In this context, static disorder refers only to deviations from perfect crystallinity; zero-point values for the cumulants due to the uncertainty principle are included in the thermal disorder.) Although it is trivial to add a static offset to Van Hung and Rehr's expression for the second cumulant, this would complicate their expressions for the thermal expansion and third cumulant considerably.

In addition, as suggested in section 3.5, determination of the third cumulant is unaffected by many sources of error which impact the second cumulant. Accordingly, I have recast Van Hung and Rehr's formulae in terms of D, α, and T only, and also explicitly included static disorder terms. (In these formulae, it is assumed that static disorder is independent of temperature. If a phase transition takes place, these values will generally be considerably different above and below the transition temperature.) Here are the results:

$$C_1 = C_{1,static} + \frac{3\hbar}{40}\left(\frac{5}{D\mu}\right)^{1/2}\left(\frac{1+z}{1-z}\right) \tag{4.2}$$

$$C_2 = C_{2,static} + \frac{\hbar}{10\alpha}\left(\frac{5}{D\mu}\right)^{1/2}\left(\frac{1+z}{1-z}\right) \tag{4.3}$$

$$C_3 = C_{3,static} + \frac{\hbar^2}{40\alpha D\mu}\left[3\left(\frac{1+z}{1-z}\right)^2 - 2\right] \tag{4.4}$$

where

$$z = \exp\left[-\frac{\hbar\alpha}{k_B T}\left(\frac{5D}{\mu}\right)^{1/2}\right] \tag{4.5}$$

In these formulae k_B is the Boltzmann constant and μ is the reduced mass of the absorber-scatterer pair.

It should be noted that, if α is not known, it can be estimated from the dissociation energy D and the Einstein frequency ω:

$$\alpha \approx \sqrt{\frac{\mu\omega^2}{5D}} \tag{4.6}$$

It is also worth noting that the temperature dependence of the second cumulant involves *only* the Einstein frequency (and the reduced mass), since the parameters of the Morse potential appear only in the combination $\alpha\sqrt{D}$.

In deriving equations 4.2-4.6, the small shift in resonant frequency with temperature due to anharmonic effects has been neglected. For most materials at temperatures below their melting points, this causes an error of less than 5%, and is generally less than the precision afforded by most EXAFS analyses ("on the order of 10-20%," [13]). If greater accuracy is desired, a first-order Taylor series expansion of the frequency shift yields the following correction to the reduced mass:

$$\mu_{eff} = 5D\left[\left(\frac{5D}{\mu}\right)^{1/2} - \frac{9\hbar^2\alpha}{32\mu}\left(\frac{1+z}{1-z}\right) + \frac{81\hbar^2\alpha^2}{10240\mu}\left(\frac{5}{D\mu}\right)^{1/2}\left(\frac{1+z}{1-z}\right)^2\right]^{-2} \tag{4.7}$$

4.2 Data

Transmission data of a 4 micron nickel foil (99.95% pure from Goodfellow) and a 5 micron copper foil (99.97% pure from Goodfellow) were collected by Azzam Mansour of the Naval Surface Warfare Lab. The data were collected on the K edge at beamline X11A of the National Synchrotron Light Source. Spectra were collected at a series of cryogenic temperatures. Examination of the spectra shows them to be of very high quality: each scan under a particular set of conditions is extremely similar to the others under the same conditions (see Figure 4.1), and the data show clear EXAFS with little noise out to 20 $Å^{-1}$.

a)

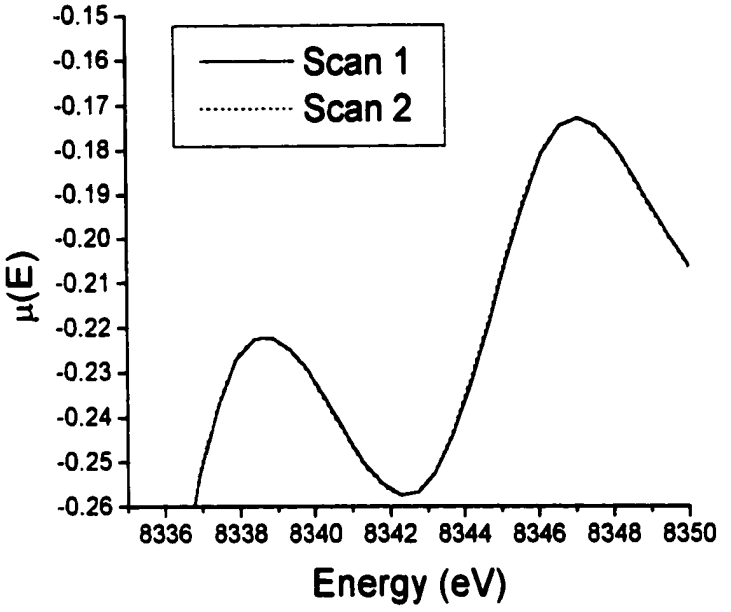

b)

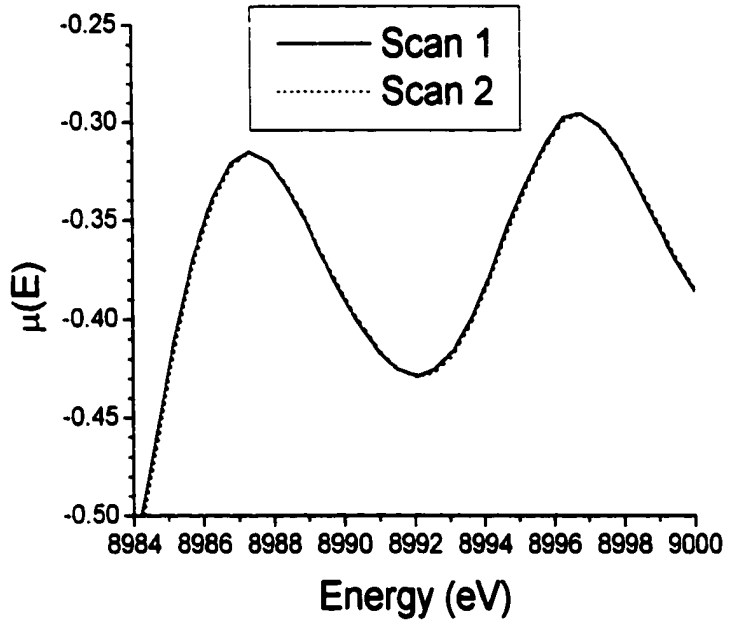

Figure 4.1: XANES of elemental metals: a) nickel at 100 K; b) copper at 200 K.. Successive scans are almost indistinguishable at this scale.

The data were then analyzed by members of our research group[1] under my supervision. Background subtraction was conducted using AUTOBK, with r_{bkg} = 0.9 Å for both metals at all temperatures. Representative results are shown in Figure 4.2. The resulting spectra in *k*-space are shown in Figure 4.3. At this scale, the spectra look very similar.

[1] Marc Bacuyag, David Lipton, and Mihail Rivlin.

a)

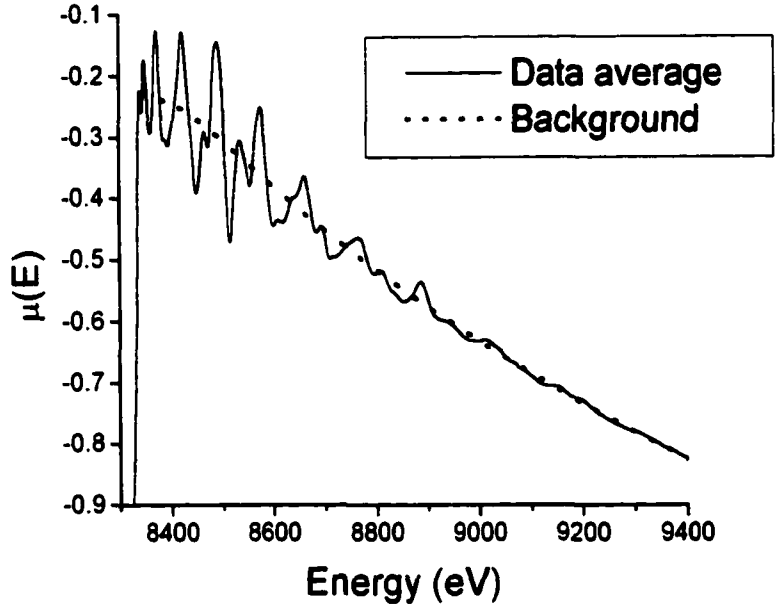

b)

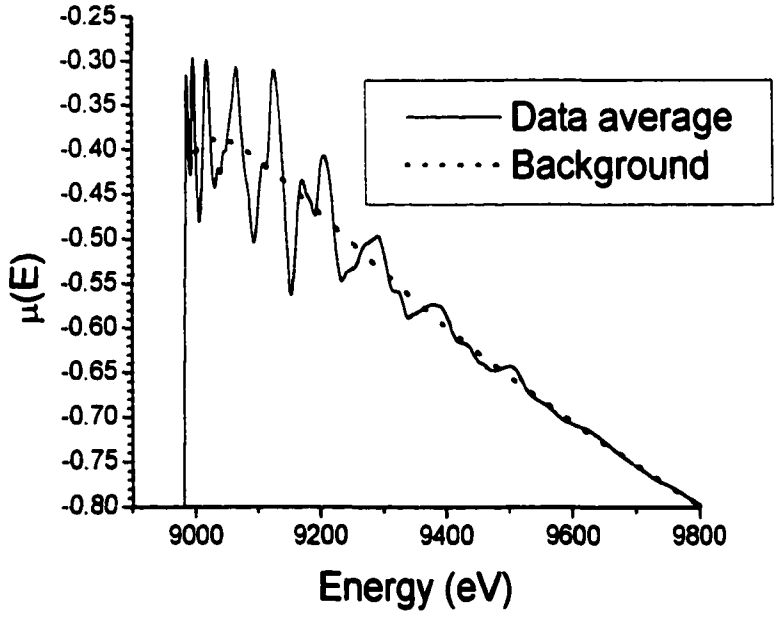

Figure 4.2: Background for elemental metals: a) nickel at 100 K; b) copper at 200 K

a)

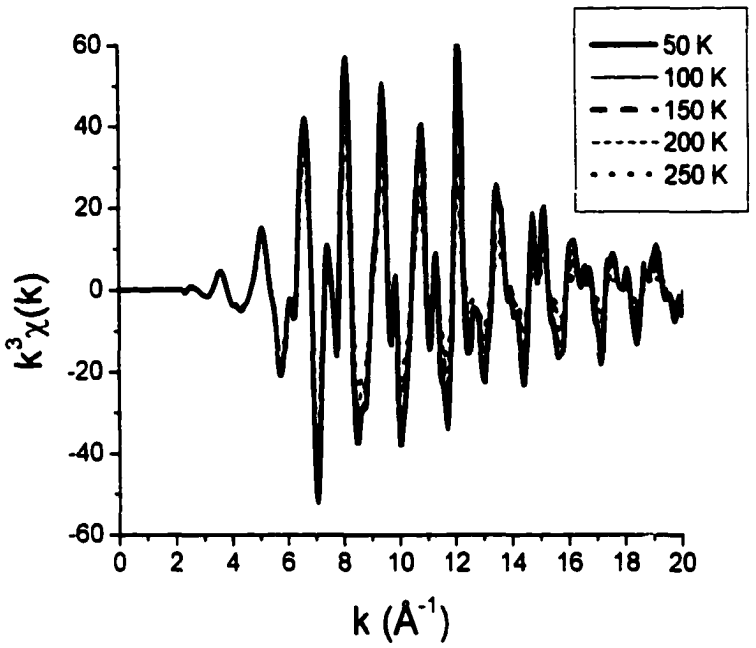

b)

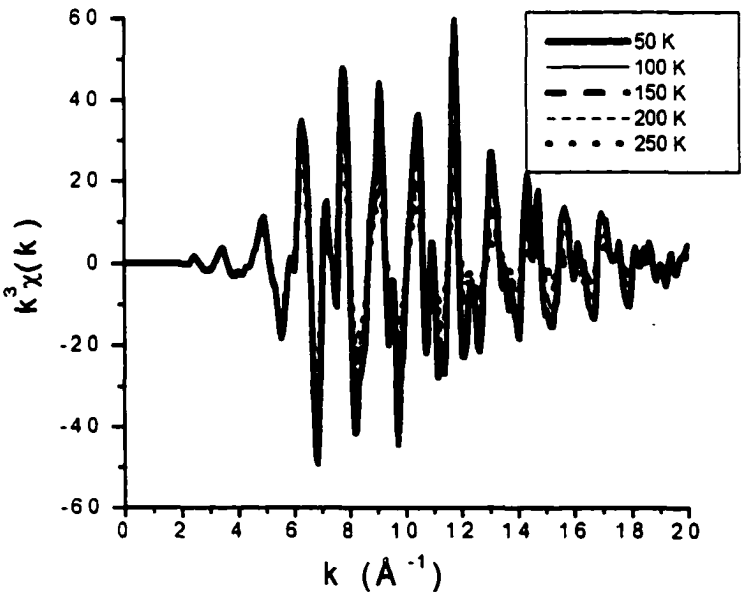

Figure 4.3: *k*-space spectra of elemental metals with *k*-weight 3: a) nickel; b) copper

Figure 4.4a shows detail of the nickel peak around 6.6 $Å^{-1}$. As expected, the amplitude decreases with temperature, implying an increasing second cumulant. The phase appears nearly constant, or perhaps shifts left somewhat with temperature, as would be expected from thermal expansion and equation (3.11). In Figure 4.4b, a peak at much higher k (about 13.5 $Å^{-1}$) is shown. For this peak, there appears to be a small shift right with increasing temperature. Such shifts can be difficult to interpret in general, as they can represent beating between two atoms at similar distances. But in elemental nickel, with its high symmetry, it is more likely to be indicative of a positive third cumulant (see equation 3.11). The copper spectrum shows a similar effect.

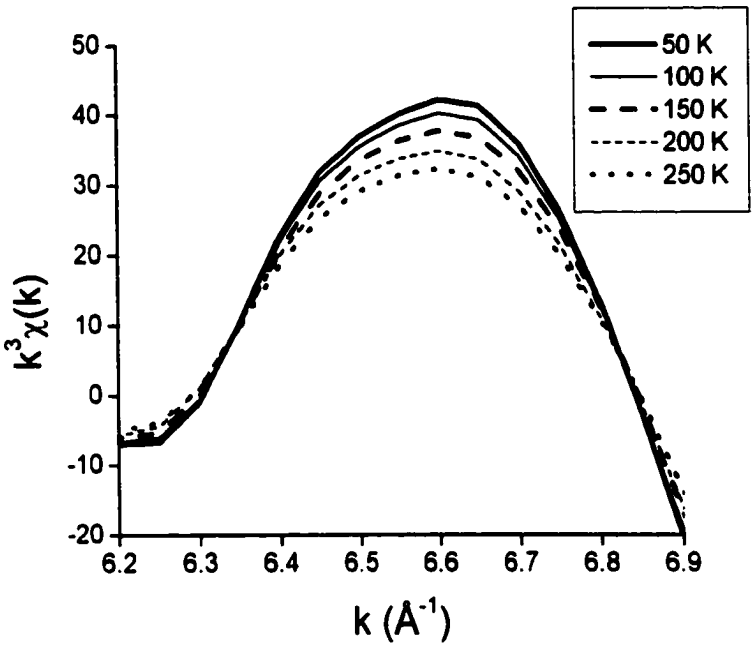

Figure 4.4a: Low-*k* peak of nickel spectra

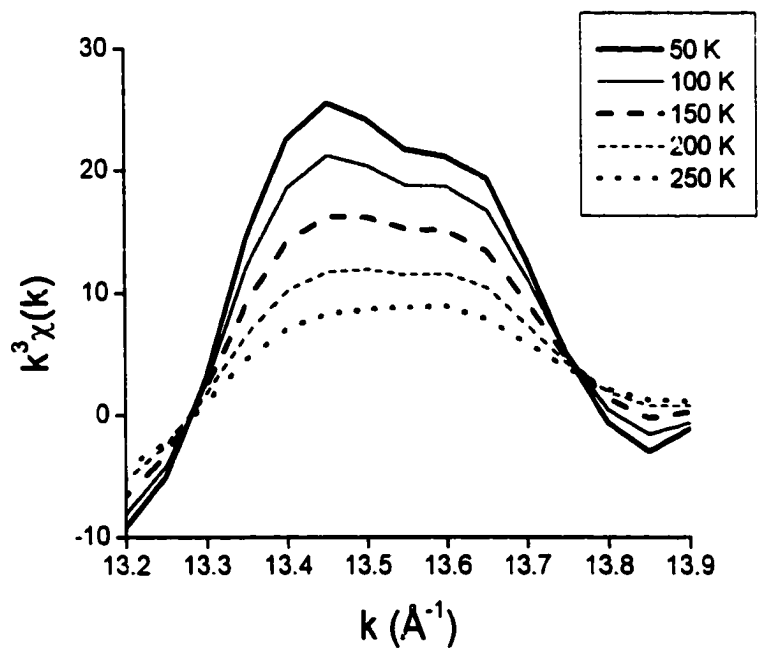

Figure 4.4b: High-*k* peak of nickel spectra

4.3 Analysis and Constraints

Rather than simply fit the first shell, paths well beyond the first shell (*outer paths*) were incorporated. This was done for three reasons:

- Spectral leakage from outer paths contributes to the region of the Fourier transform dominated by the first path (see Appendix A for a description of this problem). Ignoring these paths leads to small systematic errors in the first-shell path. In particular, since these contributions are generally greater on the high-r side of the first path, their omission would artificially increase the value of the first-path third cumulant as determined by a first-path only fit.
- Including outer paths reduces the correlations between variables relevant to the first path (for example, S_o^2 and the second cumulant for the first path).
- Fitting parameters for outer paths provides an additional test for the validity of the fit. (When using this technique, the *outermost* path fit may be partially outside the fitting range, and the parameters found for this path should not be taken too seriously.)

The inclusion of outer paths necessitates a treatment of multiple-scattering paths. For details, see Appendix C.

A preliminary fit was done at one temperature, and then spectra for all temperatures were fitted simultaneously. S_0^2 and ΔE_0 were constrained to the same value for all temperatures, while the cumulant values were allowed to vary freely with temperature. In addition, outer paths were grouped together to reduce the number of free variables being fit.

Finally, the procedure described in Appendix D was used to reduce the correlations between variables.

4.4 Results

The theoretical model for the nickel fit was taken from x-ray diffraction data [33], and is characterized by an FCC unit cell of side 3.524 Å. The scattering paths generated by FEFF are given in Table 4.1.

Table 4.1: Scattering paths for elemental nickel. *Path* is an identification number, *degeneracy* is the number of identical scattering paths with the characteristics shown, r_o is the length of the path in the theoretical model, *type* is explained in Appendix C, and *importance* is the relative amplitude of the path as estimated by FEFF.

Path	Degeneracy	r_o (Å)	Type	Importance
1	**12**	**2.4918**	**Direct**	100
2	6	3.5240	Direct	24
3	48	3.7378	Triangle	13
4	48	4.2538	Triangle	10
5	24	4.3160	Direct	57
6	48	4.6398	Triangle	12
7	96	4.6498	Triangle	28
8	12	4.9837	Direct	20
9	12	4.9837	Flattened	10
10	24	4.9837	Focused	46
11	12	4.9837	Conjoined	9
12	12	4.9837	Double	4
13	48	4.9837	Conjoined	3
14	12	4.9837	Focused	36
15	48	4.9837	Reverse	4
16	48	4.9837	Conjoined	4
17	24	5.5719	Direct	29

The high symmetry of the crystal produces unusually important triangle paths due to their high degeneracy; paths such as 7, which are not geometrically favored, nevertheless contribute as much as some of the direct scattering paths. The multiple-scattering paths were constrained by the "segment" method described in Appendix C.

The model for copper was very similar, since it is also an FCC metal, except that the lattice constant was 3.615 Å [34], and all the paths were scaled up accordingly. In addition, FEFF filtered out paths 13, 15, and 16 as being of little importance to the fit, and the researcher analyzing the data chose not to include path 17. Since the latter path is quite far above the *r*-range eventually selected, it has little effect on the fit, even through spectral leakage.

The following constraints were used for both metals:

- The interatomic distances of the nearest and next-nearest neighbors were allowed to vary separately, with further shells being constrained to vary by a single fraction at each temperature. Physically, it is clear that all interatomic distances must vary from the model by the same percentage, as a consequence of the FCC structure. The purpose of these fits, however, is not to determine the structure of nickel or copper, but to evaluate the accuracy of this method of analysis. In more complex crystals, it is not necessarily the case that all interatomic distances will scale the same way with temperature.
- The second cumulant was constrained in a similar fashion to the bond length. In general, it is not as clear how the second cumulants of different scattering paths should be related. If the motion of all atoms were uncorrelated, then the second cumulant for all paths would be the same. This is assuredly not the

case, since nearest-neighbors will find it easier to move in concert than in opposition. Yet, as the scattering atom becomes increasingly distant from the absorber their interaction drops off rapidly and the interaction can be expected to approach that of uncorrelated atoms (i.e. the second cumulant should approach twice the x-ray diffraction Debye-Waller factor).

- The third cumulant for all pairs beyond nearest neighbors is constrained to be zero. As absorber and scatterer become more distant and their interaction decreases, the third cumulant must approach zero since uncorrelated motion cannot produce an asymmetric PDF.[2]
- S_0^2 was fit by the method described in Appendix D.
- In order to break the correlation between C_{11} and C_{31} the procedure described in Appendix D was performed at one temperature for nickel. Since the results were very similar to those found when both were allowed to vary freely, they were allowed to vary freely at all temperatures. For copper, this procedure was used to fix ΔE_0, while for nickel ΔE_0 was allowed to float freely in the fit.

There are thus 37 parameters being fit: S_0^2; ΔE_0; and three bond lengths, three second cumulants, and one third cumulant at each of five temperatures.

The k-range for fitting was chosen to be 6.5 $Å^{-1}$ to 15.5 $Å^{-1}$ for nickel, and 7.0 $Å^{-1}$ to 16.0 $Å^{-1}$ for the copper. The fits proved very stable to changes in this range; the

[2] This is *not* at odds with the oft-stated fact that thermal expansion depends on anharmonic potentials. Thermal expansion may be thought of as a collective property of the entire crystal in which the lattice itself expands, due almost entirely to the anharmonicity of the interaction between nearest-neighbors. It is trivial to calculate that the thermal motion of an atom has a negligible impact on the local potential of an atom far away.

particular selections were based on statistical measures of quality of fit. After *k*-weighting of 3 and a Gaussian window with $\alpha = 2$ (see Appendix A for the meaning of these parameters), the resulting Fourier transform for the 250 K copper data is shown in Figure 4.5.

The *r*-range for fitting was chosen to be 0.9 Å to 4.0 Å for nickel, and 1.1 Å to 4.2 Å for copper. Because the background was chosen to minimize the signal below 0.9 Å, this is the minimum meaningful value for any fit; the upper limit was chosen primarily to maximize the statistical quality of the fit and to reduce correlations and uncertainties for the parameters being fit. In the case of copper, a slight oscillation of the data around 1.0 Å is probably due to imperfect background subtraction. For this reason, copper was fit only above 1.1 Å. In all cases, the fits were very stable relative to changes in the *r*-range being fitted.

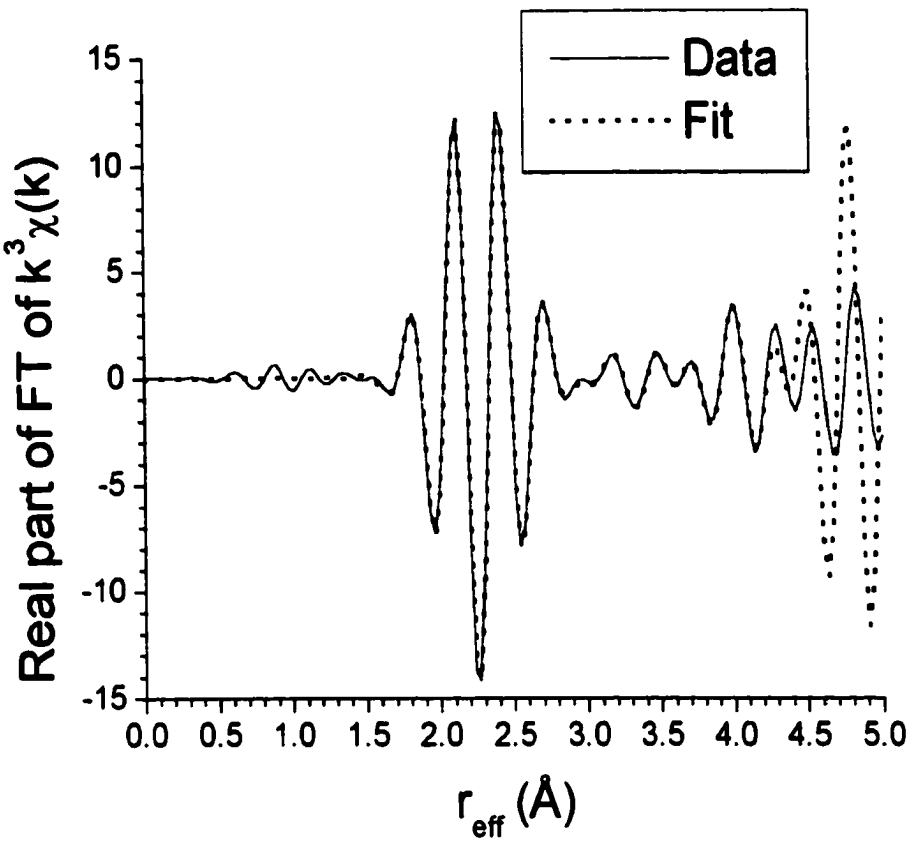

Figure 4.5: Fit for elemental copper at 250 K

Using these ranges, equation 3.14 yields 94.4 independent points for both fits. With 37 parameters being fit, there were 57.4 degrees of freedom. Measures of the statistical quality of the fit at each temperature, along with the overall quality of fit, are shown in Tables 4.2a and 4.2b. Although there is some decrease in the quality of fit as the temperature increases, and the copper is not quite as good as the nickel at high temperatures, all of the reduced χ^2's are under 15, indicative of good fits relative to the

white noise in the spectra. In addition, the $\mathcal{R}$–factors are extremely small, a very small absolute mismatch between data and fitted model.[3]

Table 4.2a: Statistical quality of elemental nickel fits

Temperature (K)	χ^2	Reduced χ^2	$\mathcal{R}$–factor
50	13.4	1.2	0.0001
100	16.6	1.4	0.0001
150	26.0	2.3	0.0001
200	37.9	3.3	0.0001
250	53.2	4.6	0.0002
Overall	**147.2**	**2.6**	**0.0001**

Table 4.2b: Statistical quality of elemental copper fits

Temperature (K)	χ^2	Reduced χ^2	$\mathcal{R}$–factor
50	6.1	0.5	0.0002
100	15.5	1.4	0.0003
150	48.7	4.2	0.0005
200	78.9	6.9	0.0006
250	140.8	12.3	0.0010
Overall	**290.0**	**5.1**	**0.0005**

[3] An $\mathcal{R}$–factor of 0.02 is widely considered indicative of a "good" fit. For nickel, the $\mathcal{R}$–factors are two

The fit for 250 K copper is shown in Figure 4.5. As expected from the measures of statistical quality, the agreement between model and fit is excellent within the range being fitted (the slight decrease in statistical quality observed is primarily due to the oscillation at the lower end of the range).

The results are summarized in Tables 4.3a and 4.3b.

---

orders of magnitude smaller!

Table 4.3a: Results for fits of elemental nickel. Uncertainties are given in parentheses.

Parameter	Temperature (K)	Value
S_0^2	All	0.88(1)
ΔE_0	All	0.4(2) eV
Difference in nearest-neighbor	50	-0.21(5) %
distance relative to model	100	-0.18(5) %
	150	-0.16(5) %
	200	-0.09(5) %
	250	-0.08(5) %
Difference in next-nearest-neighbor	50	0.07(4) %
distance relative to model	100	0.08(4) %
	150	0.09(4) %
	200	0.14(4) %
	250	0.18(4) %
Difference in outer-path	50	0.22(3) %
distance relative to model	100	0.22(3) %
	150	0.21(3) %
	200	0.23(3) %
	250	0.22(3) %
C_{21}	50	0.0030(0) Å^2
	100	0.0034(0) Å^2
	150	0.0040(0) Å^2
	200	0.0047(0) Å^2
	250	0.0054(0) Å^2
C_{22}	50	0.0040(1) Å^2
	100	0.0047(1) Å^2
	150	0.0056(1) Å^2
	200	0.0067(1) Å^2
	250	0.0078(1) Å^2
C_2 for outer paths	50	0.0042(1) Å^2
	100	0.0048(1) Å^2
	150	0.0057(1) Å^2
	200	0.0067(1) Å^2
	250	0.0078(1) Å^2
C_{31}	50	-0.000068(12) Å^3
	100	-0.000062(12) Å^3
	150	-0.000056(11) Å^3
	200	-0.000039(10) Å^3
	250	-0.000028(10) Å^3

Table 4.3b: Results for fits of elemental copper. Uncertainties are given in parentheses.

Parameter	Temperature (K)	Value
S_0^2	All	0.86(3)
ΔE_0	All	0.0(1) eV
Difference in nearest-neighbor	50	-0.51(10) %
distance relative to model	100	-0.44(7) %
	150	-0.41(5) %
	200	-0.28(4) %
	250	-0.19(4) %
Difference in next-nearest-neighbor	50	-0.06(9) %
distance relative to model	100	0.02(8) %
	150	0.07(7) %
	200	0.19(7) %
	250	0.27(7) %
Difference in outer-path	50	-0.02(4) %
distance relative to model	100	0.00(4) %
	150	-0.04(3) %
	200	-0.02(3) %
	250	-0.05(3) %
C_{21}	50	0.0032(1) Å^2
	100	0.0039(0) Å^2
	150	0.0049(0) Å^2
	200	0.0061(0) Å^2
	250	0.0072(0) Å^2
C_{22}	50	0.0042(3) Å^2
	100	0.0056(3) Å^2
	150	0.0072(2) Å^2
	200	0.0089(2) Å^2
	250	0.0103(2) Å^2
C_2 for outer paths	50	0.0032(1) Å^2
	100	0.0054(1) Å^2
	150	0.0068(1) Å^2
	200	0.0072(0) Å^2
	250	0.0098(1) Å^2
C_{31}	50	-0.000081(28) Å^3
	100	-0.000067(21) Å^3
	150	-0.000041(16) Å^3
	200	-0.000004(14) Å^3
	250	0.000046(14) Å^3

For the most part, the behavior of the parameters appears reasonable: the cumulants of the inner two shells increase with temperature and have appropriate orders of magnitude. A few particulars are worth noting:

- Paths beyond the nearest-neighbor show distances that are slightly too large in both metals. A more realistic fit would constrain these paths to show the same fractional change as the nearest-neighbor. As stated in section 4.4, these fits are not meant to provide the most accurate fit possible for nickel and copper, but to test the accuracy of the fitting method. Since most materials may have different temperature-dependence for different scattering paths, the constraints used here are typical. The next-nearest neighbor shows a nearly constant *offset* in fractional distance from the nearest-neighbor, suggesting that the temperature dependence is still accurate, even if the absolute numbers are slightly off.
- The distances for the outer paths are nearly independent of temperature. This is not indicative of a bad fit. Phase parameters for the outer paths should not be considered accurate, since the main features of these paths lie outside the fitting range; they are included to account for spectral leakage.
- The behavior of the second cumulants appears reasonable. Since scatterers at greater distances are likely to have motion less strongly correlated to the motion of the absorbing atom than the nearest-neighbor, the second cumulant should increase with distance, approaching some asymptotic value. This is observed. In the case of copper, the slight decrease in the second cumulant from the second shell to the outer paths is probably due to the decision to

leave out path 17; the small amount of spectral leakage from this path is affecting the amplitude of the outer paths.

- The temperature dependence of the third cumulants appears reasonable. The absolute numbers do not, however; third cumulants in simple materials should be positive. The origin of this apparent negative offset is unknown, but I have observed it in many substances. It is possible that this is a systematic error due to FEFF's approximation of spherically symmetric potentials.

Section 4.5 includes a comparison of these results to the theory given in section 4.1.

4.5 Comparison to Theory

In order to compare the results of the fit with the theory given in section 4.1, it is necessary to obtain values for the parameters of the Morse potential. Girifalco and Weizer [35] used values computed from zero-point energies of sublimation and compressibilities. These authors then used these values to compute elements of the elastic tensor, generally finding agreement with experiment to within 10%, although some components (notably C_{44}) were found to differ from experiment by 50% or more. Since the Morse potential is strictly phenomenological, it should not be surprising that this two-parameter potential has difficulty matching all experimental measurements simultaneously. Milstein [36] and Mohammed *et al.* [37] worked in the other direction, using the elastic tensor components C_{11} and C_{12} (not to be confused with EXAFS cumulants!) to find D and α. Indeed, a set of parameters that are ideal for one experimental regime might have to be modified for a different regime. The parameters

from these papers,[4] as well as the ones I eventually used, are given in Tables 4.4a and 4.4b.

Table 4.4a: Morse potential parameters for elemental nickel

Authors	D (eV)	α (Å^{-1})
Girifalco & Weizer	0.4205	1.4199
Milstein	0.2191	2.4905
Mohammed *et al.*	0.2308	2.0198
Present work	0.32	1.7

Table 4.4b: Morse potential parameters for elemental copper

Authors	D (eV)	α (Å^{-1})
Girifalco & Weizer	0.3429	1.3588
Mohammed *et al.*	0.1503	2.0102
Present work	0.15	2.0

To determine the values of the Morse potential to use, I began by plotting the data from the fits along with the curve generated by equations 4.2-4.4 using Girifalco's and Weizer's parameters (Figures 4.6 and 4.7). The zero-point values of the cumulants were adjusted to provide a good visual fit to the data; these offsets represent some combination

[4] I am somewhat amused that parameters that vary by 50% depending upon how they are determined, and lead to agreement with experiment that is on the order of a few percent, are routinely reported to five

of static disorder[5] and small systematic errors typically seen in the curve-fitting procedure, perhaps due to approximations used in FEFF. Next I adjusted the value of D (see equation 4.1) to provide a good fit to the temperature-dependence of the second cumulant; since only $\alpha\sqrt{D}$ appears in (4.3), there is really only one parameter controlling the shape of the curve (the zero-point value, of course, had to be readjusted). Once D was set, I could adjust D and α in such a way as to keep $\alpha\sqrt{D}$ constant. Doing this, I found the value that best matched the temperature-dependence of the first cumulant. The excellent fit to the third cumulant temperature dependence when using these parameters is then evidence that both the theory in section 4.1 and the curve-fitting method described in Chapter 3 are valid. In addition, it is worth noting that the values of the Morse potential parameters I arrived at in this manner are within the range found by other authors.

---

significant figures.

[5] In the case of the first cumulant, this is not static disorder, but a simple offset related to the model being used for curve-fitting being based on room-temperature data.

a)

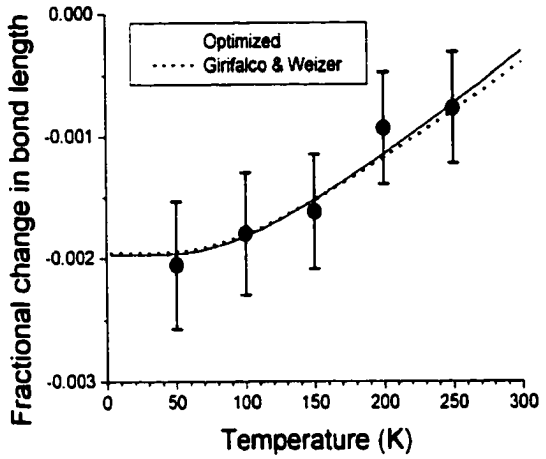

b)

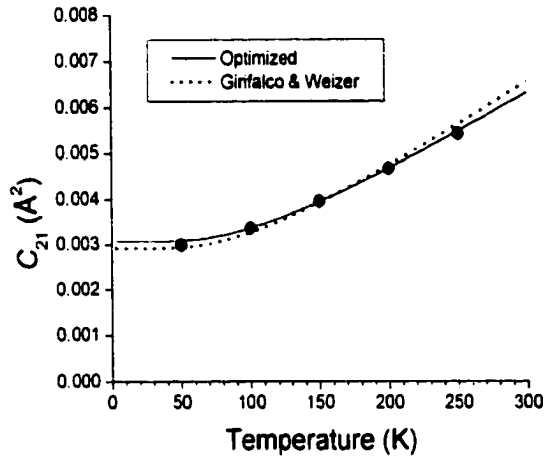

c)

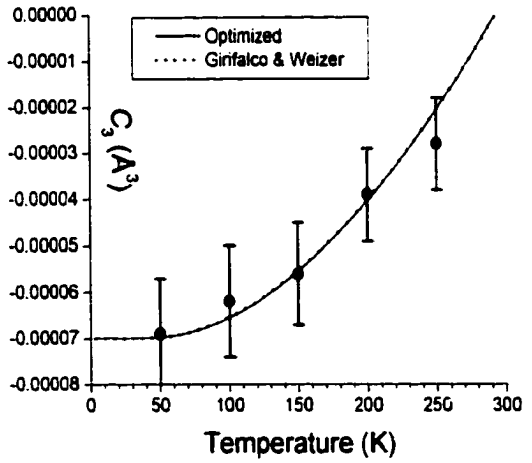

Figure 4.6: Temperature dependence of nearest-neighbor nickel cumulants

a)

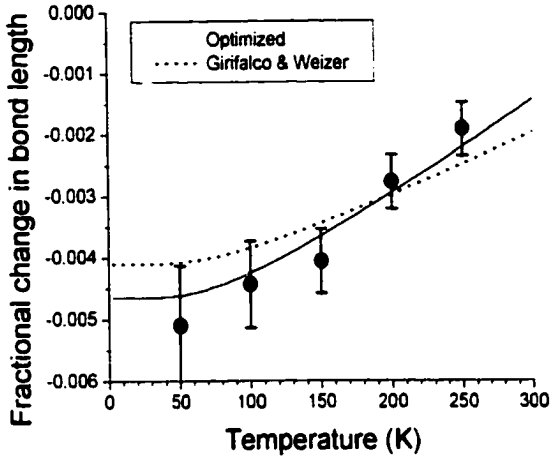

b)

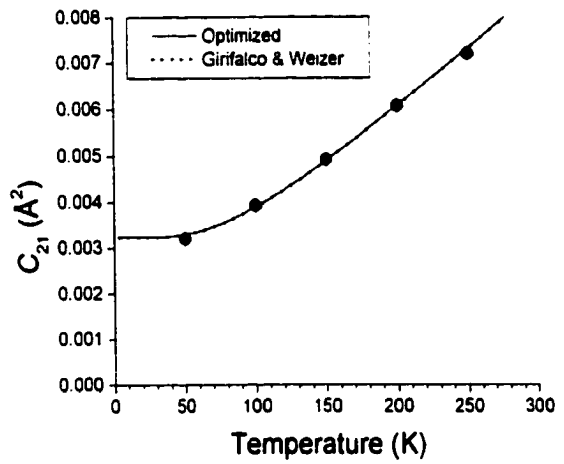

c)

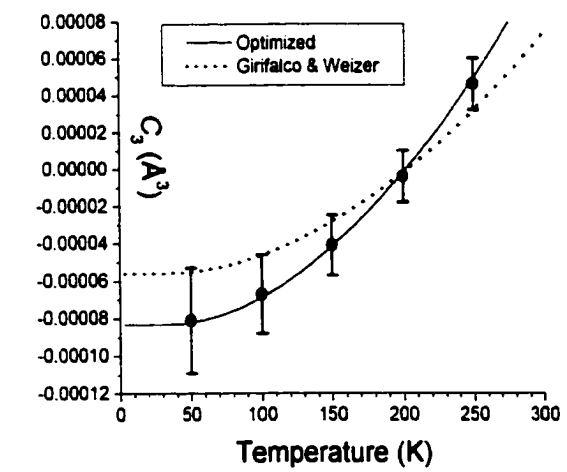

Figure 4.7: Temperature dependence of nearest-neighbor copper cumulants

4.6 Validity of the Cumulants Determined by the Curve-Fitting Method

The results in this chapter clearly demonstrate that the curve-fitting method has sufficient precision and accuracy to determine relatively small changes in the third cumulant, as would be required for testing the hypothesis put forward in Chapter 2. The ability to detect changes in the third cumulant is not the same as the ability to determine the cumulant itself, as can be seen from the results in this chapter: it is doubtful that the third cumulants of elemental nickel and copper should be negative. The origin of this offset is not clear, but it does not interfere with the ability to compare the cumulants of similar materials.

Chapter 5

TITANIUM SESQUIOXIDE: A SEMICONDUCTOR-METAL TRANSITION

5.1 Structure

Titanium sesquioxide (Ti_2O_3) is a semiconductor at room temperature, but exhibits a second order phase transition to a metallic form with onset at 390 K. The structure, with space group R_{3c}, is based on that of corundum (Al_2O_3), and is shown in Figure 5.1.

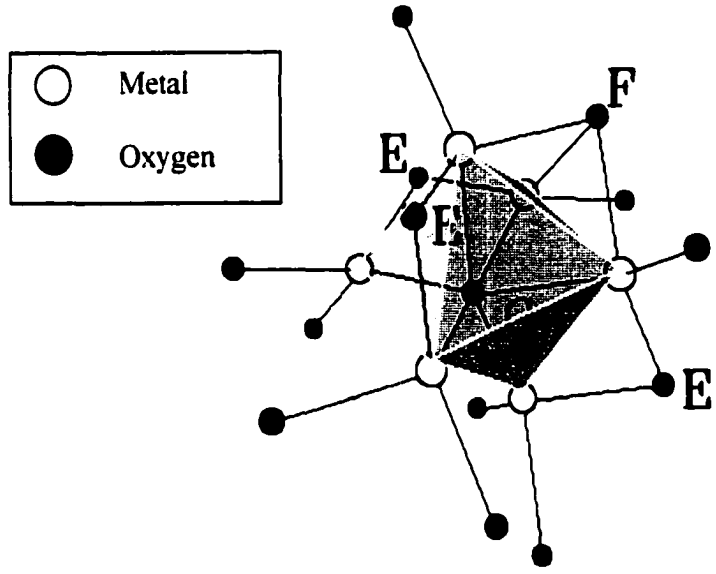

Figure 5.1: Corundum structure

In this structure, each titanium atom is surrounded by six oxygen atoms arranged in a distorted octahedron. The distortion is due to the requirement that the oxygen ions be tetrahedrally coordinated; it is geometrically impossible to satisfy both coordinations without distortion [38]. In Figure 5.1, the atoms in the vicinity of one titanium atom (labeled C) are shown. The structure is moderately complicated; although all titanium

atoms in Ti_2O_3 are crystallographically equivalent, the distortion of the octahedra gives a variety of oxygen-titanium and titanium-titanium distances. Each octahedron shares one face with a neighbor; in the figure, the titanium atom labeled **F** is at the center of the octahedron connected in this matter. Since the crystallographic *c*-axis runs through this bond, this is referred to as the axial bond. Each octahedron also shares three edges with neighboring octahedra; the central atoms in these octahedra are indicated by an **E**; these are referred to as basal bonds. Nine neighboring octahedra share only a vertex; the central atoms for these structures are unlabeled in the figure.

Using molecular orbital theory, the axial Ti-Ti bond has been implicated in the semiconductor-metal transition [39]. Since the electrons in the axial bond are predicted to delocalize at the transition, it should show a sharp increase in its radial asymmetry parameter at the onset of the transition. Because the second-order transition implies a modification of the local structure in advance of the long-range structure, I would expect the radial asymmetry parameter to complete its transition over a somewhat smaller temperature range than the conductivity or x-ray diffraction determinations of bond length.[6]

5.2 Experimental

To verify the predictions of the previous section, we performed temperature-dependent x-ray absorption measurements on the titanium K edge for 99.8% pure titanium sesquioxide

---

[6] X-ray diffraction does not actually determine bond length, but rather the difference in average positions between two atoms relative to the crystal lattice. For a disordered material, this is not the same thing as bond length, as can be seen in the following artificial example: consider a diatomic molecule positioned *completely at random* within the unit cell (this is, of course, not really possible, but something like intercalated carbon monoxide gas could come close). In that case *both* atoms would have average positions

powder (source: Alfa Aesar) using beamline X23B of the NSLS. This beamline uses a Cowan type Si(111) double-crystal monochromator and two focusing mirrors [40]. Harmonic rejection is a natural consequence of the optics, and thus detuning is not necessary.

A heater and thermocouple were used to reach the desired temperatures. The sequence of temperature collection and the range of temperatures recorded are shown in Table 5.1. During the course of analysis, it was found that measurements that showed variations of temperature greater than within $\pm$ 2 K during data collection did not provide results consistent with the others; in these cases I would speculate that the varying temperature caused a variation in bond length which interfered with attempts to determine the third cumulants. Although the analysis reported used only measurements with temperature stability of $\pm$ 2 K, it is not unlikely that, because of thermal gradients in the sample chamber, the thermocouple was reading temperatures slightly offset from the temperature of the sample itself. To account for this possibility, I have assigned an uncertainty of $\pm$ 5 K to the temperature measurements.

---

at the center of the unit cell, and the x-ray diffraction "bond length" would be zero. EXAFS, on the other hand, would still provide the correct average bond distance.

Table 5.1: Ti_2O_3 temperatures

Measurement	Temperature Range (K)
1	296-297
2	349-357
3	424-429
4	494-498
5	445-448
6	390-393
7	366-368

A typical energy spectrum is shown in Figure 5.2. For the most part, the scans appear consistent, but there is some evidence that the monochromator is off by about 1 eV from 4985-4995 eV of one of the scans. This kind of problem, if sufficiently severe, can impact the ability to determine phase variables such as the third cumulant. In the data that was used for this chapter, the problem appeared relatively minor, although sometimes one scan had to be translated by a few eV to align it with other scans at the same temperature.

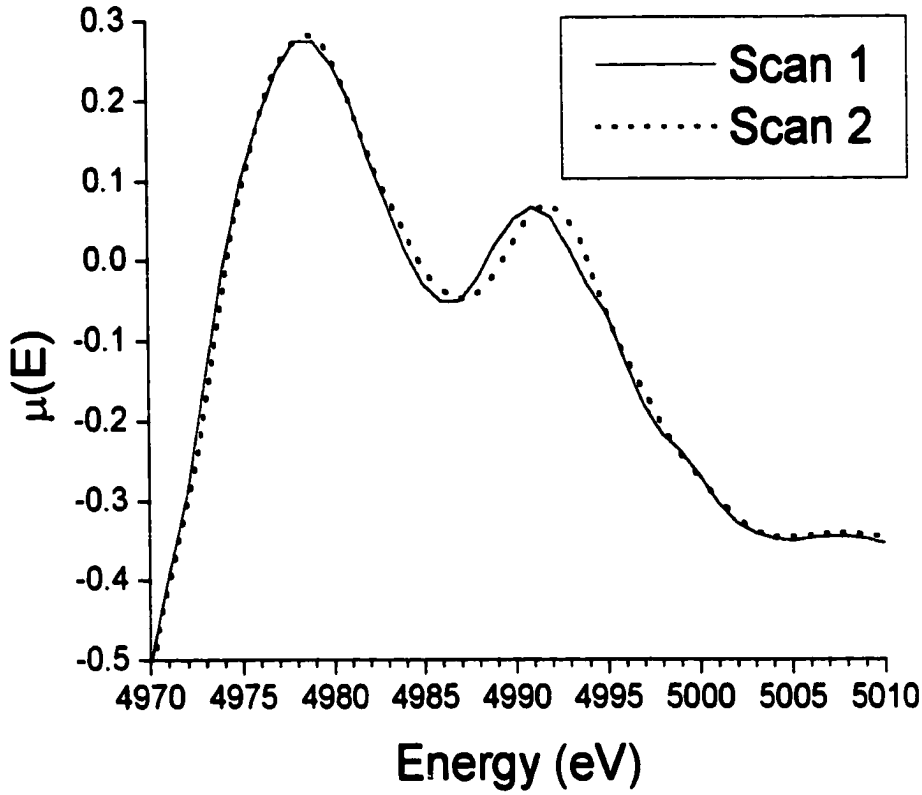

Figure 5.2: Ti_2O_3 XANES at 392 K

5.3 Analysis[7]

Preliminary background subtraction was performed using AUTOBK with r_{bkg} = 1.2 Å; a representative example is shown in Figure 7.3. During the fit, the background was refined further using FEFFIT. The only significant correlations were between the background for the room-temperature fit and S_o^2, which were as extreme as –0.84. Not surprisingly, no significant correlations with phase variables were present. I then fixed the background determined at this stage for the 368 K measurement as the background for all subsequent

fits. The 368 K background was chosen because it showed particularly low correlations with the parameters being fit.

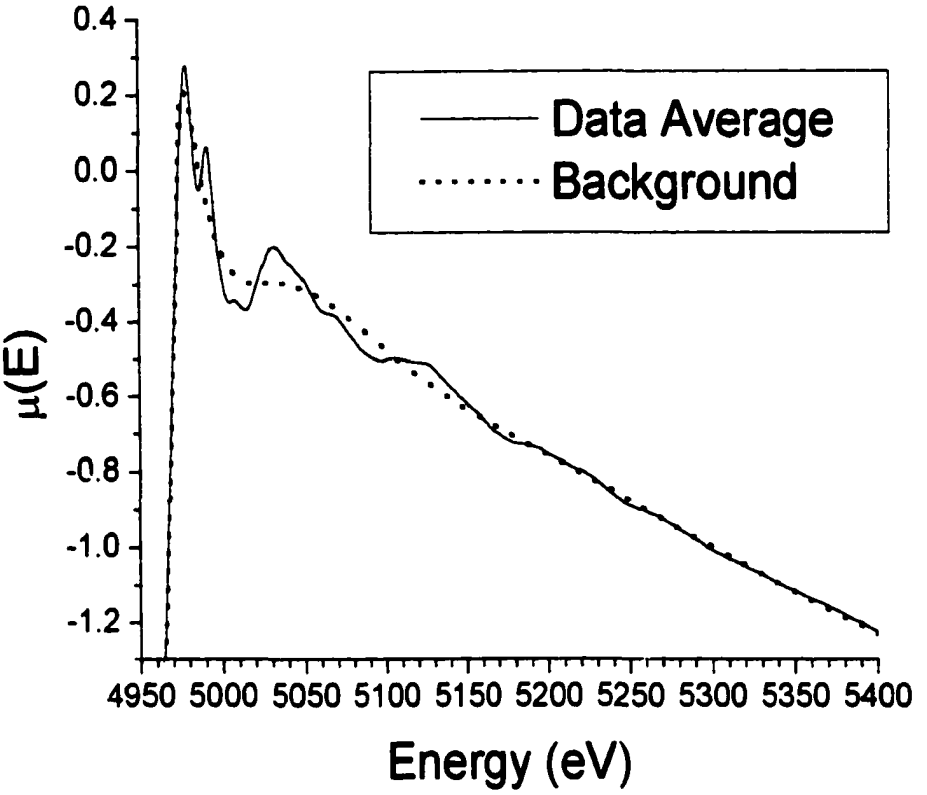

Figure 5.3: Ti_2O_3 background at 392 K

As a basis for the theoretical standard, we used the x-ray diffraction determination of 621 K titanium sesquioxide of Rice and Robinson [41]. The parameters of this model are given in Table 5.2. The room-temperature x-ray diffraction determination by the same researchers [42] gave a very similar structure, with *c* being smaller (13.611 Å) and *a* being slightly larger (5.158 Å).

[7] Preliminary analysis on this material was performed by Vitaly Kishinyovsky under my direction. I then refined the preliminary fit.

Table 5.2: Model for Ti_2O_3

Unit cell dimensions	a = b = 5.126 Å; c = 13.878 Å
Titanium (fractional coordinates)	0, 0, 0.3467
Oxygen (fractional coordinates)	0.3107, 0, 1/4

The scattering paths identified by FEFF as possibly significant are given in Table 5.3.

Table 5.3: Scattering paths for Ti_2O_3. *Path* is an identification number, *degeneracy* is the number of identical scattering paths with the characteristics shown, r_o is the length of the path in the theoretical model, *type* is explained in Appendix C, and *importance* is the relative amplitude of the path as estimated by FEFF. The axial and basal titanium-titanium direct scattering paths are given in bold.

Path	Scattering element(s)	Degeneracy	r_0 (Å)	Type	Importance
1	O	3	2.0184	Direct	100
2	O	3	2.0826	Direct	93
3	**Ti**	**1**	**2.6840**	**Axial**	19
4	**Ti**	**3**	**2.9826**	**Basal**	46
5	Ti, O	6	3.4246	Triangle	11
6	O, O	6	3.4582	Triangle	11
7	O, O	6	3.4619	Triangle	12
8	O	3	3.4983	Direct	27
9	O, O	6	3.5066	Triangle	10
10	Ti	3	3.5398	Direct	32
11	Ti, O	6	3.5418	Triangle	15
12	Ti, O	4	3.5418	Triangle	10
13	Ti, O	2	3.5148	Triangle	5
14	O, O	4	3.5508	Triangle	6
15	O	3	3.7304	Direct	23
16	Ti	6	3.7561	Direct	56
17	O	3	3.7797	Direct	22
18	Ti, O	6	3.7883	Triangle	23

19	Ti, O	6	3.9286	Triangle	25
20	Ti, O	6	3.9286	Triangle	25
21	O	3	4.0386	Double	14
22	O, Ti	3	4.0368	Reverse	7
23	O	3	4.0608	Direct	18
24	O, O	6	4.0905	Flattened	34
25	O, O	6	4.1010	Conjoined	54
26	O, Ti	2	4.1010	Reverse	5
27	O, Ti	3	4.1010	Reverse	11
28	O, Ti	3	4.1010	Reverse	8
29	O, Ti	3	4.1010	Reverse	11
32[8]	O, O	6	4.1376	Triangle	9
33	O	3	4.1653	Double	12
34	O, O	6	4.1653	Conjoined	4
35	O, O	6	4.2466	Triangle	8
36	Ti	1	4.2550	Direct	7
37	O, Ti	6	4.2818	Triangle	10
38	O, O	6	4.2908	Triangle	8

[8] 30 and 31 are skipped as labels because of a quirk in the operation of FEFF's filters; this should be considered a labeling scheme only and not evidence of particular "missing" paths. (Many multiple-scattering paths are eliminated from consideration by FEFF because their amplitude is too low; most are never even assigned numbers.)

As can be seen from the table, the axial and basal paths are well separated from all other paths, although they are fairly close to each other. According to (3.13), the range of *k*-space needed to resolve the peaks is

$$\frac{\pi}{2\Delta r} = \frac{\pi}{2(2.9826\text{Å} - 2.6840\text{Å})} = 5.26\text{Å}^{-1}, \tag{5.1}$$

smaller than the typical EXAFS fitting range. Accordingly, it should be possible to fit these paths separately.

After considerable trial and error in attempting to achieve a good fit (by both statistical and physical criteria), we arrived at the following constraints:

- All direct scattering paths except the axial and basal paths were constrained to have a similar temperature expansion. This included the two nearest-neighbor oxygen paths (paths 1 and 2), which are too close together to resolve by EXAFS, and all the "outer" paths, which affect the fit only through a small amount of spectral leakage. Each of these "uninteresting" paths was constrained to have the same (undetermined) coefficient of thermal expansion and the same offset between the 392 K length (chosen because it was toward the middle of the sampled temperature range) and the model. The oxygen octahedron was actually constrained to have the same *percentage* offset, so that the octahedron kept the same shape.
- The lengths of the axial and radial bonds were constrained to the temperature-dependent lengths found by a previous x-ray diffraction study [43].
- The second cumulant of *all* paths, including the axial and basal paths, was constrained to be the same at each temperature, *except* that the distorted oxygen octahedron was constrained to have second cumulants in the ratio of

their Ti-O bond length squared. The physical justification for this constraint is that the potential in which the oxygens move is dominated by the titanium to which they are bound; therefore if they are a greater distance from the titanium, it is not unreasonable that the cumulants might scale as well. On the other hand, atoms further out, including the axial and basal titaniums, move *primarily* in the potential of atoms other than the absorbing titanium (e.g. the axial titanium is *primarily* constrained by its oxygen octahedron), and thus should have second cumulants independent of distance from the absorbing atom, eventually approaching twice the x-ray diffraction Debye-Waller factor. On a physical basis, of course, other reasonable hypotheses could also be made. Statistically, the fit was best when this set of constraints on the second cumulant was applied, so they were selected as being physically reasonable and statistically desirable.

- The second cumulants of all paths were constrained to follow an Einstein model for temperature dependence, with the single Einstein temperature found in the fit.
- The third cumulant of the nearest-neighbor oxygens (paths 1 and 2) was fit to a model in which the value increased with the square of the temperature (an approximation to equation 4.4). The proportionality constant and the zero-point value were unconstrained. The second nearest-neighbor was scaled to the cube of the ratio of its bond-length to that of the nearest-neighbor, using an argument similar to that for the second cumulant. The third cumulant of the basal bond was fit to a similar model, but the proportionality constant and

zero-point value were allowed to vary separately from the oxygens. The third cumulant of all outer bonds was set to zero; if the motion of those atoms is assumed to be uncorrelated to the absorbing atom, then their PDF's cannot be asymmetric. The third cumulant of the axial bond was completely unconstrained at each temperature, since it is the variable of interest.

- S_o^2 was constrained to be temperature-independent.
- ΔE_0 was found by the method described in Appendix D.

The parameterization of the outer paths is probably too simplistic for a substance undergoing a phase change. The *r*-range selected for fitting stops at a relatively low *r* (see below), however, meaning that these paths contribute only through a small amount of spectral leakage.

Thus there are a total of fourteen parameters fit: S_0^2, ΔE_0, the Einstein temperature, the 393 K offset and thermal expansion coefficient for the "uninteresting" paths, the zero-point and proportionality constant for the third cumulant for the oxygen octahedron, the zero-point and proportionality constant for the third cumulant for the basal bond, and the third cumulant of the axial bond at each of the five temperatures.

The *k*-data (k-weight 3; see Appendix A) is shown in Figure 5.4. The range chosen for the final fit was 3.5 $Å^{-1}$ to 12.5 $Å^{-1}$, avoiding XANES effects and background errors that distort the low-k region and continuing as far as there are reliable oscillations. Figure 5.5a shows the detail of the major peak near $k = 6.5$ $Å^{-1}$. The amplitude decreases monotonically with increasing temperature, as would be expected from the increase in thermal disorder. The phase behaves reasonably as well, shifting slightly to the *left*

between the 367 K and 392 K temperatures, as would be expected from expansion of the bond (see equation 3.11). The peak near 10.3 $Å^{-1}$ (Figure 5.5b), however, shows decidedly different behavior. In particular, the 456 K and 496 K spectra form a group peaking about 0.15 $Å^{-1}$ *higher* than the room temperature and 367 K data, with the 392 K appearing to form a broad transition between the two groups. Although this is the opposite of would be expected from bond expansion, at high values of *k*, the third cumulant plays a more important role. A positive third cumulant shifts the data to the right. With the axial and basal bond lengths as similar as they are, it is difficult to draw any conclusions from visual examination of the spectra in *k*-space, but examination of these peaks does support the conclusions drawn from curve-fitting (section 5.4).

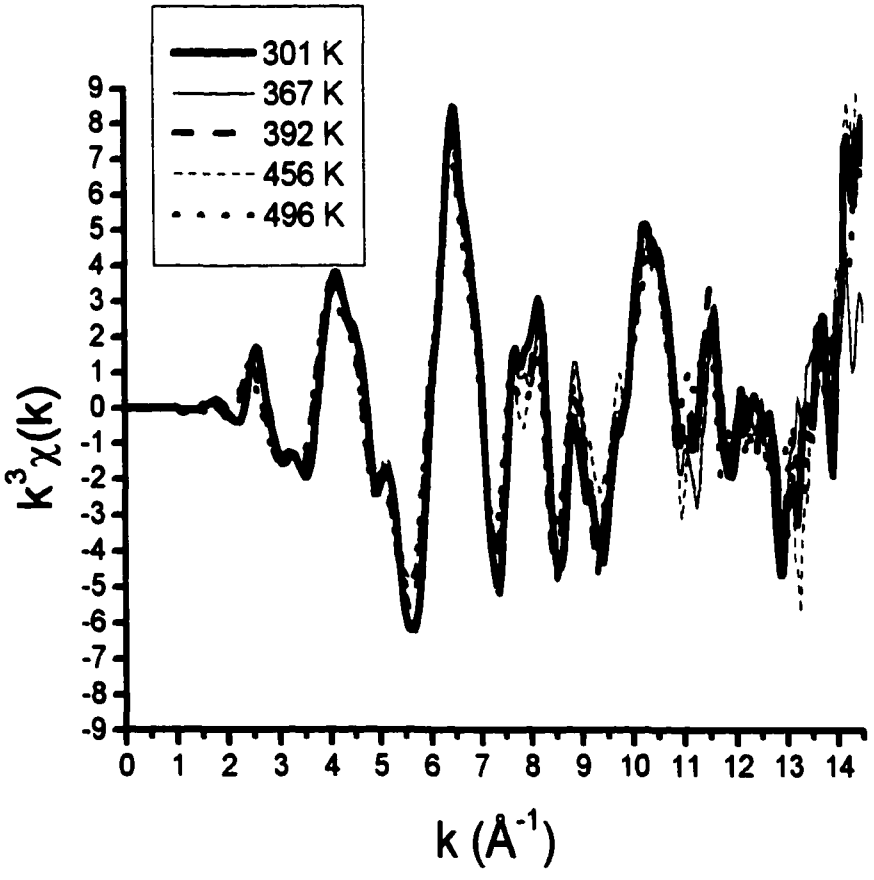

Figure 5.4: *k*-space spectra of Ti_2O_3 with *k*-weight 3

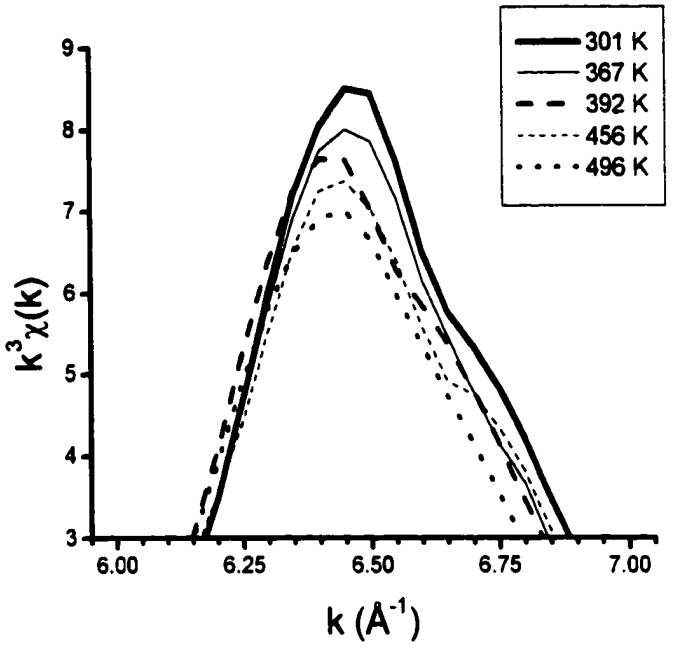

Figure 5.5a: Low-*k* peak of Ti_2O_3 spectra

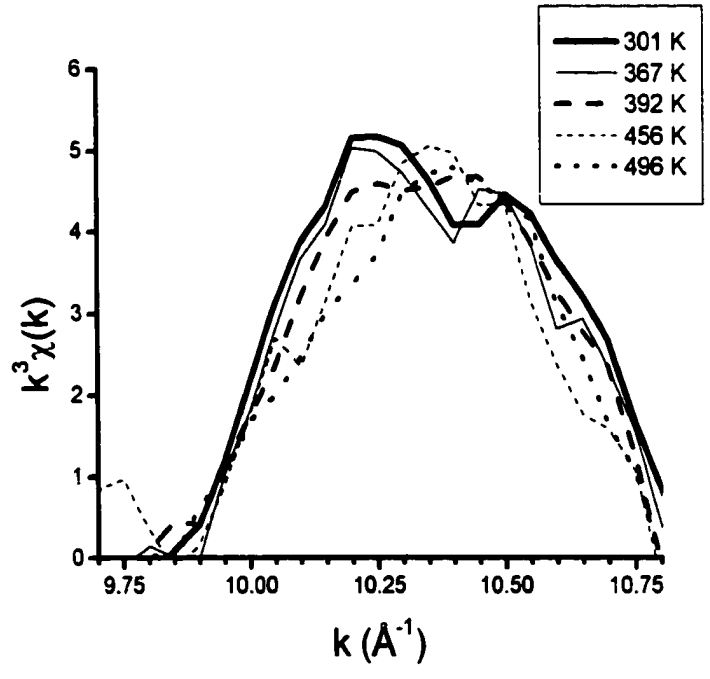

Figure 5.5b: High-*k* peak of Ti_2O_3 spectra

The fit is stable with respect to small changes in the lower limit of *k* and changes in the *k*-weight, but does show instability at the high-*k* end. Small changes in the maximum end of the range cause the fit to shift unpredictably between two different fitting minima. But each of the two minima appears fairly stable, and one has nonphysical behavior: a shorter bond distance for the "uninteresting" paths at 392 K than is found in the room-temperature X-ray diffraction data, no clear temperature dependence in the axial third cumulant, and a decrease in the basal third cumulant with increasing temperature. Since there are two distinct minima sharply distinguished by their parameters, with one giving unphysical parameters, I have accepted the physically reasonable fit despite this instability.

The *r*-range for the final fit was 1.7 Å to 2.0 Å,[9] using a Hanning window with sills of width 1.0 $Å^{-1}$ (see Appendix A). This relatively small range captures a good portion of the signal from the axial and basal bonds, while allowing only spectra leakage from the complex outer paths. It might seem that it should miss the axial and basal bonds as well, since they are found at 2.68 Å and 2.98 Å respectively, but it must be remembered that the *r* in the Fourier transform is only roughly equivalent to the *r* in the PDF. The phase shift to the potentials of the absorbing and scattering atom, in particular, tends to yield a peak in the transform at a shorter *r* than in the corresponding PDF. This is one of the reasons that theoretical standards are useful; if the transform were an accurate reflection of the PDF, there would be less need for curve-fitting! Figure 5.6 shows the real part of the Fourier transform of the data, and the contribution to the 496 K model from just the axial path. As can be seen, the axial path contributes significantly within the

range being fit. The stability of the fit to changes in r-range is poor, being plagued by the same false minimum seen with changes in the upper limit of the k-range. Nevertheless, the two minima are again clearly distinguishable, and one is clearly unphysical.

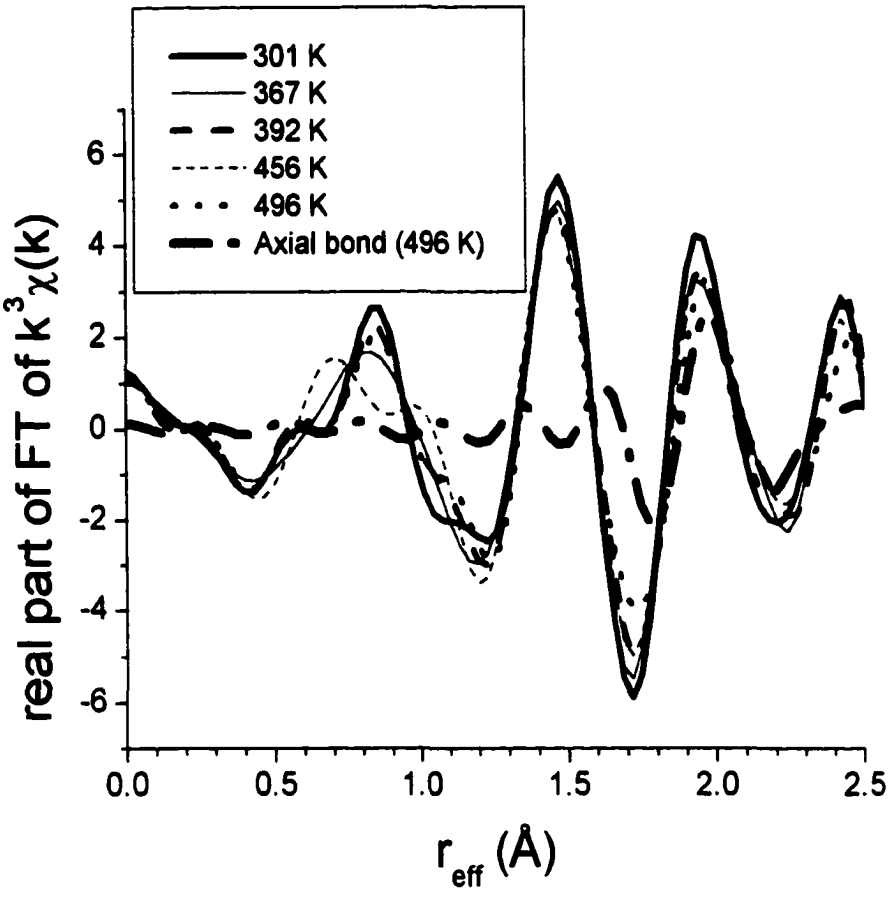

Figure 5.6: Real part of the Fourier transform of Ti_2O_3 data, with model of contribution from axial bond shown.

Our final fit had 17.0 independent points as calculated by equation 3.14. With 14 variables being fit, this gives only 3 degrees of freedom. Nevertheless, as can be seen in Table 5.4, the overall reduced χ^2 is 50 and under 90 for each fit, which is acceptable for a material of this complexity. In addition, the $\mathcal{R}$-factor is 0.0035, indicating very little

[9] Initially, fits with greater r_{max} were attempted, but this tended to complicate the issue without improving

mismatch between model and fit. A graph of the Fourier transform of the 392 K data (the set with the lowest statistical quality) and the fitted model is shown in Figure 5.7.

Table 5.4: Quality of Ti_2O_3 fit

Temperature (K)	χ^2	Reduced χ^2	$\mathcal{R}$–factor
296	7.6	12.7	0.0003
367	30.4	50.7	0.0025
392	49.8	83.0	0.0052
446	40.8	68.0	0.0069
496	22.1	36.8	0.0024
Overall	**150.7**	**50.2**	**0.0035**

the statistical quality of fit, correlations, or uncertainties significantly.

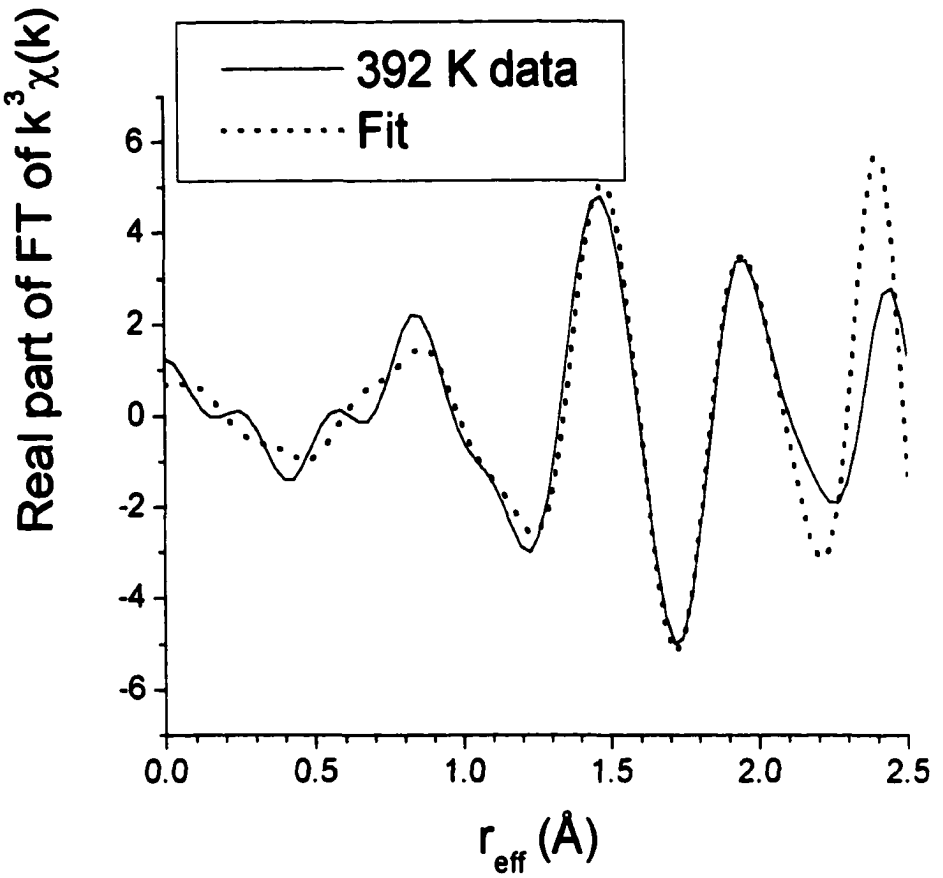

Figure 5.7: Fit of 392 K Ti_2O_3

5.4 Results

The results are summarized in Table 5.5.

Table 5.5: Results of Ti_2O_3 fit. Uncertainties given in parentheses.

S_0^2	0.87(24)
ΔE_0	-2.5 eV
Einstein temp	507(156) K
393 K bond length offset	0.017(22) Å
Thermal expansion coefficient	0.00018(18) K^{-1}
Zero-point C_{31}	-0.0007(10) $Å^3$
Proportionality constant for C_{31}	0.0011(11) $Å^3$ K^{-1}
Zero-point C_{34}	-0.0019(14) $Å^3$
Proportionality constant for C_{34}	0.0018(10) $Å^3$ K^{-1}
ρ_{AXIAL} at 301 K	0.000064(18)
ρ_{AXIAL} at 367 K	0.000060(19)
ρ_{AXIAL} at 392 K	0.000082(17)
ρ_{AXIAL} at 456 K	0.000138(16)
ρ_{AXIAL} at 496 K	0.000149(23)

In Figure 5.8 is plotted, as a function of temperature, the radial asymmetry parameter for the axial Ti-Ti bond. The conductivity of the material [44] is also plotted. The axial radial asymmetry parameter exhibits a sudden jump between 367 K and 456 K as would be expected due to delocalization of electrons in the newly formed metallic bond. (The 392 K data point may show the beginning of this jump, although the rise is still within the estimated error.) As can be seen, the rise in the axial radial asymmetry parameter is

sharper than the conductivity increase. This is in accordance with my model, since ρ reveals delocalization on a nanometer scale, while metallic conductivity requires delocalization on a macroscopic scale. The transition is non-cooperative, beginning as a relatively local phenomenon. In this case, ρ is more sensitive to the onset of the transition than is the conductivity.

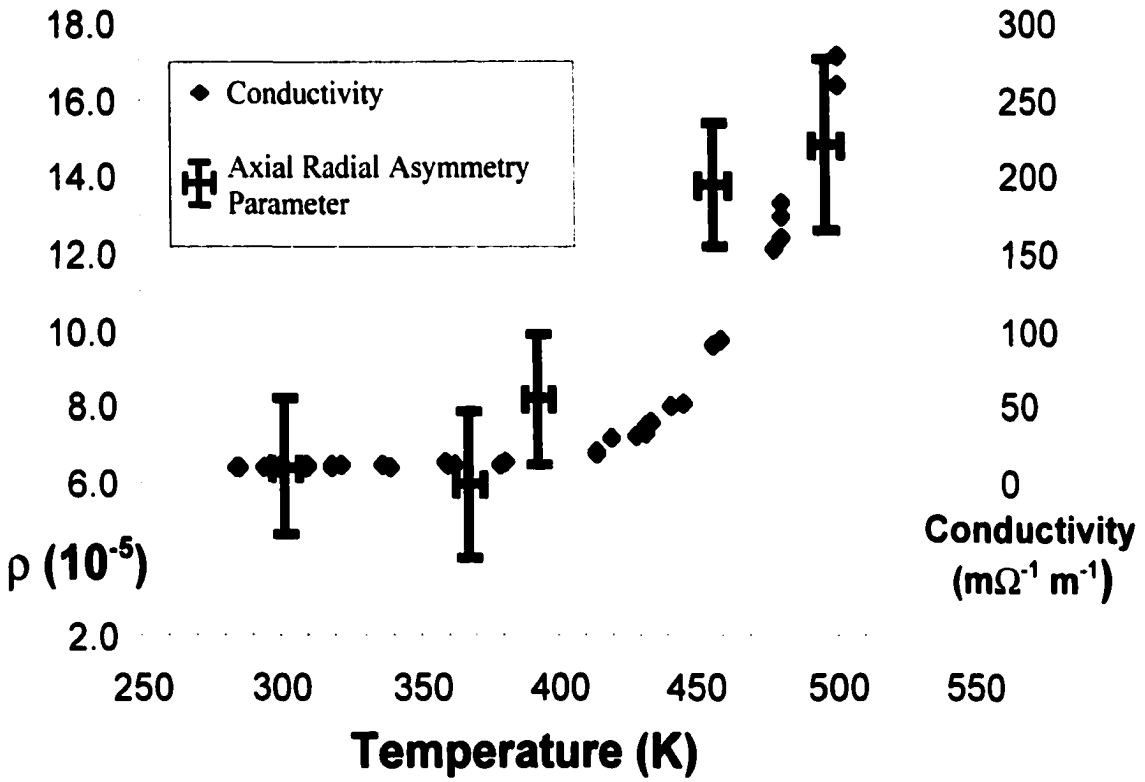

Figure 5.8. Radial asymmetry parameter for axial titanium-titanium bond in Ti_2O_3, along with conductivity for the same material.

In order to determine that it was truly the axial bond responsible for this behavior, rather than an artifact of the fitting constraints, I performed a fit in which the roles of the axial and basal bonds were switched. In other words, the third cumulant for the *basal* bonds was completely unconstrained, while the axial bond was forced to have a temperature

dependence proportional to T^2. This resulted in a substantial degradation of the quality of the fit (χ^2_ν =124; $\mathcal{R}$-factor 0.0091) and no sharp jump in ρ for this bond. The results for this fit are summarized in Table 5.6.

Table 5.6: Results of alternate Ti_2O_3 fit. Uncertainties given in parentheses.

S_o^2	1.08(49)
ΔE_o	-2.5 eV
Einstein temp	372(92) K
393 K bond length offset	-0.100(52) Å
Thermal expansion coefficient	0.00033(40) K^{-1}
Zero-point C_{31}	-0.0072(43) $Å^3$
Proportionality constant for C_{31}	0.0023(31) $Å^3$ K^{-1}
Zero-point C_{33}	0.0029(9) $Å^3$
Proportionality constant for C_{33}	0.0008(9) $Å^3$ K^{-1}
ρ_{BASAL} at 301 K	-0.000005(85)
ρ_{BASAL} at 301 K	0.000006(67)
ρ_{BASAL} at 301 K	-0.000340(391)
ρ_{BASAL} at 301 K	-0.000282(426)
ρ_{BASAL} at 301 K	0.000068(57)

As can be seen, this fit is not only worse in terms of statistical quality, but is also distinctly less physical. The 0.10 Å shorter bond lengths at 393 K than at room temperature for the oxygen octahedron is particularly unlikely. Although it is possible

that this is a false minimum like the one found for certain variations on the primary fit, as a general rule the correct minimum will have a fit quality no better than the false minimum...otherwise the minimization tends to find it, particularly when, as in this case, the parameter values for the false minimum are particularly far from the initial guesses. This implies that even if a more physical fit can be found, it will be a considerably worse fit than the primary one. Therefore, I conclude that the axial bond does in reality show a sharp jump in the radial asymmetry parameter around the onset of the semiconductor-metal transition, and that the basal bond does not (at least to within the uncertainty of the analysis). The results strengthen both the (generally accepted) argument given in [39] that a change in the axial bond is responsible for the jump in conductivity, and the hypothesis from Chapter 2 that changes in electron delocalization are reflected in the radial asymmetry parameter.

With only the results from this chapter, I would consider the evidence for the link between electron delocalization and the radial asymmetry parameter to be weak: even if one is convinced that they both increase together in this particular system, it is not enough of a pattern to declare a connection. To strengthen the link more examples are needed—examples I provide in the next two chapters.

Chapter 6

IODINE: CHARGE TRANSFER

6.1 Structure and Properties

The electronic properties of elemental iodine are in some ways not well understood. Although iodine is often thought of as composed of diatomic molecules, which, in condensed phases, are held together by London dispersion-type forces, some of its properties indicate the reality is more complex. The high reflectivity of single crystals of iodine and the fact that iodine converts into a conducting form under a moderate amount of pressure [45] suggests that solid iodine is "nearly" metallic under ordinary conditions. To explain these properties, it has long been suggested that some degree of charge transfer occurs between iodine molecules in the solid [4]. According to my model, even this limited delocalization should show up as a higher radial asymmetry parameter for solid iodine than for the vapor phase.

6.2 Experimental—Vapor

To produce and contain the vapor, we[10] designed a simple sample chamber. A 40-cm Pyrex cylinder was fitted with chemical-resistant caps, with large Teflon windows. O-rings were used to maintain a tight seal. Inside was placed a small quantity of solid iodine (99.998% pure from Alfa Aesar). Since the vapor pressure of iodine at room temperature is only 0.3 torr, heating tape was then wrapped around the length of the tube and heat guns aimed at each end (to prevent iodine vapor from condensing on the windows). A thermocouple was placed between the heating tape and the Pyrex; a layer of insulation

was then added outside of the heating tape. The temperature was maintained at 340 ± 10 K, with the uncertainty being an estimate of the maximum difference in temperature between the thermocouple, on the outside of the Pyrex tube, and the vapor inside.

L edge data was collected at beamline X23B of the NSLS (see section 5.2 for details of this beamline). The spectra are shown in Figure 6.1a. Oscillations from the L_{II} or L_{III} edges were visible in the L_I pre-edge, so the L_{III} edge was used; the edge region of this spectrum is shown in Figure 6.1b. Some discrepancies between scans can be observed, primarily in amplitude. This may have been due either to variations in the partial pressure of iodine vapor in the sample tube or to nonlinearity in the ion chambers as the intensity of the incident beam changed. Amplitude differences of this type have little effect on the EXAFS spectra, since the data is normalized by the edge jump before analysis. More troubling are the slight (< 2 eV) drifts in phase as well, due to instabilities in the monochromator, since such shifts will degrade the EXAFS spectrum. The spectra shown have already been aligned on the "white line" at 4562 eV by shifting scan 3 by about 1 eV. When this has been done, however, the edge itself is out of alignment. I felt the EXAFS scans were more likely to be in phase if I aligned up the white lines rather than the edges.

---

[10] Richard Krumm, Marten denBoer, James Waters, and myself. Richard Krumm executed the design.

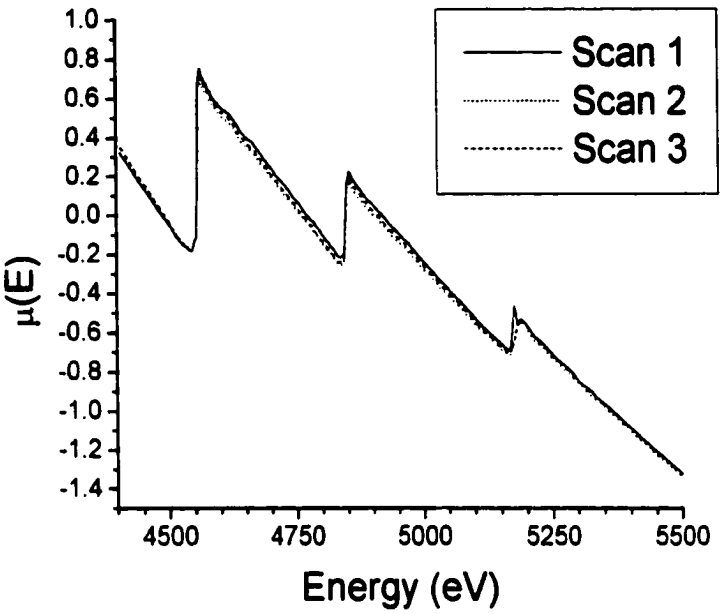

Figure 6.1a: L edges of iodine vapor

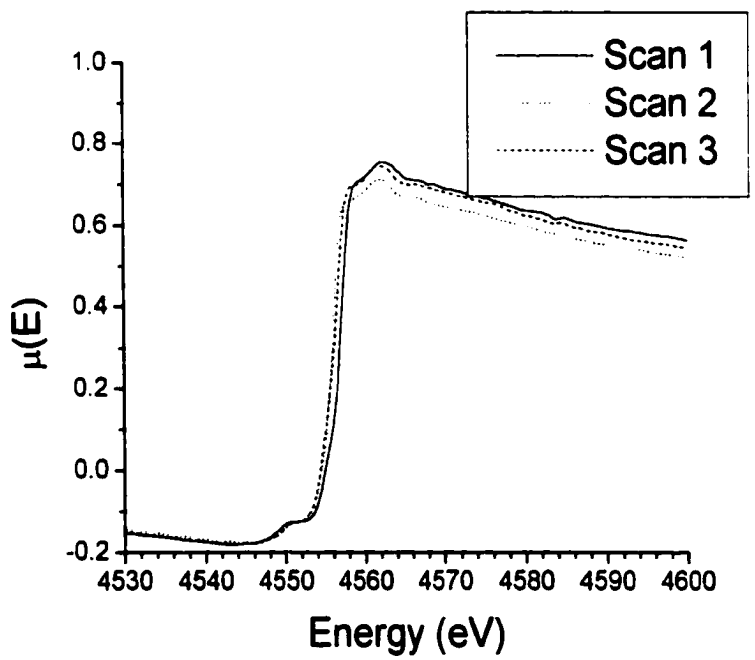

Figure 6.1b: L_{III} edge of iodine vapor

6.3 Analysis—Vapor

The preliminary background subtraction as performed by AUTOBK (r_{bkg} = 1.5 Å) is shown in Figure 6.2, with the resulting graph in *k*-space with *k*-weight 1 (see Appendix A) given in Figure 6.3. The background was subsequently refined by FEFFIT; significant correlations between background parameters and the third cumulant were unfortunately observed (highest correlation = 0.96). Because the background for this spectrum was somewhat problematic, data near the edge was not used, limiting the region analyzed to 4.8 $Å^{-1}$ to 8.3 $Å^{-1}$. The final fit was, however, remarkably stable to small changes in this *k*-range as well as to changes in *k*-weighting and windowing: the radial asymmetry parameter found during these stability checks was always within 1% of the result reported below.

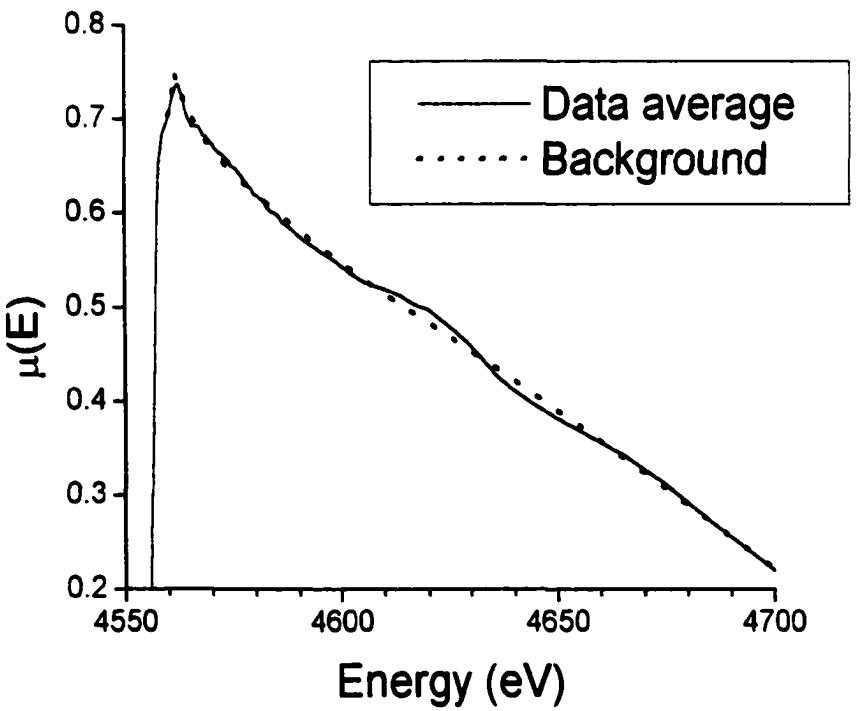

Figure 6.2: Background subtraction for iodine vapor

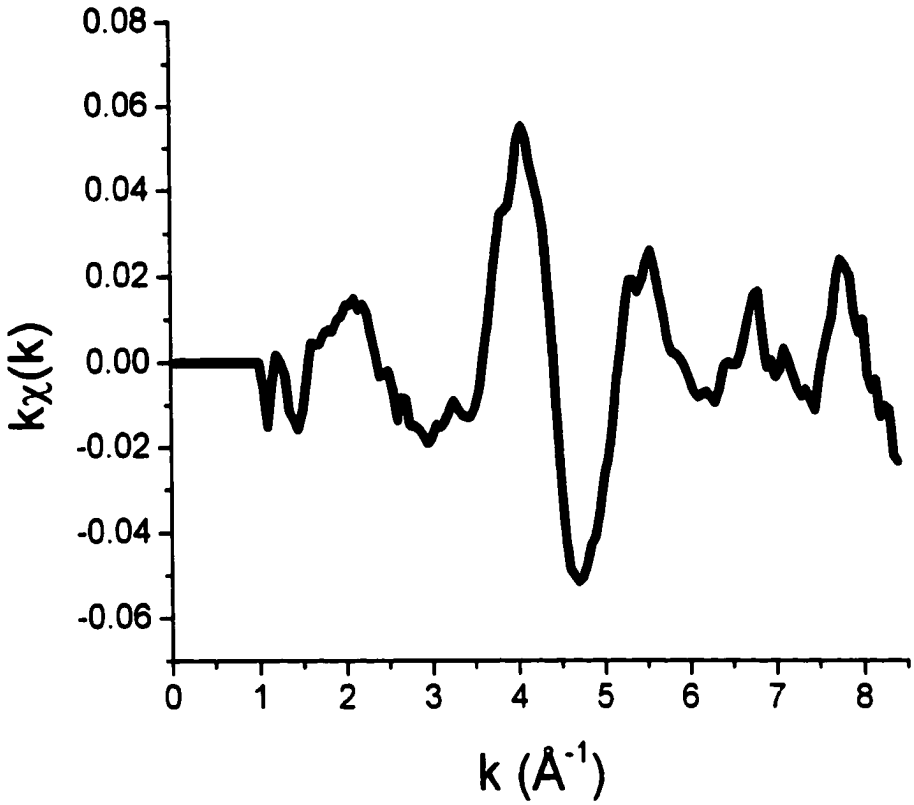

Figure 6.3: *k*-space spectrum for iodine vapor with *k*-weight 1

The theoretical model for iodine vapor was naturally quite simple, consisting of a single direct scattering path at 2.6740 Å, the room-temperature length of the bond in iodine vapor, and the corresponding double path, constrained as described in Appendix C. The fit was conducted from 1.5 Å to 4.0 Å using a Hanning window with sills of width 1.0 $Å^{-1}$. Again, the stability was remarkable; the maximum deviation in the radial asymmetry parameter as a result of changing the fitting range by a small amount was a fraction of a percent.

Only four parameters were fit, the bond length being set at 2.676 Å (the appropriate bond length for 340 K): S_0^2, ΔE_0, and the second and third cumulants. The

first two of these were fit by the method described in Appendix D. Using equation 3.14, there were 8.27 independent points, resulting in 4.27 degrees of freedom. The value found for the third cumulant was not sensitive to the bond length; if the bond length was set to 2.680 Å, the third cumulant changed by only 0.01%.

The reduced χ^2 for the final fit was 0.56, indicating as good a fit as could statistically be expected given the level of white noise (actually, since it is less than one, this suggests we were a bit lucky!). The $\mathcal{R}$–factor was 0.0026, also indicative of an excellent fit. The real part of the Fourier transform and the fit are shown in Figure 6.4. As can be seen, the agreement between model and data is excellent.

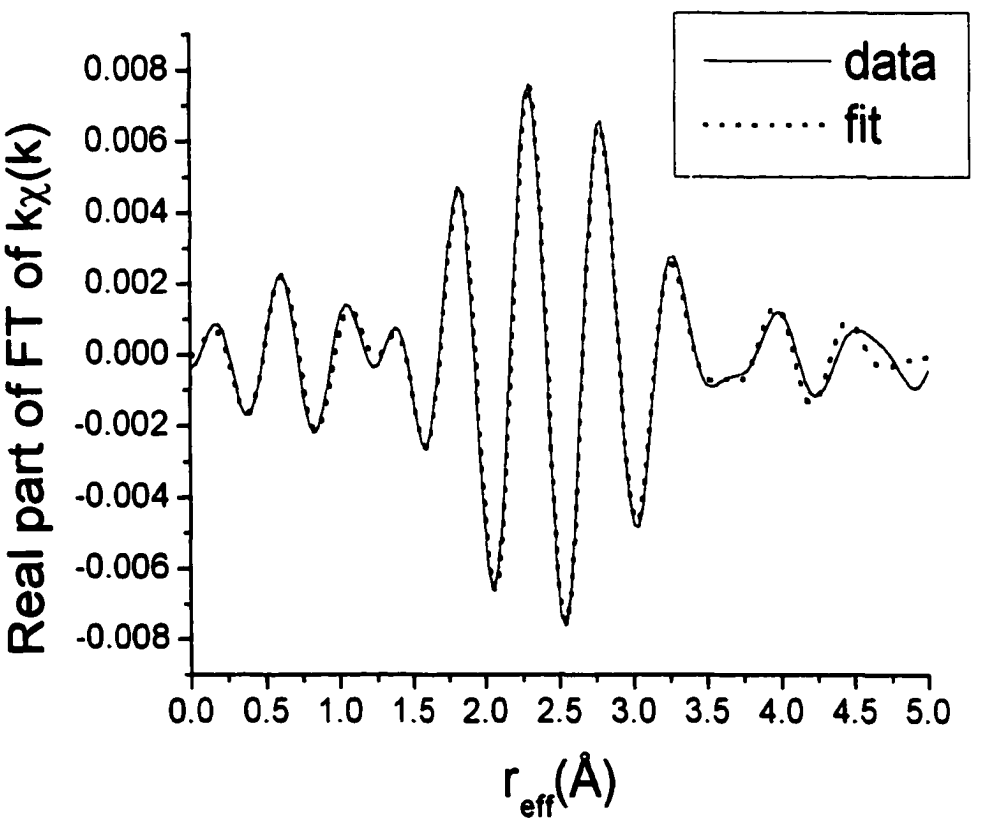

Figure 6.4: Fit of iodine vapor

6.4 Results—Vapor

The results for the fits of iodine vapor are shown in Table 6.1.

Table 6.1: Results of iodine vapor fit. Uncertainties are given in parentheses.

S_0^2	1.0(2)
ΔE_0	-6.3(10) eV
C_2	0.0109(3) Å^2
C_3	0.0027(1) Å^3

6.5 Experimental—Solid

L-edge spectra on the solid were also collected on beamline X23B of the NSLS, using a closed-cycle helium cryostat to control the temperature. The sample was cooled to the desired temperature using a closed-cycle helium cryostat. The iodine was in thermal contact with the cold finger of the cryostat, as was the thermocouple, which always read within 0.5 K of the target temperature. Upon reaching a new temperature, at least five minutes were allowed to elapse for equilibrium to be reached before collecting data. A mechanical vacuum helped maintain thermal isolation, but was apparently imperfect: condensation on the sample was observed. I estimate that the temperature of the sample was within 5 K of the nominal temperature during data collection.

For iodine, the difference in absorption above and below the L_I edge was approximately 0.2. This difference decreased gradually from 0.24 to 0.18 in the course of our measurement, perhaps because of sample movement caused by vibration of the

cryostat. In order to prevent this from having a systematic effect, we collected the data in the following order: 20 K, 120 K, 220 K, 170 K, 70 K, 270 K. Higher temperatures were not achievable because of condensation.

K edge spectra were also collected, but the longer core hole lifetime at the L_I edge yielded higher resolution data. Unlike the vapor, examination of the L_{II} and L_{III} EXAFS showed no detectable oscillations in the L_I pre-edge. This is not surprising, considering the higher degree of disorder inherent in the solid.

The edge region of the 120 K measurement is shown in Figure 6.5. Although a vertical translation is readily evident between the two scans, the phase appears consistent. This was the case for all temperatures.

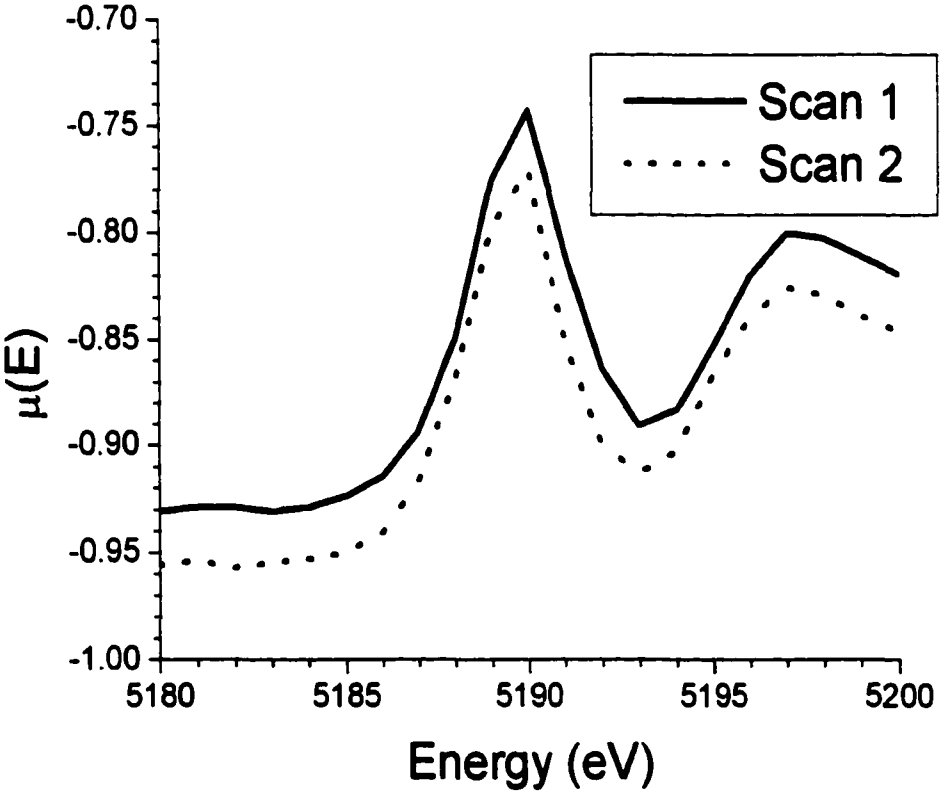

Figure 6.5: 120 K solid iodine L_I edge

6.6 Analysis—Solid

The initial background found by AUTOBK (with r_{bkg} = 1.3 Å) is shown in Figure 6.6. Further refinement was performed later in the fitting process, with the 120 K background refinement being selected for all subsequent fits. This background showed some correlation to S_0^2 (as much as 0.92), but no significant correlations to other fitting parameters.

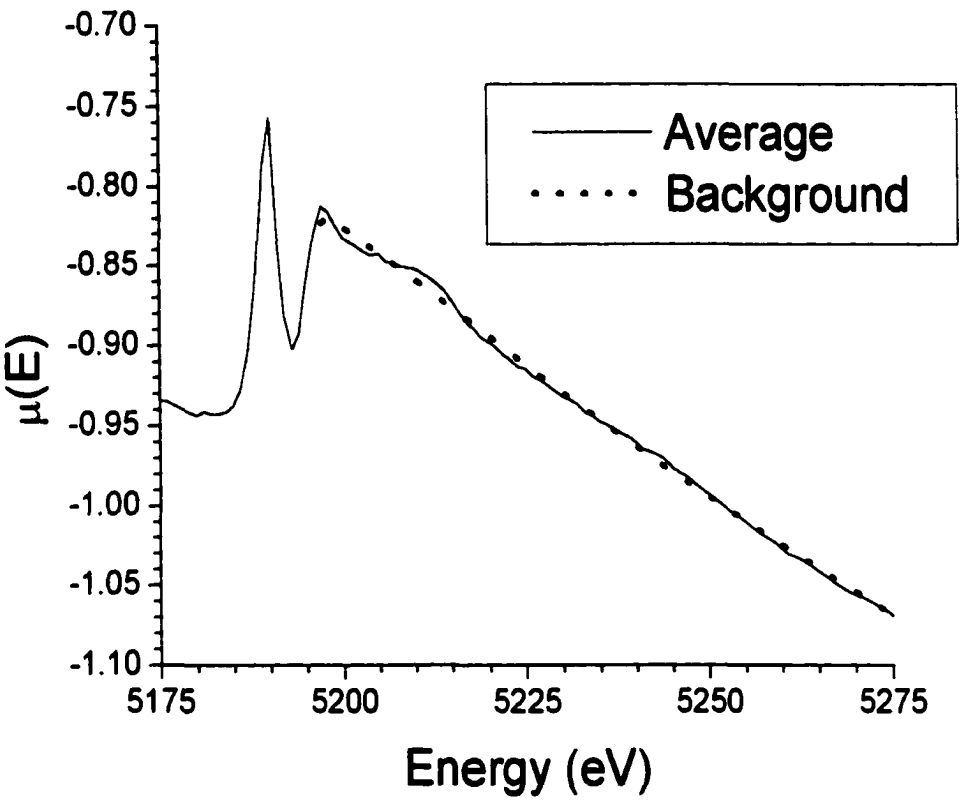

Figure 6.6: Background for 120 K solid iodine

As a basis for the theoretical standard, I used the x-ray diffraction determination of the solid iodine structure at 110 K of von Bolhuis *et al.*[46]. The parameters of this model are given in Table 6.2.

Table 6.2: Model for solid iodine

Space group	C_{mc}
Unit cell dimensions	a = 7.136 Å; b = 4.686 Å; c = 9.784 Å
Iodine (fractional coordinates)	0, 0.1543, 0.1174

The scattering paths identified by FEFF as possibly significant are given in Table 6.3.

Table 6.3: Scattering paths for solid iodine. *Path* is an identification number, *degeneracy* is the number of identical scattering paths with the characteristics shown, r_o is the length of the path in the theoretical model, *type* is explained in Appendix C, and *importance* is the relative amplitude of the path as estimated by FEFF

Path	Degeneracy	r_o (Å)	Type	Importance
1	**1**	**2.7146**	**Direct**	100
2	2	3.4960	Direct	99
3	1	3.9717	Direct	34
4	4	4.2685	Direct	107
5	2	4.3373	Direct	51
6	2	4.4117	Direct	48
7	2	4.6860	Direct	40
8	2	4.9735	Direct	33
9	1	5.4291	Double	10
10	2	5.5921	Triangle	7
11	2	5.5921	Triangle	7
12	4	5.6602	Triangle	10
13	2	5.6891	Direct	21
14	8	6.0881	Triangle	10
15	2	6.1878	Direct	16
16	2	6.1992	Flattened	10
17	2	6.1992	Focused	29
18	2	6.1992	Focused	27
19	2	6.2106	Conjoined	20

20	1	6.2106	Focused	28
21	1	6.2106	Focused	25
22	4	6.2252	Direct	30
23	4	6.3361	Triangle	7
24	4	6.3361	Triangle	7
25	4	6.4360	Direct	27
26	1	6.5483	Direct	6
27	4	6.6757	Triangle	8
28	4	6.6757	Triangle	8
29	4	6.8673	Direct	22
30	2	6.9920	Double	4
31	2	7.0126	Direct	10
32	8	7.1003	Triangle	7
33	3	7.1003	Triangle	7
34	2	7.1360	Direct	9
35	4	7.3503	Triangle	4
36	2	7.4230	Direct	8
37	2	7.4453	Flattened	4
38	2	7.4453	Flattened	11
39	2	7.4453	Flattened	11
40	2	7.4677	Conjoined	6
41	1	7.4677	Focused	8
42	1	7.4677	Focused	8
43	2	7.4926	Direct	8

As can be seen from the table, the relatively low symmetry of the iodine crystal leads to a preponderance of low-degeneracy direct scattering paths. The nearest-neighbor path is well separated from the other paths.

The following relatively simple system of constraints were applied to the fit:

- The first and third cumulants for the nearest-neighbor scattering paths was constrained to the functional forms (4.2) and (4.4), with an Einstein temperature of 308 K, as given by [47]. The zero-point offset and the proportionality constant were found in the fit.
- The bond length for other direct-scattering paths was constrained to have the same fractional change from the model as the nearest-neighbor.
- The third cumulant for other direct-scattering paths was fixed at zero, since the motion of these atoms should be largely uncorrelated.
- The second cumulant for all paths was constrained to an Einstein model with Einstein temperature 308 K.
- S_o^2 was constrained to be the same at all temperatures
- ΔE_0 was found by the method of Appendix D.

There are thus a total of six parameters being varied: S_0^2, ΔE_0, the zero-point offset and proportionality constant for the first cumulant, and the zero-point offset and proportionality constant for the third cumulant.

The k-data (k-weight = 1) is shown in Figure 6.7. The data becomes quite noisy at high-k, so I limited the k-range used for the Fourier transform to 1.7 $Å^{-1}$ to 5.4 $Å^{-1}$. Parameters were fairly stable to small changes in this k-range or to a change in k-

weighting, although the statistical quality of fit tended to degenerate when k_{min} was moved much in either direction. This is not surprising, since lowering k_{min} would incorporate more of the XANES region, while raising it lowers an already narrow *k*-range. Occasionally a false minimum would arise; it was easily identified (and rejected) by a nearest-neighbor bond length greater than that of the room temperature model, a bond length that decreased with increasing temperature, and a third cumulant that also decreased with increasing temperature.

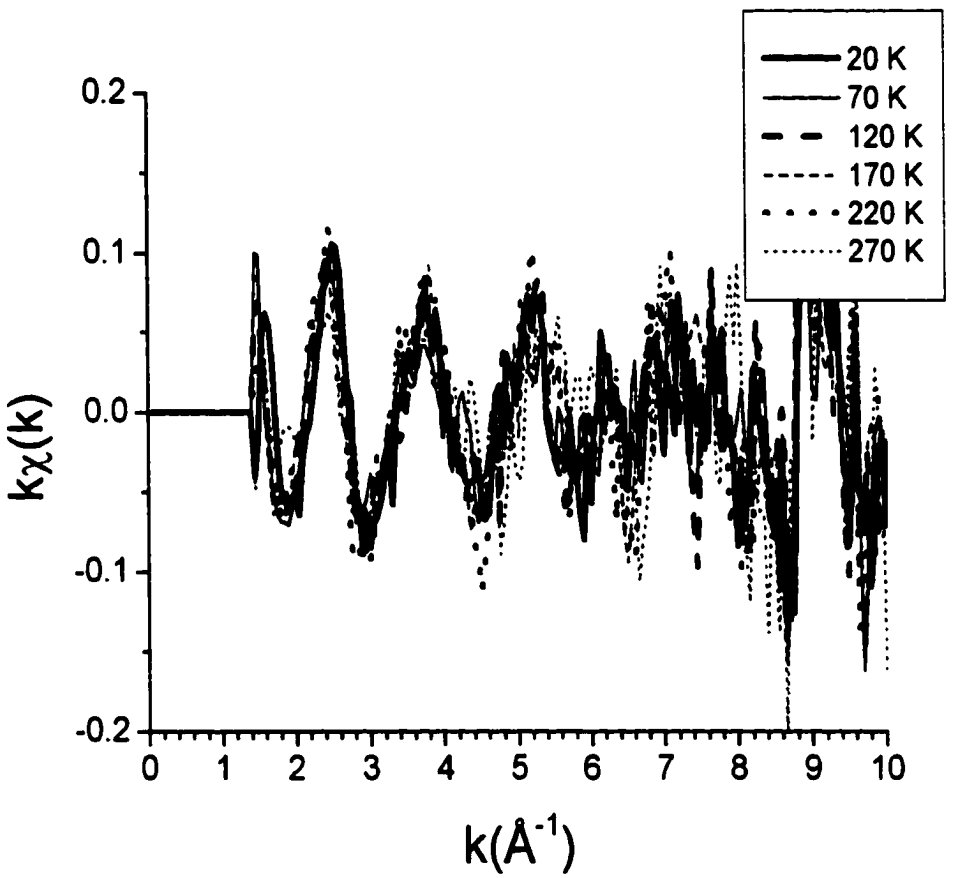

Figure 6.7: *k*-space spectra of solid iodine with *k*-weight 1

After a transform using a Hanning window with sills of width 1 $Å^{-1}$, the real part of the Fourier transform is shown in Figure 6.8. As can be seen from the figure, there are

considerable differences in amplitude between spectra. These differences are correlated to neither temperature nor the sequence of data collection. The source of this systematic error is accordingly uncertain, but the phase (outside of the background region) is fairly consistent between measurements. Since the third cumulant depends on the phase, it may still be determined from this data.

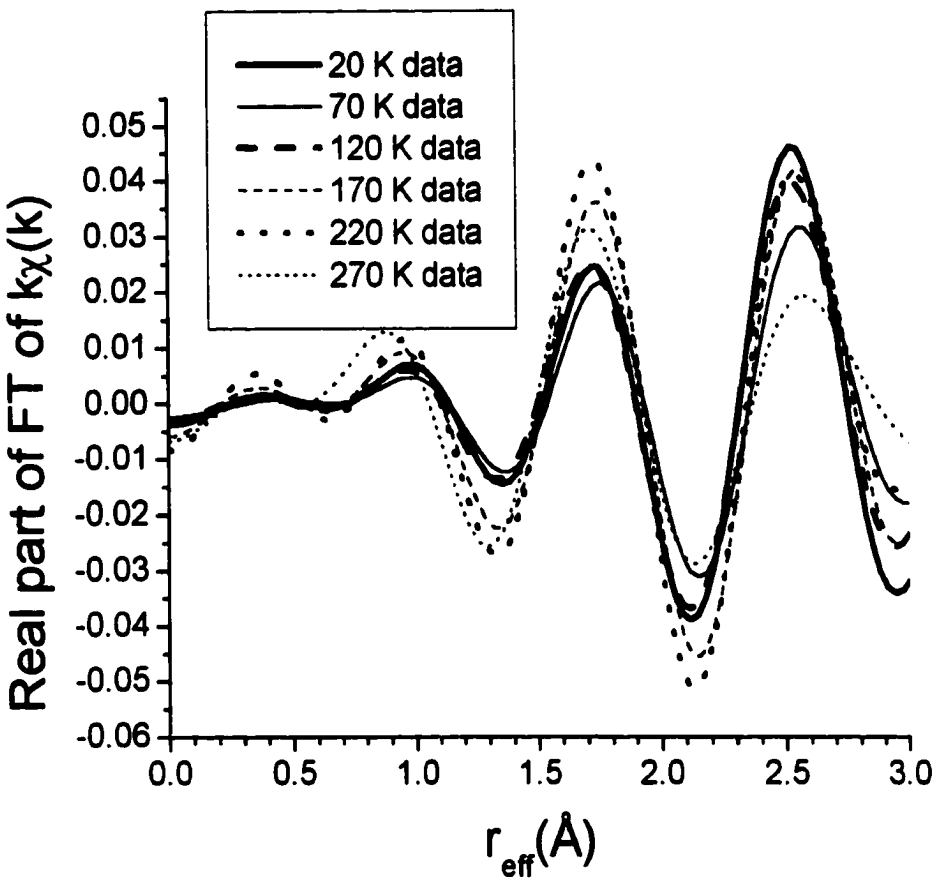

Figure 6.8: Real part of Fourier transform of solid iodine data

The data was fit over a range of 1.7 Å to 2.4 Å, the region in which the nearest-neighbor path is dominant. The fit was reasonably stable to small changes in the *r*-range, although lowering the minimum end of the range resulted in a rapid decrease in the quality of the fit, as expected. The range used gives, according to equation 3.14, 26.0 independent

points. Since six variables are being fit, that gives 20.0 degrees of freedom. The statistical quality of fit is summarized in Table 6.4. The reduced χ^2's, under 25 for all temperatures, suggest a reasonably good fit compared to the white noise. The $\mathcal{R}$–factors, however, often exceeded 0.05, a fairly large mismatch between data and fitted model. This suggests considerable *random* error. The fit for a representative temperature, 120 K, is shown in Figure 6.9a. The fit with the greatest $\mathcal{R}$–factor, for 220 K, is shown in Figure 6.9b for comparison. Even in the latter case, the phase is fairly accurate, with the discrepancy almost entirely in the amplitude.

Table 6.4: Statistical quality of solid iodine fits

Temperature (K)	χ^2	Reduced χ^2	$\mathcal{R}$–factor
20	11.1	3.3	0.0270
70	68.2	20.5	0.0781
120	25.9	7.8	0.0506
170	52.8	15.8	0.0326
220	64.5	19.4	0.0837
270	35.6	10.7	0.0563
Overall	**258.1**	**12.9**	**0.0547**

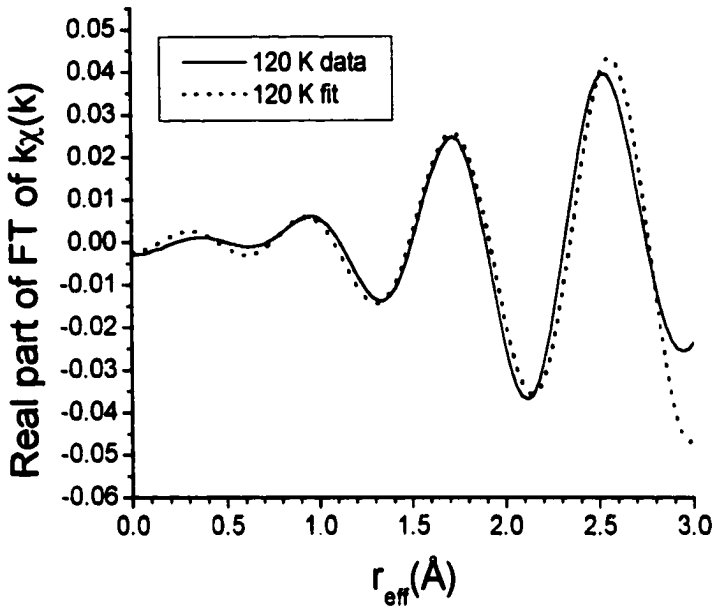

Figure 6.9a: Fit of iodine solid at 120 K

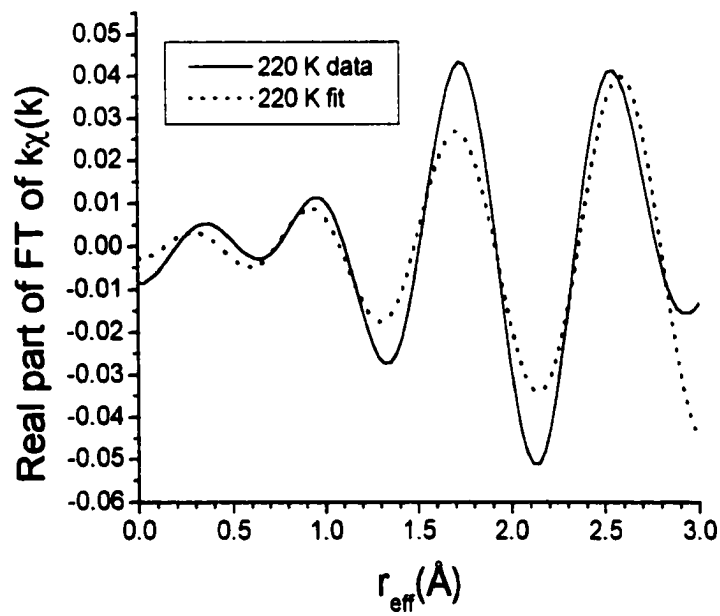

Figure 6.9b: Fit of iodine solid at 220 K

6.7 Results—Solid

The results are summarized in Table 6.5.

Table 6.5: Results of solid iodine fit

S_0^2	0.62(6)
ΔE_0	-6.3(40) eV
Difference in zero-point bond length relative to model	-5.0(2.2)%
Proportionality constant for temperature-dependence of fractional changes in bond length	0.024(15)
Zero-point C_{31}	0.0073(37) Å^3
Proportionality constant for temperature-dependence of C_{31}	0.0006(5) Å^3

From this data, it can be seen that the temperature dependence of the cumulants is fairly uncertain. This is not surprising, given that there is no clear temperature dependence in the *k*-spectra and that, since all the data was collected below the Einstein temperature of iodine, the temperature dependence should be small in any case. The zero-point value of the third cumulant, on the other hand, is relatively well determined and proved stable to changes in fitting ranges, constraint strategies, and other changes to the fit. The temperature dependence of the bond length as found by the fit is shown in Figure 6.10.

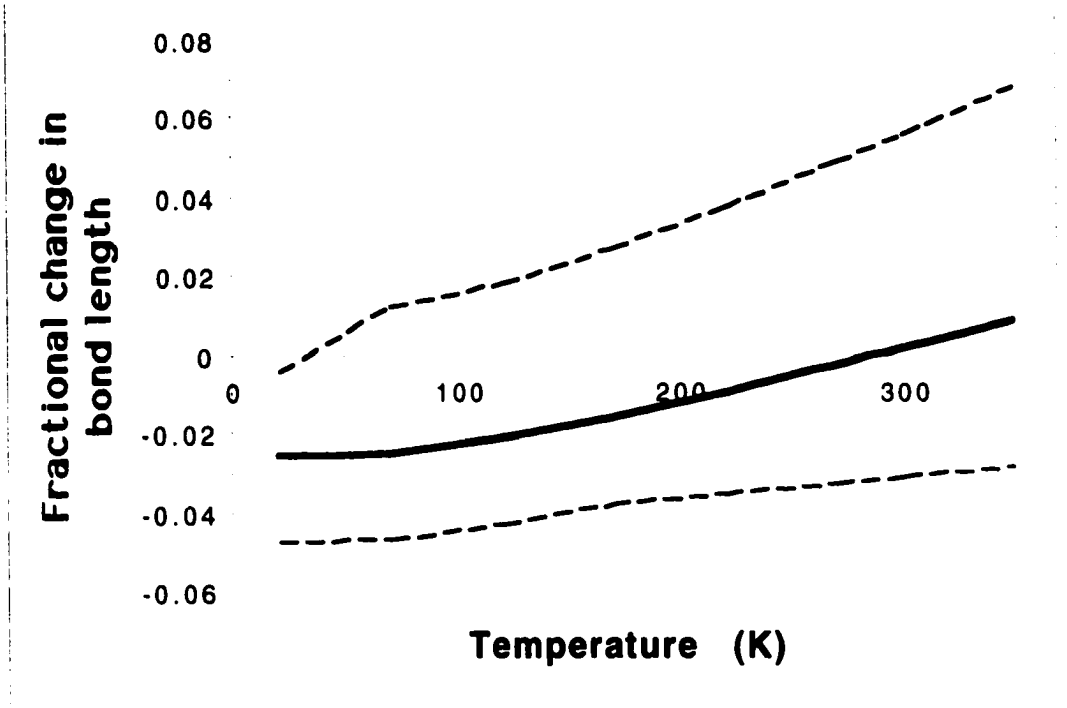

Figure 6.10: Temperature dependence of bond length in solid iodine. Solid line is the best-fit; the dashed lines give the maximum and minimum values consistent with the results of the fit.

6.8 Comparison of Vapor and Solid Results

Comparing the fits for solid and vapor iodine, it is clear that the third cumulant for the nearest-neighbor in the solid is substantially larger than the corresponding value in the vapor. In Figure 6.11, an extrapolation of the solid iodine radial asymmetry parameter is compared to the vapor determination. Even with the large uncertainty in the temperature dependence of the third cumulant for the solid iodine, the radial asymmetry parameter for the solid is unambiguously larger than that for the vapor at the same temperature. While it is probable that static disorder in the solid (perhaps due to a small amount of hydration) makes some contribution to this difference, it is unlikely to account for the entire increase observed, which is at least 150%. Indeed, the magnitude of this increase is similar to that

observed for the semiconductor-metal transition in titanium sesquioxide, and the bulk of it is likely due to a similar effect: electron delocalization in the solid phase, probably via the charge transfer mechanism.

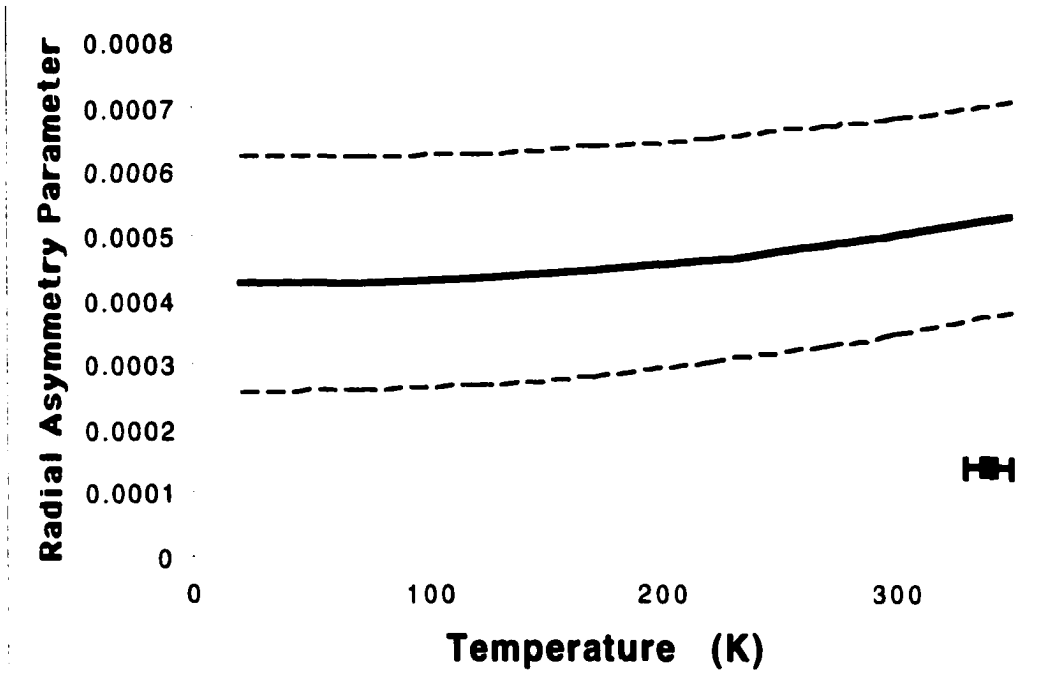

Figure 6.11: Radial asymmetry parameter in iodine. The solid line is the best-fit for the solid phase; the dashed lines give the maximum and minimum values consistent with the fit. The individual data point at the lower right is the value from the vapor fit, with the uncertainty in the temperature of that measurement shown. The uncertainty in the radial asymmetry parameter of the vapor is too small to appear at this scale.

Chapter 7

BUTYL BROMIDES: DELOCALIZATION WITHIN MOLECULES

7.1 Structure and Electronic Delocalization

It has long been known that the carbon radicals and carbocations formed by the dissociation of alkyl halides are stabilized by the presence of additional alkyl groups attached to the carbon bonded to the halogen [48]. Stabilization of bond stretching in the alkyl halides themselves, however, has been much more difficult to determine experimentally (subtle changes in molecular geometry have been used to provide estimates for related systems [49]). Stabilization in either case is due to the delocalization of electron density from neighboring C-H bonds; the electron density can be shared through direct overlap of molecular orbitals (hyperconjugation), or through field and inductive effects. Perhaps due to the interaction of these mechanisms, the effect of alkyl substituents is different for cations, radicals, and anions [50]. By using the radial asymmetry parameter to determine electron delocalization in the C-Br bond, this study provides the first experimental determination of the relative alkyl-group stabilization of the parent alkyl halide compounds themselves.

In *n*-butyl bromide (Figure 7.1a), the bromine is bonded to a carbon atom attached to a single propyl group and the effect of both hyperconjugation and the inductive effect is relatively small. In *t*-butyl bromide (Figure 7.1b), the bromine is bonded to a carbon attached to three methyl groups, significantly increasing the amount of hyperconjugation, as well as the inductive effect. *Sec*-butyl bromide (Figure 7.1c) is an interesting intermediate case: the availability of two neighboring alkyl groups (one methyl, one ethyl) provides an amount of hyperconjugation intermediate between the *n*- and *t*-

isomers, while it has been suggested that the single-chain structure of the molecule limits the inductive effect to essentially that found in the *n*- isomer [51].

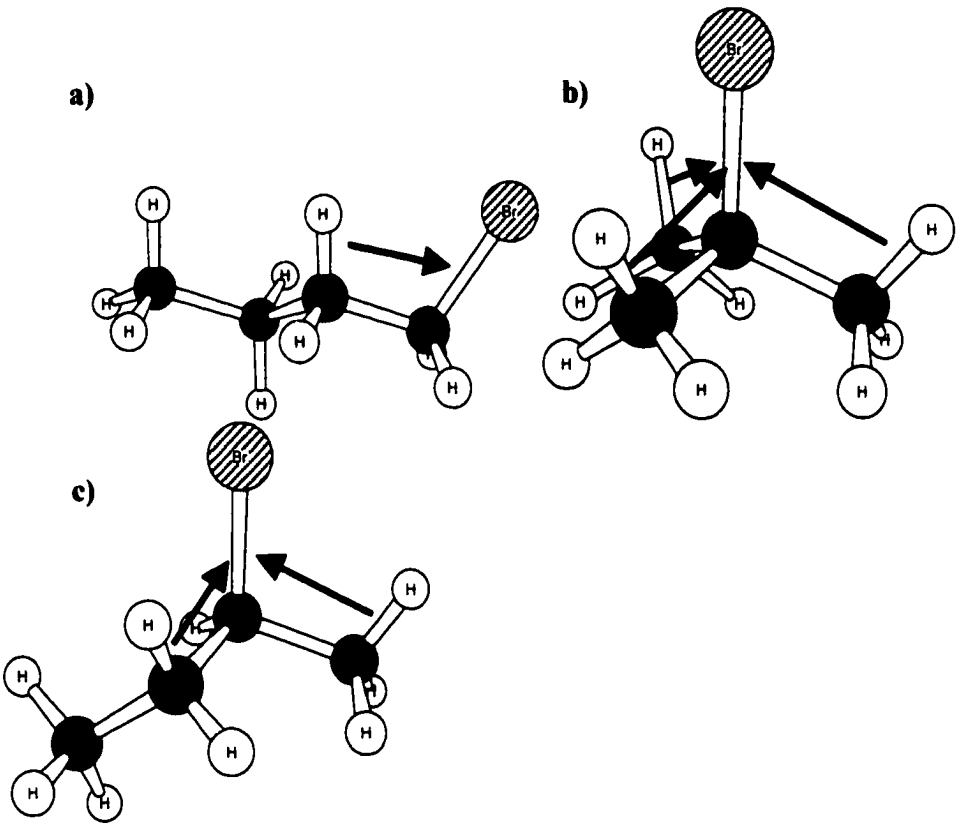

Figure 7.1: Isomers of butyl bromide. Hyperconjugation interactions are shown with arrows. **a)** *n*-butyl bromide; **b)** *t*-butyl bromide; **c)** *sec*-butyl bromide.

Bond dissociation energies provide some suggestion that the mechanism of stabilization is different for radicals than for cations. Data for *heteropolar* (cation-forming) and *homopolar* (radical-forming) bond dissociation is given in Table 7.1 [52]. Although bond dissociation energies for *n*-butyl bromide and *sec*-butyl bromide are not available in the literature, *n*-propyl bromide is structurally quite similar to *n*-butyl bromide and isopropyl bromide is structurally similar to *sec*-butyl bromide.

Table 7.1: Bond dissociation energies for alkyl bromides

Isomer	Homopolar Bond Dissociation Energy (kcal mol^{-1})	Heteropolar Bond Dissociation Energy (kcal mol^{-1})
n-propyl bromide	68.0	178
isopropyl bromide	68	164
t-butyl bromide	66.1	149

Interestingly, homopolar dissociation (radical formation) shows similar stabilization for the *n*- and *iso*- isomers, with a greater stabilization for the *t*- isomer, while heteropolar dissociation (cation formation) shows the *iso*- isomer intermediate between the other two. If [51] is correct, then this could be explained by hyperconjugation being the dominant stabilizing effect for cations, and the inductive effect being the dominant stabilizing effect for radicals.

7.2 Experimental

The butyl bromide isomers used for this experiment are liquids at STP, but in the liquid phase, the electron delocalization *within* molecules would be considerably modified by the interactions *between* molecules. This can be avoided by measuring the molecules in the vapor phase, with the added advantage of not having to worry about a solvation shell in the analysis. Since the vapor pressure of butyl bromides is substantial at room temperature, we used modifications of the apparatus described in the previous chapter to collect data on these substances. Alkyl halides are considerably less reactive than halogen vapors; therefore we initially used stainless steel tubes with plastic and Parafilm

windows. The *sec*-butyl bromide spectra did not provide stable fits, however, so we later repeated the experiment for that isomer using a glass tube with Teflon windows (similar to that described for iodine in the last chapter, but shorter, due to the greater vapor pressure of the butyl bromide). Bromine K edge x-ray absorption measurements were then performed at beamline X23A2 of the NSLS. This beamline uses a Golouchenko-Cowan type Si (311) monochromator, detuned to 50% intensity to eliminate harmonics.

The white-line region of the *n*-butyl bromide spectrum is shown in Figure 7.2. As is often the case, the two scans are translated vertically, but have the same phase. This was also the case for the *t*-butyl bromide isomer.

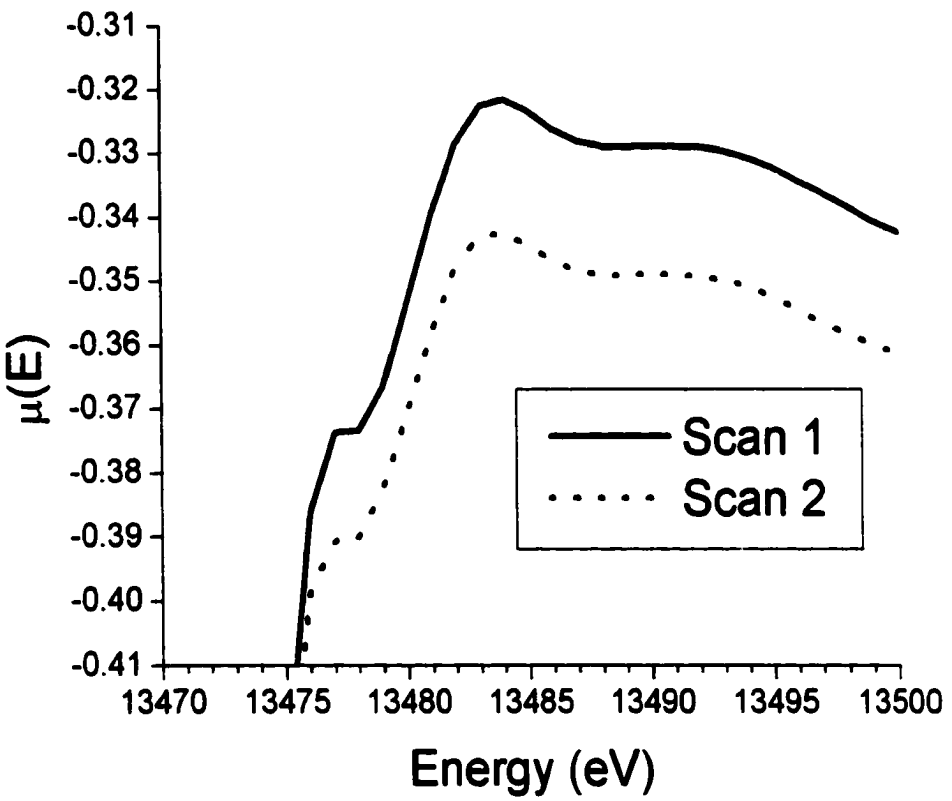

Figure 7.2: White line of *n*-butyl bromide spectra

7.3 *Analysis*[11]

Initial background subtraction was performed using AUTOBK with r_{bkg} = 1.2 Å. The results for the *t*-butyl bromide isomer are shown in Figure 7.3 FEFFIT was then used to further refine the background. Since the materials are isomers of each other and the background is due to the individual atoms, a single background refinement should be suitable for all three isomers. The background for the *sec*-butyl isomer, as refined at an intermediate stage in the fit, was used for this purpose. These background parameters showed no significant correlations with the parameters being fit.

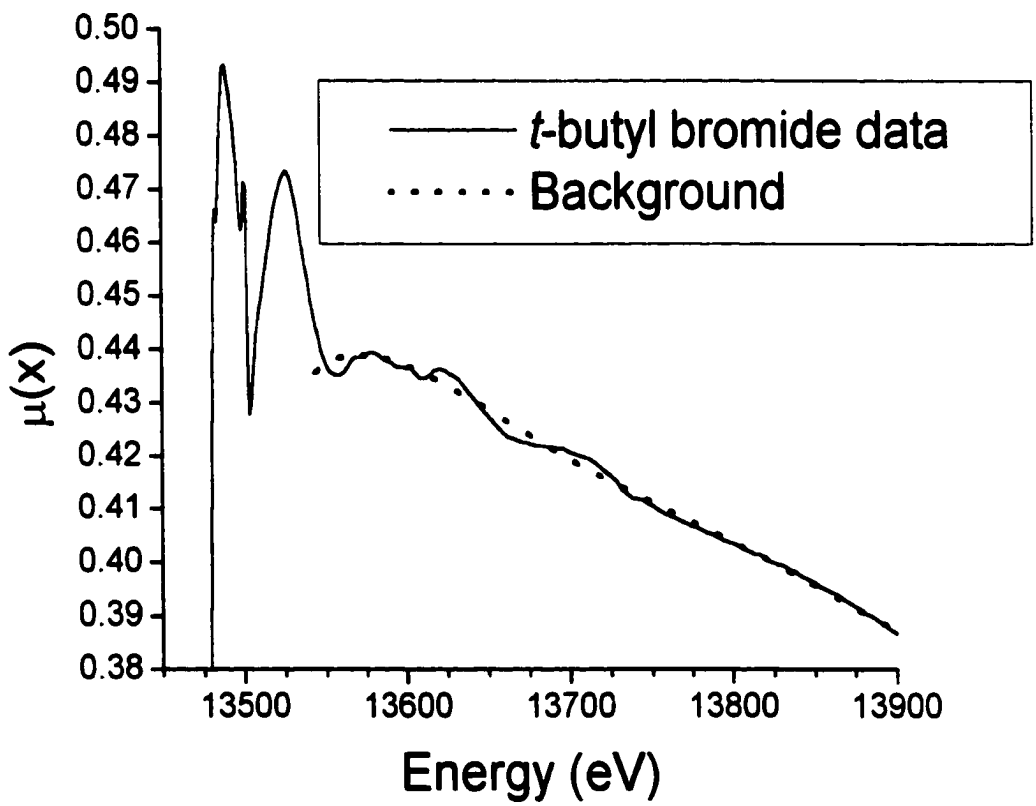

Figure 7.3: Background for *t*-butyl bromide

[11] Preliminary analysis was performed by Jihane Mimih under my direction. I then refined the fits to the form discussed here.

For a theoretical model, we used the simplest model available in the HYPERCHEM software; this model simply substitutes standard bond lengths and angles. It should be noted that the butyl bromide isomers can adopt different conformations, which could be an issue for EXAFS analysis beyond the nearest-neighbor. For *t*-butyl bromide, this does not affect the EXAFS analysis: the radial distribution function about the bromine is independent of the conformation adopted, aside from a negligible contribution from scattering off of the hydrogen atoms. The possible conformations of the *n*-butyl bromide isomer make no difference to the first two carbon neighbors of the bromine atom, but the third can adopt various positions. For the FEFF calculation, we assumed the most stable "anti" conformation, in which the carbons and the bromine adopt a coplanar zigzag pattern. The *sec*-butyl bromide is the most problematic case. Once again, the third nearest carbon to the bromine can assume different conformations, but this time there is no pure anti conformation; either all the carbons can be in the coplanar zigzag pattern, with the bromine in a "gauche" position sixty degrees out of the plane, or the three carbons and the bromine can be coplanar, with the methyl group in the gauche position. Since we were primarily interested in the C-Br bond, we simply decided not to fit beyond the second nearest carbon. In addition, since for all isomers rotation around C-C bonds would tend to reduce the already miniscule hydrogen scattering contribution, we ignored all paths due to the hydrogens.

The resulting paths are given in Table 7.2.

Table 7.2: Scattering paths for butyl bromides. *Path* is an identification number, *degeneracy* is the number of identical scattering paths with the characteristics shown, r_o is the length of the path in the theoretical model, *type* is explained in Appendix C, and *importance* is the relative amplitude of the path as estimated by FEFF.

Isomer	Path	Scattering element(s)	Degeneracy	r_o (Å)	Type	Importance
n-butyl bromide	**1N**	**C**	**1**	**1.910**	**Direct**	100
	4N	C	1	2.825	Direct	34
sec-butyl bromide	**1S**	**C**	**1**	**1.910**	**Direct**	100
	5S	C	2	2.825	Direct	
t-butyl bromide	**1T**	**C**	**1**	**1.919**	**Direct**	100
	2T	C	3	2.825	Direct	112

As can be seen from the table, in this model the first two carbon neighbors for the bromines in each isomer are the same. In the actual molecules, there can be expected to be small differences in the C-Br distances for the different isomers; these must be found during fitting.

The constraints used follow:

- The third cumulant for the second nearest-neighbor in each isomer was constrained to the third cumulant for the nearest-neighbor in that isomer. In these molecules the geometry is such that this is a reasonable approximation: most of the asymmetry in the PDF of the bromine relative to the second carbon is due to stretching of the C-Br bond.
- The second cumulant for the nearest-neighbor in the *n*- and *sec*- isomers were constrained to be the same. This was an empirical decision; the fit was not

improved by allowing them to vary separately. A good fit could not be achieved if the *t*- isomer was also constrained to the same value.

- S_0^2 was constrained to be the same for all isomers, and was determined by the method described in Appendix D.
- ΔE_0 was eventually constrained to be the same for all isomers, but not without considerable investigation. Initially, I attempted to find a separate value for each isomer using the method of Appendix D. Unfortunately, ΔE_0, the first cumulant, and the third cumulant are entangled in a complex fashion: the intersection point of the ΔE_0 versus the third cumulant lines depends on the value of the first cumulant. If the first cumulant is allowed to be fit, then for the *sec*- isomer the lines do not intersect at all, while for the *t*- isomer they intersect at all values. Fortunately, the *n*-isomer did have a consistent intersection at –9.0 eV, whether ΔE_0 was plotted versus the first cumulant or versus the third cumulant. I accordingly attempted constraining *all* ΔE_0's to –9.0 eV. The statistical quality of fit improved, so this was the option I adopted.

This left us with sixteen unconstrained parameters: six first cumulants, five second cumulants, three third cumulants, S_0^2, and ΔE_0.

The *unweighted* spectra in *k*-space are shown in Figure 7.4. As can be seen, the *t*-butyl bromide spectrum has a very different *k*-space dependence from the other two isomers. Aside from some glitches above $k = 15$ Å, the most dramatic difference is the slow decrease in amplitude with increasing *k* relative to the other two spectra. This is due

to the much lower degree of disorder associated with the relatively rigid *t*-butyl isomer. Although not unexpected, this difference does raise a difficult issue: the *k*-weighting (see Appendix A for a discussion of this concept) most appropriate for the *t*-butyl isomer is clearly lower than that appropriate for the other two. Yet applying different *k*-weights to different spectra runs the risk of introducing spurious differences between the fits; there are also difficulties in maintaining an appropriate contribution from each spectrum to parameters in common (such as S_0^2) when the spectra are weighted differently. For these reasons, I decided to apply a uniform *k*-weight of 2. As it turned out, the final fit was not at all sensitive to the choice of *k*-weight, and gave similar results even if different spectra were assigned different *k*-weights.

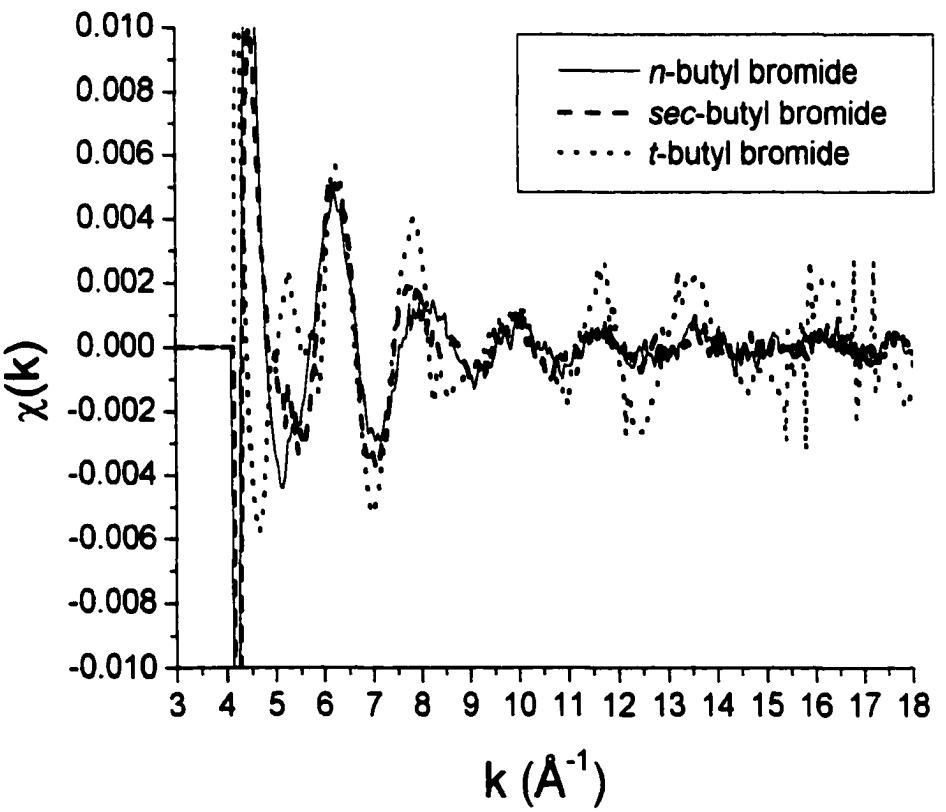

Figure 7.4: Unweighted *k*-spectra for butyl bromide spectra

The spectra with a *k*-weight of 2 are shown in Figure 7.5. The *k*-range of the fit was chosen to be 4.6 $Å^{-1}$ to 12.7 $Å^{-1}$, avoiding the glitches at high *k*. The final fit was stable to small changes in *k*-range, changes in *k*-weight, and changes in the window used.

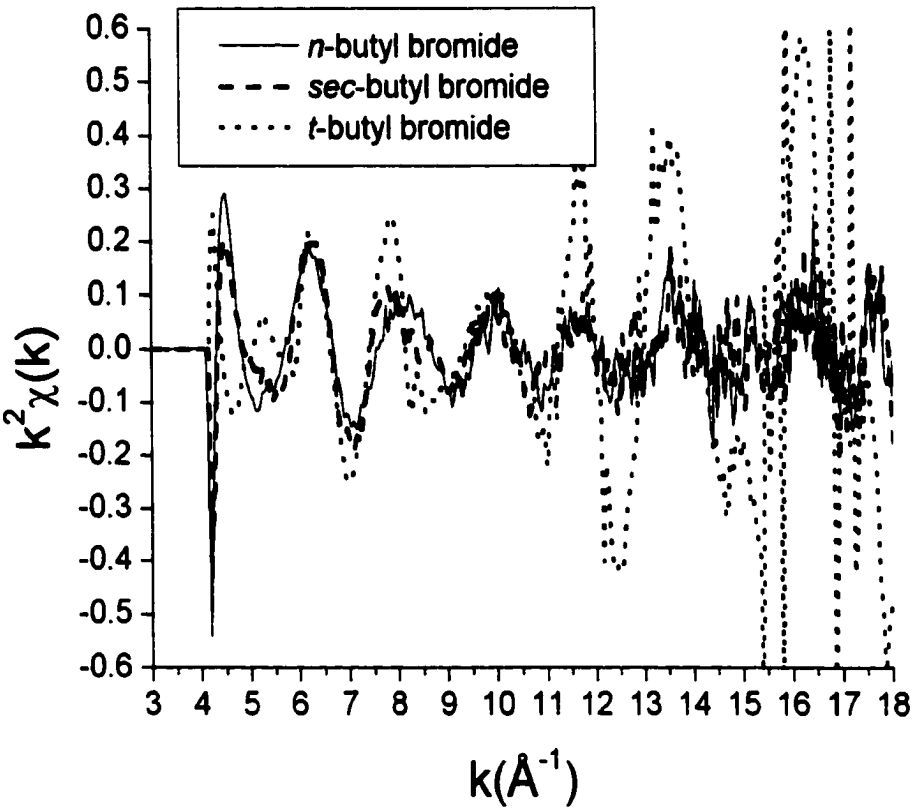

Figure 7.5: *k*-spectra for butyl bromide spectra with *k*-weight 2

The real part of the Fourier transform of the data, using a Hanning window with sills of width 1.0 $Å^{-1}$, is shown in Figure 7.6. Despite the considerably greater amplitude for the *t*-butyl isomer on certain peaks of the *k*-graph, in the region where the nearest-neighbor path is dominant, this isomer shows only a moderate increase in amplitude. In fact, the peak at 1.6 Å is also noticeably narrower than the corresponding peak in the other isomers. This combination is indicative of a smaller second cumulant and thus a lower

vibrational amplitude, as would be expected from the rigidity of the structure. The peak near 2.5 Å, on the other hand, is dominated by the next-nearest carbon neighbor, which has a greater degeneracy in the *t*-butyl bromide isomer and thus should have a greater amplitude. For the fit, we used a range from 1.2 Å to 2.5 Å. The fit was stable relative to small changes in this range.

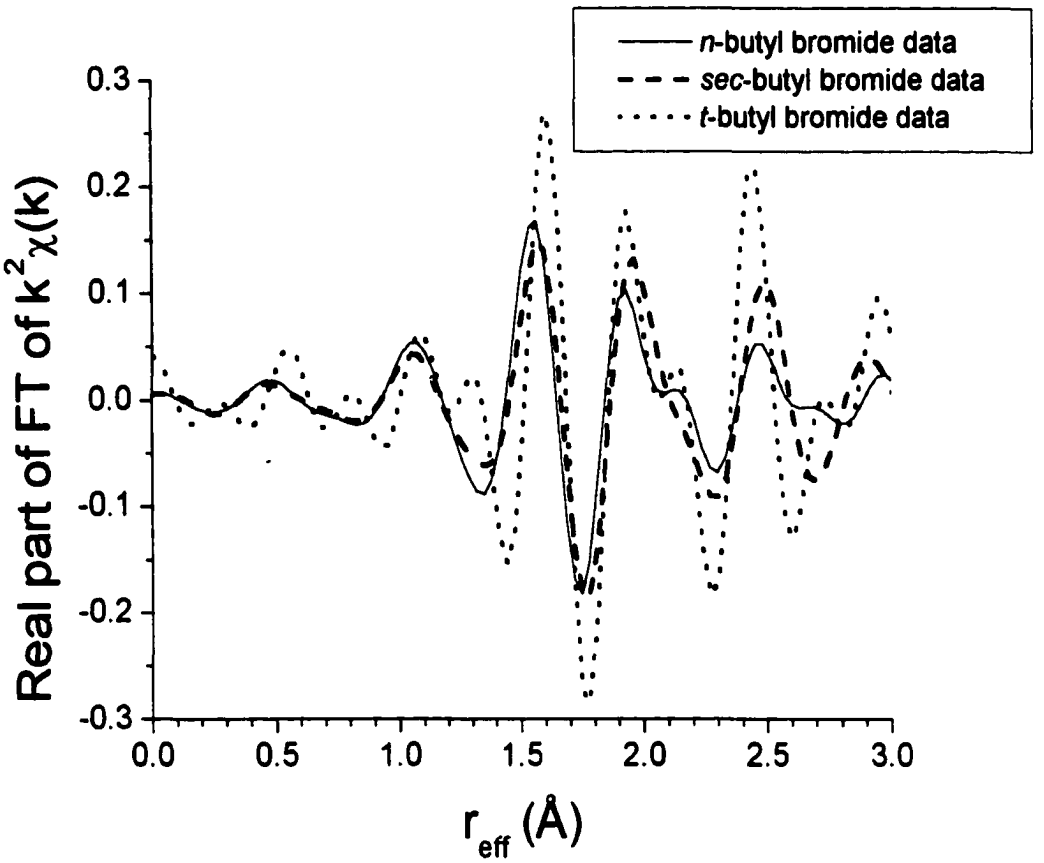

Figure 7.6: Real part of Fourier transform of butyl bromide data

We thus had 25.8 independent points, which, with sixteen parameters fit, left us with 9.8 degrees of freedom. The statistical quality of fit is summarized in Table 7.3. The reduced χ^2 is 6.7, with all fits below 15, suggesting a good fit relative to the white noise. The $\mathcal{R}$ -factor is 0.0096, indicating a fairly good absolute fit between data and fitted model. It

should be noted that the *t*-butyl bromide isomer fit shows lower statistical quality than the other two, although the values are still fairly good. This is probably related to the difficulty with the amplitude (see section 7.4). The graphs of the Fourier transforms for the fits are shown in Figure 7.7. In agreement with the statistical measures, all three fits appear quite good over the range fitted.

Table 7.3: Statistical quality of butyl bromide fits

Isomer	χ^2	Reduced χ^2	$\mathcal{R}$–factor
n-butyl bromide	3.0	0.9	0.0011
sec-butyl bromide	18.2	5.6	0.0074
t-butyl bromide	44.7	13.7	0.0202
Overall	**65.9**	**6.7**	**0.0096**

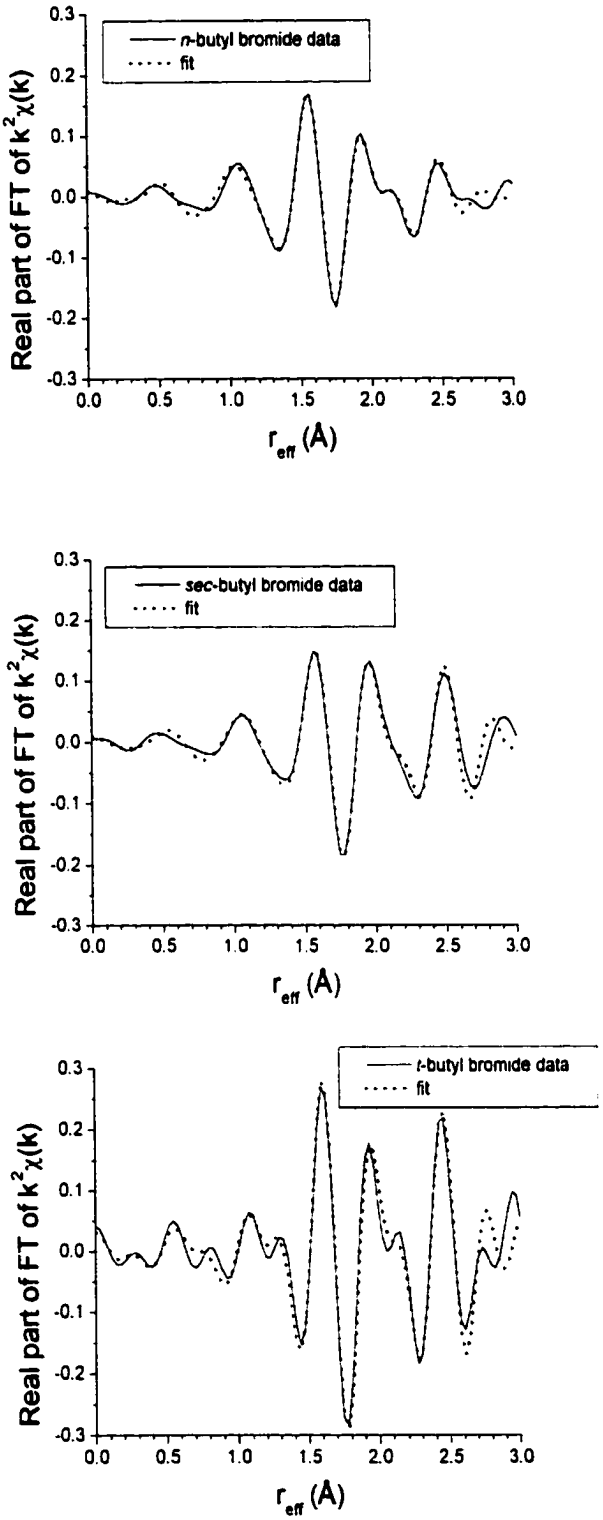

Figure 7.7: Butyl bromide fits

7.4 Results

The results are summarized in Table 7.4:

Table 7.4: Results of butyl bromide fits. Uncertainties are given in parentheses.

S_0^2	0.85(2)
ΔE_0	-9.0(6) eV
C-Br bond length for *n*-butyl bromide	1.872(10) Å
C-Br bond length for *sec*-butyl bromide	1.885(10) Å
C-Br bond length for *t*-butyl bromide	1.952(10) Å
C-Br C_2 for *n*- and *sec*-butyl bromide	0.0017(3) Å^2
C-Br C_2 for *t*--butyl bromide	-0.0025(4) Å^2
C-Br ρ for *n*-butyl bromide	-0.000171(27)
C-Br ρ for *sec*-butyl bromide	-0.000200(27)
C-Br ρ for *t*-butyl bromide	-0.000060(20)
Second neighbor distance in *n*-butyl bromide	2.759(18) Å
Second neighbor distance in *sec*-butyl bromide	2.759(12) Å
Second neighbor distance in *t*-butyl bromide	2.769(11) Å
Second neighbor C_2 for *n*-butyl bromide	0.0030(22) Å^2
Second neighbor C_2 for *sec*-butyl bromide	0.0023(13) Å^2
Second neighbor C_2 for *t*-butyl bromide	0.0005(8) Å^2

The most troubling aspect of this fit is the second cumulant for the C-Br bond in *t*-butyl bromide. The negative value is, of course, nonsensical, indicating a serious problem with

the amplitude portion of the fit. Although the negative value is clearly incorrect, the effect may be systematic across fits; the second cumulants for the other isomers are somewhat small for room temperature measurements of a soft bond like that typically formed with bromine. Possible sources of error include a problem with the background subtraction.

Does this evident failure in the determination of the second cumulant invalidate the results for the third? Not necessarily, since errors which affect amplitude and phase variables tend to be of different types. Although FEFFIT reported moderate correlations between the first and third cumulants (less than 0.92), correlations between the second cumulants and other variables were less than 0.3 (although there certainly would have been correlation with S_0^2 if it had not been refined in a previous step). This suggests that errors in the determination of second cumulant do not impact the determination of other variables significantly.

The third cumulants are also negative, which, although not impossible, is not likely. Our investigations of other materials suggest that this is may be due to a systematic error in FEFF, and does not impair *comparison* of cumulants in similar spectra (see Chapter 4).

Thus, I believe that our result of a greater radial asymmetry parameter for the carbon-bromine bond in *n*-butyl bromide than that in *t*-butyl is valid. For *sec*-butyl bromide, on the other hand, the result is indistinguishable from the *n*-butyl isomer to within our estimated uncertainty. Comparison with Table 7.1 shows that the stabilization of the C-Br bond stretch is qualitatively similar to the stabilization found for radicals, and dissimilar from that found for cations. If [51] is correct, then the inductive effect, rather

than hyperconjugation, is probably not the dominant stabilizing factor in the neutral molecules.

Chapter 8

CONCLUSIONS

Using the curve-fitting method of EXAFS analysis, I have determined changes or differences in the asymmetry of the PDF for four systems: elemental nickel and copper, titanium sesquioxide, iodine, and butyl bromide isomers. The analyses of nickel and copper demonstrate the accuracy and limitations of the method; the temperature dependence of the parameters fit matched theoretical predictions, but offsets were present. Thus, the method as currently employed can correctly determine differences between related systems, but may yield values that have incorrect absolute magnitudes.

Titanium sesquioxide is known to undergo a second-order semiconductor-metal transition over a broad temperature range. At the onset of the transition, I have shown that the asymmetry of the PDF for the axial Ti-Ti jumped rapidly, suggesting that electron delocalization in that bond was increasing. This is in accord with theoretical predictions. Likewise, solid iodine showed much higher PDF asymmetry than iodine vapor, suggesting significant electron delocalization (by the mechanism of charge transfer) in the solid form. This is also in accord with theoretical predictions, although these predictions have not been universally endorsed. Finally, the C-Br bond in *t*-butyl bromide showed greater PDF asymmetry than either *n*-butyl bromide or *sec*-butyl bromide, which yielded similar values. This suggests the inductive effect is the dominant mechanism for stabilizing the C-Br bond; prior to this work, neither experiment nor theory has been sufficiently developed to provide this information.

The systems I have studied do not have much in common except some form of electron delocalization: they comprise molecular gases and network solids, conductors

and insulators, elements and compounds. Yet, within each set there is a marked increase in the radial asymmetry parameter with increased electron delocalization (as inferred from macroscopic phenomena). Although in each case an alternative explanation for the jump in radial asymmetry parameter can be imagined, I can think of no other single explanation for the common behavior of these disparate systems.

The utility of the technique is made clear by the information it provides about even long-known systems. The macroscopic and chemical consequences of electron delocalization are clear: copper conducts; gold shines, iron bends, and tertiary carbocations form more easily than primary. Theories of electron delocalization on multiple scales, such as band-structure and molecular-orbital theories, are successful and well established. Yet, there are still few direct probes of delocalization on a microscopic level. *Which* bond is responsible for the jump in conductivity of titanium sesquioxide? Does charge transfer take place in iodine? What mechanism stabilizes carbocations? Up until now, most attempts to address these questions have been based on comparing theoretical predictions or simulations with macroscopic observations. The result is that, when I began to believe that I had a method for identifying delocalization on an interatomic scale, I found a dearth of systems for which delocalization on this scale has been definitively described![12] Thus this work can be seen as not only providing a new technique for probing delocalization, but also providing additional evidence for certain theoretical descriptions (and not others!) of such common materials as iodine and alkyl halides.

---

[12] An obvious exception is the elemental metals, for which the local structure of electron delocalization is fairly uninteresting. As it turns out, the high symmetry of these metals prevents them from giving high radial asymmetry parameters.

Of course, that is not the ideal circumstance for demonstrating a new technique: with both the technique and the systems undergoing initial study uncertain, I was forced to make up for in variety what I lack in certainty. The eventual fate of my hypothesis will depend on its application to yet more systems; as the results continue to show consistency with theories of delocalization, my confidence in them grow. One obvious class of systems to investigate is the aromatics; in these compounds, the theory is so well established that there can be no doubt when and where electron delocalization is taking place. Unfortunately, EXAFS is difficult to perform on light elements such as carbon, and so I have been hunting for aromatics containing heavier elements. Just recently, I received permission from Dr. Graham George of Stanford University to analyze data he has collected on aromatic selenides, along with a non-aromatic control. I look forward to receiving this data and beginning this analysis.

Even once the validity of the technique is clearly established, progress must be made in EXAFS analysis in order to make it practical for routine analysis. Determinations of fine changes in the third cumulant stretch the limits of even state-of-the-art EXAFS techniques. The state-of-the-art is, however, rapidly progressing. Following is a list of some improvements that I plan to pursue in the future. The list is meant to be suggestive, rather than exhaustive.

- The origin of the systematic error in the third cumulant discovered in the analyses of nickel and copper must be discovered if this technique is ever to be applicable to truly novel materials. As it stands, comparison between similar compounds can be done, but it is not possible to say that a third cumulant is "high" without something to compare it to. My current suspicions

lie toward the isotropic potentials used by FEFF, but it is also possible that it is due to some defects in the samples or a bias in the least-squares minimization procedure.

- The details of the Fourier transform can be considerably improved. As discussed in Appendix A, the process of Fourier transforming the data produces a wildly varying amount of broadening, effectively at random. Improved windowing techniques could reduce this broadening to a predictable, consistent amount.
- Infrared spectroscopists often examine the second derivative of the Fourier transform, since this process transforms shoulders into discrete peaks. It is possible a similar technique would improve the resolution of overlapping scattering paths and reduce the incidence of false minima.
- Further study of well-characterized materials can improve the treatment of multiple scattering paths.
- As can be seen from the study of butyl bromide isomers in this work, the fitting of multiple spectra simultaneously can be improved. Weighting such that each spectrum contributes equally to the fit and statistics would be advisable.
- More can be done to utilize other structural probes. X-ray diffraction is already used to provide approximate atomic positions. Can the Debye-Waller factors from X-ray diffraction be used to constrain the second cumulant of distant shells? Likewise, infrared and Raman spectroscopies can sometimes be

used to find Einstein temperatures for particular bonds, which can in turn be used to constrain the second cumulant in EXAFS fits.

As these avenues are pursued, the precision and accuracy of EXAFS analysis will improve. Even modest improvements, combined with the results of this work, will provide a powerful new probe of electron delocalization in many materials.

Appendix A

FOURIER TRANSFORMS

A.1 Fourier transforms of finite, discrete data sets

In theory, the Fourier transform used in EXAFS has nearly the ordinary form, except for the conjugate variable being $2r$ and the integral being limited to nonnegative values of k.:

$$\tilde{\chi}(r) = \frac{1}{\sqrt{2\pi}} \int_0^\infty \chi(k) e^{i2kr} dk \qquad \text{(A.1)}$$

In practice, however, several significant modifications must be made.

Most obviously, in order to compute the integral shown in equation A.1, an infinite amount of data must be collected, both because the upper limit of the integral extends to infinity and because the integration implies a continuous function.

In order to examine the effect of limited data on the transform, consider a $\chi(k)$ which is perfectly harmonic and periodic:

$$\chi(k) = \cos(ak) \qquad \text{(A.2)}$$

The continuous Fourier transform of this function is a delta function at $2r = a$.

Mathematically, using a discrete Fourier transform is equivalent to multiplying the continuous $\chi(k)$ by a sampling function which is one when $k = n\Delta k_{\min}$ and zero otherwise, where n is an integer and $\Delta k_{\min}$ is the spacing between data points in k-space. The Fourier transform of this sampling function is a set of delta functions with spacing $\frac{\pi}{\Delta k_{\min}}$. Since the Fourier transform of a product is the convolution of the Fourier transforms, the discrete Fourier transform of (A.2) is also periodic in r-space with this frequency. In effect, this limits the range of r-space that contains unique data (the

symmetry of the function reduces this by an additional factor of 2). AUTOBK interpolates the data on to a k-grid of 0.05 $Å^{-1}$, giving a maximum value of r of more than 30 Å. Since this is greater than the typical mean free path of an EXAFS photoelectron, this is not a significant limitation.

Likewise, using a finite range of k-space Δk for the transform is equivalent to multiplying the infinite $\chi(k)$ by a "boxcar" function which is one within Δk and zero otherwise. The Fourier transform of this function is $\mathrm{sinc}(k\Delta k) = \frac{\sin(k\Delta k)}{k}$. Convoluting this function with a delta function leads to a sinc function centered on the position of the original delta function. This function is infinite in extent, non-monotonic, and continuous. In one sense, this truncation effect does not impact the validity of the curve-fitting analysis, since it has an equal effect on the data and on the theoretical standard. Nevertheless, it is highly significant to EXAFS analysis, since even a very sharply peaked PDF will lead to a somewhat broadened peak in the Fourier transform, and since scattering paths will contribute to the transform at values of r considerably removed from the actual absorber-scatterer distance. Therefore scattering paths at similar distances will be difficult to resolve, and fits for scattering paths limited to a range of r-values will be influenced by paths considerably outside of that range.

Of course, this analysis still treats $\tilde{\chi}(r)$ as continuous, when in fact it is also discrete. Since the actual $\tilde{\chi}(r)$ calculated by a computer is the continuous $\tilde{\chi}(r)$ multiplied by a sampling function, it follows that the discrete $\tilde{\chi}(r)$ is actually the Fourier transform of a periodic function extending to all k-space, even though the original data was over a finite range of k-space.

Finally, the fast Fourier transform (FFT) algorithm commonly used for computing discrete Fourier transforms requires a number of discrete points in $\chi(k)$ that is an integer power of 2. AUTOBK and FEFFIT address this by padding the data with enough zeroes to yield the desired number of points. Although according to equation A.1 this operation should not alter the transform, when the effects discussed above are taken into account, this can have a considerable effect.

As an illustration of these effects, Figure A.1a shows the FFT of $\chi(k) = \cos\left(3\frac{2\pi k}{\Delta k}\right)$, with 64 points sampled in k-space. Perhaps surprisingly in light of the above discussion, the FFT is remarkably uncomplicated: a single spike at the frequency of $\chi(k)$. The periodicity introduced by $\chi(k)$ sampling would be seen if the graph were extended far enough, but what about the broadening implied by the sinc function? In this case, the zeroes of the sinc function correspond exactly with the points at which $\tilde{\chi}(r)$ is sampled, and thus no broadening is observed. Figure A.2a shows the FFT of $\chi(k) = \cos\left(3.5\frac{2\pi k}{\Delta k}\right)$. Now, since the points at which $\tilde{\chi}(r)$ is sampled correspond to maxima in the sinc function, the broadening is highly evident. There is an alternate way of interpreting the difference between the two Fourier transforms. Since $\tilde{\chi}(r)$ is discrete, its inverse Fourier transform is periodic; in effect, the original $\chi(k)$ is repeated in a periodic fashion. In Figure A.1a, $\chi(k)$ has an integral number of periods in Δk, and is thus periodic with a single frequency (see Figure A.1b). In Figure A.2a, however, $\chi(k)$ has a half-integral number of periods in Δk, so when it is made periodic it has a discontinuity that requires other frequencies in the Fourier transform to generate (see Figure A.2b). Now, consider the function $\chi(k) = \cos\left(3\frac{2\pi k}{\Delta k}\right)$, but with 60 points in k-space sampled. In

order to reach an integer power of 2, four points with value of zero must be added. If a continuous Fourier transform were applied, there would of course be no difference between this case and the first one examined. When the periodicity introduced by the sampling in *r*-space is considered, however, *two* discontinuities have been introduced into the function (see Figure A.3b). The Fourier transform (Figure A.3a) is thus considerably more complex than in Figure A.1a.

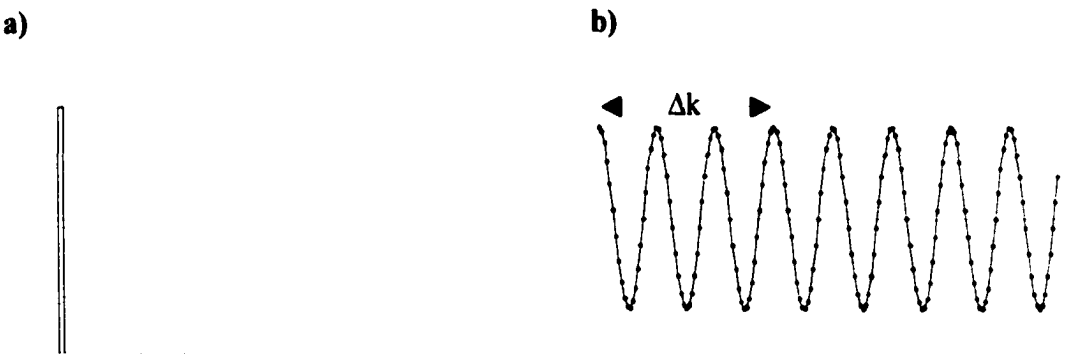

Figure A.1: a) Discrete Fourier transform of $\chi(k) = \cos\left(3\frac{2\pi k}{\Delta k}\right)$; b) Backtransform

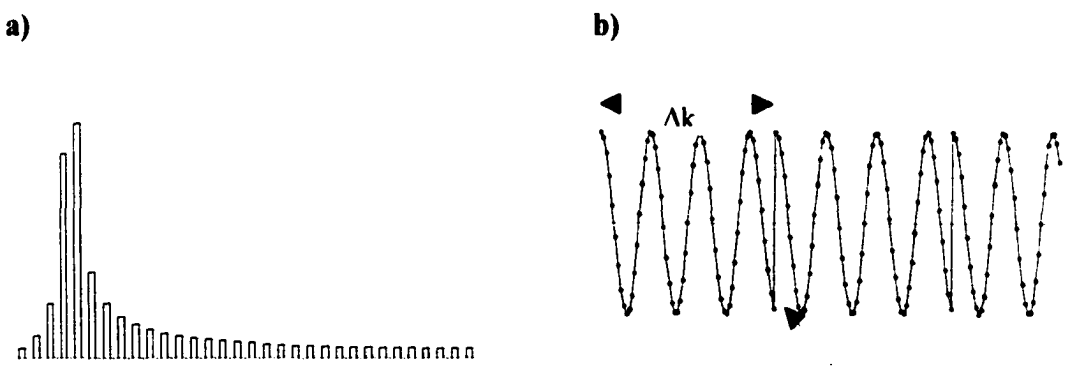

Figure A.2: a) Discrete Fourier transform of $\chi(k) = \cos\left(3.5\frac{2\pi k}{\Delta k}\right)$; b) Backtransform

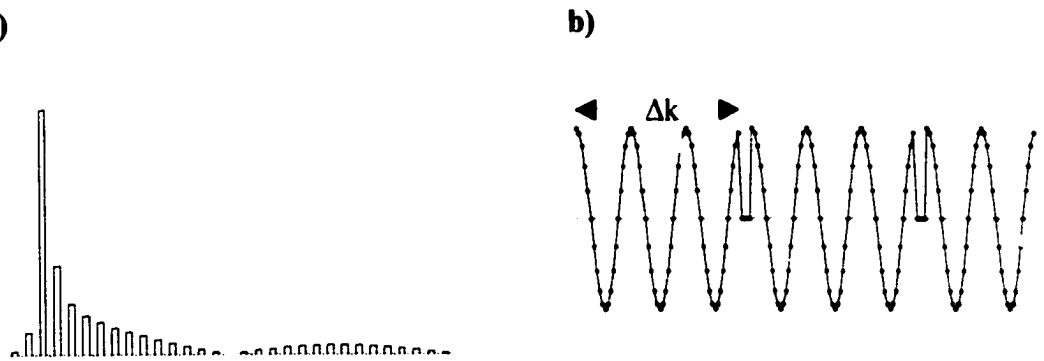

Figure A.3: a) Discrete Fourier transform of $\chi(k) = \cos\left(3\frac{2\pi k}{\Delta k}\right)$ padded with zeroes; b) Backtransform

A.2 Windowing

In order to minimize the effects of the above factors, it is conventional to multiply $\chi(k)$ by a "softer" window function than the boxcar implied by simple truncation of the sampling range. If this window goes smoothly to zero (or nearly to zero) at the ends of the range, then discontinuities will be minimized and the Fourier transform relatively sharp. In EXAFS analysis, a very common window function is the Hanning window, given by:[13]

[13] In FEFFIT, the keyword kmin actually sets the value of $k_{min} + \Delta k_{win}/2$, and kmax $k_{max} - \Delta k_{win}/2$. This creates an error in FEFFIT's calculation of degrees of freedom; that error has been compensated for in this work. (The error is, in effect, a compromise. If someone using FEFFIT were to set their own ε rather than using FEFFIT's method for estimating it, the Hanning window would cause an overestimate of the degrees of freedom, while if FEFFIT's method was used, the degrees of freedom would be underestimated.

$$H(k)=\begin{cases}\sin^2\left[\dfrac{\pi\left(k-k_{\min}\right)}{2\Delta k_{win}}\right], & k_{\min}\le k<k_{\min}+\Delta k_{win}\\ 1.0, & k_{\min}+\Delta k_{win}\le k\le k_{\max}-\Delta k_{win}\\ \cos^2\left[\dfrac{\pi\left(k-k_{\max}+\Delta k_{win}\right)}{2\Delta k_{win}}\right], & k_{\max}-\Delta k_{win}\le k<k_{\max}\end{cases} \qquad \text{(A.3)}$$

The effect of the Hanning window (with $\Delta k_{win} = \Delta k/16$) on the padded function considered in Figure A.3 is shown in Figure A.4b. The severity of the discontinuities is somewhat tempered from the unwindowed function. This is confirmed in the Fourier transform (Figure A.4a), which shows noticeably less broadening.

a) **b)**

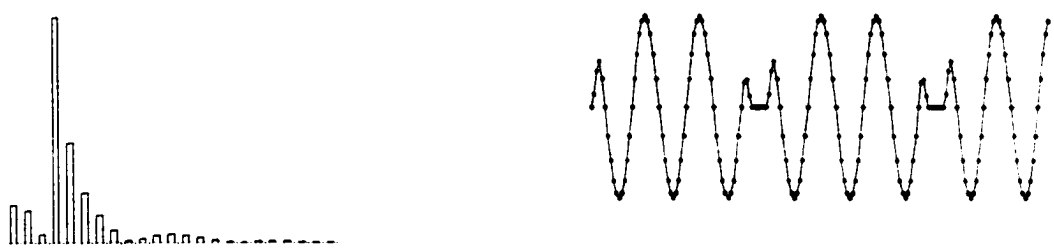

Figure A.4: a) Discrete Fourier transform of $\chi(k)=\cos\left(3\frac{2\pi k}{\Delta k}\right)$ padded with zeroes and windowed with a Hanning function; b) Backtransform

Another window in use is the Gaussian window, given by:

$$G(k)=\exp\left[-\alpha\left(\frac{2k-k_{\min}-k_{\max}}{k_{\min}+k_{\max}}\right)^2\right] \qquad \text{(A.4)}$$

Taking $\alpha = 2$ gives the result shown in Figure A.5b. Although this window does not quite go to zero at the limits, it does get quite small. This function does, however, have the virtue of being exceedingly smooth. The Fourier transform, shown in figure A.5a,

confirms this dramatically: the broadening is confined to a relatively narrow region of *r*-space.

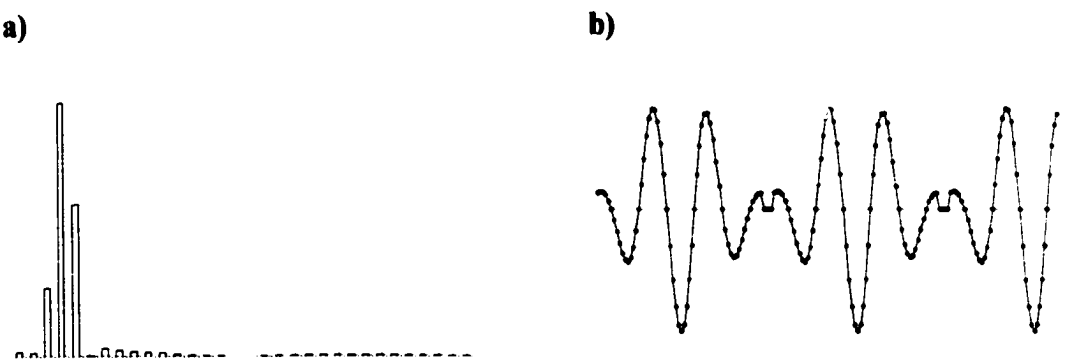

Figure A.5: Discrete Fourier transform of $\chi(k) = \cos\left(3\frac{2\pi k}{\Delta k}\right)$ padded with zeroes and windowed with a Gaussian function; b) Backtrans$\left(3\frac{2\pi k}{\Delta k}\right)$

Accordingly, I generally begin fitting with a Gaussian window. I always attempt to confirm fits with a Hanning window; a true fit should give compatible values under each. If both fits do yield similar parameters, I choose based on statistical quality-of-fit, correlations between variables, uncertainties in variables of interest, and similar criteria.

A.3 k-Weighting

In addition to broadening due to the finite, discrete character of $\chi(k)$, the EXAFS equation itself (3.11) contains terms that will reduce the periodicity of the signal, thereby increasing the complexity of the transform. In particular, two effects tend to decrease the amplitude of the signal as a function of k: the $\frac{1}{k}$ dependence of the pre-exponential, and the $-2k^2C_2$ term in the exponential. Transforming $k\,\chi(k)$, rather than $\chi(k)$ itself, removes the pre-exponential dependence, and, by making the signal more nearly periodic, leads to simpler Fourier transforms. The exponential damping is more difficult to counteract,

since C_2 is not known in advance. In general, a selection is made between multiplying $\chi(k)$ by k, k^2, and k^3. One criterion for choosing between these "k-weights" is to choose the one that most nearly gives a constant amplitude as a function of k.

The k-weight should ideally have no effect on the parameters found from a fit (but see Appendix D). When a fit is complete, the k-weight should always be changed to check for stability; if parameters remain the same (to within the uncertainty) when the k-weight is changed, then a greater confidence can be assigned to the validity of that fit. The final choice of k-weight is often based on the statistical quality of the fit produced, the correlations between variables of interest, and the uncertainties in those variables.

A.4 Statistical Effect of Windowing and k-Weighting

Since windowing reduces the magnitude of some portion of the data, it seems at first that it has the effect of reducing the amount of independent data, but this is not the case. FEFFIT estimates the uncertainty ε from the value of the transform above 15 Å. This noise can be reasonably expected to be drawn from all values of k, and thus will be weighted in exactly the same way as the average data point. The scaling of the data by a window (or, for that matter, by k-weighting) will have no systematic effect on the estimation of errors.

A.5 Suggestions for future development

If, instead of interpolating on to a grid with fixed spacing, the data were interpolated on to a grid with a fixed number of points, the number of points could be chosen to be an integer power of 2. This would decrease the amount of broadening in many cases, although, as can be seen from Figure A.2, windowing would still be necessary. Equally importantly, the current scheme produces an anomalous behavior as a function of the k-

range chosen for analysis: a very small change in the k-range could cause the number of grid points to increase from, say, 256 to 257. This change of one grid point would then require 255 zeroes to be padded on to the end of the function to bring it to the next integer power of 2. This massive change in the way the function was transformed could easily overwhelm the benefits of the single data point that was added. In some cases, this could mislead a person performing a fit into believing that high-*k* data was too noisy to improve the fit (or low-*k* data too strongly influence by the background). Interpolating on to a grid with a fixed number of points would remove this anomalous result of changing the *k*-range.

Appendix B

SAMPLE PREPARATION

In this study, all samples were powders and gases used in transmission. For this geometry, there are two primary considerations.

First, the sample must be neither too thin nor too thick. This is necessary to avoid a poor signal-to-noise ratio. If the sample is thin, the absorption is a small difference between large numbers (according to equation 3.6, the absorption is the difference between ln I_0 and ln I_t) , and random fluctuations in the ion chambers will overwhelm the signal. If the sample is too thick, then I_t is small, and Poisson statistics large fractional fluctuations in that quantity. It has been shown [53] that, considering only fluctuations due to counting statistics, the maximum signal-to-noise ratio is achieved when the sample is of a thickness such that[14] $\mu(E)x$ is 2-3 above the absorption edge (the precise value depends somewhat on the absorption due to the measurement of I_0). It should be noted that this is the desired absorption for the entire sample, as well as any other absorbing material between the two ion chambers (such as windows), not just the element being probed.

The other requirement is that the sample be as even as possible over the width of the beam. To see why, consider a sample with two different regions within the beam, one of thickness x_1 and area A_1, the other of thickness x_2 and area A_2. The intensity in each region obeys the usual Bouguer law:

$$I_{1t} = I_o e^{-\mu x_1} \tag{B.1}$$

[14] The difficulties with the multiple meanings of μ are particularly acute in this section: in exponentials and expressions such as this one, it is the absorption per unit length, while μ_{meas} is a total absorption. Sorry.

$$I_{2t} = I_o e^{-\mu x_2} \tag{B.2}$$

This gives a total intensity of

$$I = \frac{I_{1t}A_1 + I_{2t}A_2}{A_1 + A_2} = \frac{I_o}{A_1 + A_2}\left(A_1 e^{-\mu x_1} + A_2 e^{-\mu x_2}\right) \tag{B.3}$$

If the usual procedure is used, μ will be calculated to be:

$$\mu_{meas} = \ln\frac{I_o}{I_t} = \ln\left(\frac{I_o}{\frac{I_o}{A_1 + A_2}\left(A_1 e^{-\mu x_1} + A_2 e^{-\mu x_2}\right)}\right) = \ln\left(\frac{A_1 + A_2}{A_1 e^{-\mu x_1} + A_2 e^{-\mu x_2}}\right) \tag{B.4}$$

Now consider the ratio at two different energies

$$\frac{\mu_{meas}(E_2)}{\mu_{meas}(E_1)} = \frac{\ln\left(\frac{A_1 + A_2}{A_1 e^{-\mu(E_2)x_1} + A_2 e^{-\mu(E_2)x_2}}\right)}{\ln\left(\frac{A_1 + A_2}{A_1 e^{-\mu(E_1)x_1} + A_2 e^{-\mu(E_1)x_2}}\right)} \tag{B.5}$$

Since, unless $x_1 = x_2$, this ratio depends explicitly on A_1, A_2, x_1, and x_2, the shape of the EXAFS spectrum no longer reflects only the absorption coefficient μ, and any fit based on a theoretical standard must necessarily be incorrect.

The magnitude of the effect may be seen by substituting $x_2 = 2x_1$ and $A_1 = A_2 = 0.5A$. Then

$$\mu_{meas}(E) = \ln\left(\frac{A}{0.5Ae^{-\mu(E)x_1} + 0.5Ae^{-\mu(E)x_2}}\right) = \ln\left(\frac{2e^{\mu(E)x_1}}{1 + e^{-\mu(E)x_1}}\right) \tag{B.6}$$
$$= \ln 2 + \mu(E)x_1 - \ln\left(1 + e^{-\mu(E)x_1}\right)$$

If $\mu(E)x_1$ is large compared to ln 2, the fractional error becomes small suggesting using a thick sample can reduce this source of error. But if the absorption is too large, the signal-to-noise ratio becomes poor.

What about the small-absorption limit, in which $\mu(E)x << 1$? In that case, $\mu_{meas}(E)$ approaches $\frac{3}{2}\mu(E)x_1$, which is the absorption that would result from a uniform sample with the same average thickness, a reasonable result. But in EXAFS analysis it is not $\mu_{meas}(E)$ that is compared to the theoretical standard, but rather $\chi(k)$. The effect on this quantity is rather complex, and best illustrated by a numerical example. Suppose $\mu(E_2)x_1 = 2.10$ and $\mu(E_1)x_1 = 1.90$ (typical numbers for the maximum and minimum of an EXAFS oscillation). Then, using (B.4), $\mu_{meas}(E_2) = 2.68$ and $\mu_{meas}(E_1) = 2.45$. Assume that μ_{0meas}(post-edge) is approximately constant at a value halfway in-between, or 2.565 (if the sample had been all of thickness $\frac{3}{2}x_1$, μ_0(post-edge) would have been 3.00). Also suppose that for a sample of thickness $\frac{3}{2}x_1$, μ_0(pre-edge) = 1.5, so that (B.4) gives μ_{0meas}(pre-edge) = 1.38. Thus (3.1) becomes $\chi_{meas}(E_2) = \dfrac{2.68-2.565}{2.565-1.38} = 0.097$, while if the sample had all been of uniform thickness, the result would have been 0.100, implying a 3% error (the error in $\chi(k)$ is the same). Considering that this is the result when half of the sample is 100% thicker than the other half, I believe that small amounts of thickness inhomogeneity are not a major source of error.

Next, consider the effect of a pinhole, where $A_2 = 0.1A_1$ and $x_2 = 0$.

$$\mu_{calc}(E) = \ln\left(\frac{1.1A_1}{A_1 e^{-\mu(E)x_1} + 0.1A_1}\right) = \ln\left(\frac{11}{10e^{-\mu(E)x_1} + 1}\right) \qquad (B.7)$$
$$= \ln 11 - \ln\left(1 + 10e^{-\mu(E)x_1}\right)$$

This time, the effect is a bit different. For small absorption, the result is again the result expected for the average thickness, $\frac{10}{11}\mu(E)x_1$, but at large thicknesses, the calculated absorption approaches ln 11 (no matter how thick the sample is, intensity still travels through the pinhole). Again taking $\mu(E_2)x_1 = 2.10$ and $\mu(E_1)x_1 = 1.90$, (B.4) gives $\mu_{meas}(E_2) = 1.60$ and $\mu_{meas}(E_1) = 1.48$, with μ_{ocalc}(post-edge) = 1.54, while if while if μ_o(pre-edge) = 1.5, then μ_{ocalc}(pre-edge) = 0.85. This yields

$\chi_{calc}(E_2) = \frac{1.60 - 1.54}{1.54 - 0.85} = 0.087$, an error of 13%. Thus, pinholes tend to reduce the amplitude of EXAFS much more significantly than variations in sample thickness.

Therefore, it is desirable that samples be somewhat smooth over the width of the beam, taking special care to avoid pinholes, and have an absorption just above the edge of interest of 2-3.

Tabulated values of the absorption coefficient in cm^2/g are readily available [54, 55]. From this, a lower limit on the desired mass of the absorbing element can be found (A is the area of the sample perpendicular to the beam, m, ρ, and V are sample mass, density, and volume respectively):

$$2 = \mu\rho x$$
$$= \mu \frac{m}{V} x$$
$$= \mu \frac{m}{Ax} x$$
$$= \mu \frac{m}{A}$$

so that

$$m = \frac{2A}{\mu} \tag{B.8}$$

Using this formula, the following sample preparation protocol was developed:

- Determine minimum mass of sample needed using above formula.
- Use a mortar and pestle to grind sample to a chalk-like consistency.
- Prepare strips of Kapton tape of the desired area. This tape has an adhesive on one side. Measure the mass of the tape strips.
- Apply the sample in as thin a layer as possible on the adhesive side of a strip. Use a spatula or other device to even the sample and remove any excess material. This assures that no large particles remain. Determine the mass of the sample applied by weighing the tape again.
- Repeat with additional strips of tape until the total mass exceeds the amount desired. By exceeding the calculated target mass, the absorption will be between 2 and 3, as desired.
- Bind up the sample strips with another layer of Kapton and attach to a metal frame.

If the sample is sensitive to oxygen or water vapor, the entire procedure can be performed under nitrogen (or another gas, such as argon) in a glove box. In that case, the frame is sealed in a polyurethane ("Ziploc") bag while still in the glove box. The bag is then removed, heat sealed, and double-bagged for transport to the beamline.

The advantage of this method is that an even sample of the desired thickness is produced in a natural way. Although each strip is somewhat uneven and may have pinholes, the differences will tend to cancel out over multiple strips (typically, 3-6 tapes are required to reach the target mass). If the amount of sample required is particularly small, it can be diluted with carbon black so that it will take up more than one tape. At the beamline, a motor was generally used to move the sample through the beam so that a particularly even spot could be chosen. In most cases, transmission was constant across the width of the beam to 20% or better. To confirm the technique was producing sufficiently small particles, we compared samples prepared in this way to those using a molecular sieve; no difference in spectrum was found.

This was our standard protocol; differences for specific samples have been noted in the text where appropriate.

Appendix C

MULTIPLE SCATTERING

C.1 Multiple Scattering Paths and Constraints

The parameters associated with multiple-scattering paths are clearly not independent of those for direct-scattering paths, since any multiple-scattering path must be made up of some combination of direct paths. The decision of how to relate them is not trivial, however. Although one could imagine parameterizing all paths in terms of the Cartesian coordinates of the scattering atoms relative to the absorbing atom, this is generally not practical, since, although it makes constraint of the multiple-scattering paths straightforward, it will involve 3 parameters for each cumulant for each direct path. Instead, it is generally necessary to make some simplifying assumptions. Fortunately, EXAFS fits are relatively insensitive to the details of multiple-scattering parameterization; these paths generally give broad, low-amplitude contributions to the EXAFS signal. Although leaving out these contributions entirely will seriously affect the amplitude of the direct paths (and, to a lesser extent, the phase), a small phase shift or modest error in amplitude in the multiple-scattering path will have a second order effect. In fact, the most careful parameterizations of multiple-scattering paths sometimes give *no* benefit over a more approximate method. This is because of the approximation FEFF makes in assuming that $F_j(k,r)$ and $\delta_j(k,r)$ do not change significantly during the fitting process. For a direct-scattering path, this introduces only a small error, but for some multiple-scattering paths, such as "focused" paths that rely on a set of atoms being collinear (or nearly so), a small shift in one atom can change the amplitude dramatically. For this reason, high precision constraints on multiple-scattering paths are probably moot.

Nevertheless, there is middle ground between, for example, constraining all multiple-scattering paths to have the same cumulants and a detailed parameterization of bond angles, Debye-Waller ellipsoids, etc.. This appendix details the strategy used in this work.

C.2 Assumptions

The basic assumption of the constraint strategy used here is that the motion of all atoms is uncorrelated. This is evidently not true; x-ray diffraction Debye-Waller factors are different from EXAFS second cumulants (also generally referred to as Debye-Waller factors) precisely because atoms tend to move in tandem. But the largest coordination is for motion along the direction of a bonded pair. Atoms beyond the first shell or components of motion perpendicular to a bond are much less strongly coordinated. For the most part, these are the kinds of motion that must be combined for modeling multiple-scattering paths.

If the motion of the individual atoms are uncorrelated, then the second cumulants for each path segment should combine additively (according to the standard statistical rule that for adding uncorrelated data, the *variances* add, rather than the standard deviations).

In addition, the schemes used here generally treat each segment of a multiple-scattering path as if they were the same length.

C.3 Classification and Constraints for Multiple-Scattering Paths

The nomenclature used here is mostly my own. For the diagrams in this section, the absorbing atom is shown in black.

C.3.1 Double

Figure C.1: Double multiple-scattering path

In these paths, the photoelectron backscatters off a neighboring atom, returns to the absorbing atom, backscatters again to the same neighbor, and backscatters one more time to the absorbing atom. The constraint here is rigorous: the fractional change in the path length, $\frac{C_1}{r_0}$, is the same as for the corresponding direct path (or, put another way, C_1 is twice the value for the direct path). The second cumulant, on the other hand, is *four* times the value for the direct path. This is because, in the expression for the second cumulant $C_2 = \left\langle \left(r - r_0\right)^2 \right\rangle$, each r and r_0 are simply doubled. Likewise, the third cumulant should be multiplied by *eight* (2^3).

C.3.2 Conjoined

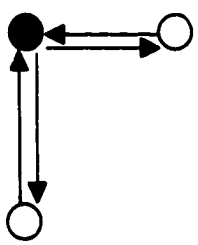

Figure C.2: Conjoined multiple-scattering path

The photoelectron again backscatters off a neighbor and returns to the absorbing atom, but it then backscatters off of a *different* neighbor before once again returning to the absorber. Two separate direct paths are traced in sequence; they may be degenerate. In this case, the fractional change in path length can be taken to be the average of the

fractional change for the two direct paths being conjoined (this uses the approximation that the paths can be treated as being the same length). The second cumulants for the two paths are added, under the assumption of uncorrelated atomic motion. Finally, I set the third cumulant to zero on these paths; these paths are generally fairly low amplitude, and the third cumulant is a small correction compared to the first two.

C.3.3 Focused

Figure C.3: Focused multiple-scattering path

This type of multi-scattering path requires at least three atoms that are collinear or nearly so. Regardless of how the individual legs of the paths are arranged, only the extreme atoms affect the path length significantly. Thus, these paths should have cumulants constrained to be the same as the cumulants for the direct path to the furthest scatterer. For materials in which large deviations from the theoretical model is expected, some caution must be used, as deviations from collinearity can substantially reduce the amplitude of these paths.

C.3.4 Triangle

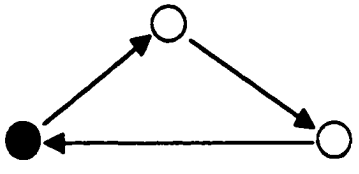

Figure C.4: Triangle multiple-scattering path

For this path, the photoelectron makes a loop around three atoms. This kind of path can be handled in either of two ways, depending on the identities of the scattering atoms. It is reasonable to approximate the fractional change in the distance by the average of the fractional changes of the two related direct absorber-scatterer paths (which may be degenerate). Likewise, it is reasonable to add the second cumulants for the two related direct paths (I will call this the "additive method"). The third cumulant is most safely set to zero, and probably will have little effect on the fit in any case.

If at least one of the scattering atoms is crystallographically equivalent to the absorbing atom, then the path can be viewed as a sum of three half-direct paths. The fractional change in the path length should then be set to the average of the fractional change of the three paths. The second cumulant requires a little care: for a half-direct path, the second cumulant is $\frac{1}{4}$ of the value for the equivalent direct path. This is, the inverse of the factor of four seen in the double path above. Then, using the assumption of uncorrelated motion, the second cumulants for the three half-paths can be added (the "segment method"). The third cumulant should again be set to zero.

It is worth noting that the two methods yield markedly different estimates of the second cumulant. Consider, for example, the case where all three segments are the same. The additive method would suggest that the second cumulant should be twice that of the corresponding direct path. The segment method would yield a value $\frac{3}{4}$ that of the direct path. There are two primary reasons for the difference, one statistical and one geometrical. The origin of the geometrical difference is that the additive method does not take account of the angle between the two scattering atoms. In fact, it is most appropriate for large bond angles. Since the case in which all three segments are the same implies a

60° bond angle, the additive method overestimates the second cumulant in this case. Statistically, the segment method takes the assumption of uncorrelated motion and applies it to each segment, rather than each atom. This is doubtless too extreme; even if the orthogonal motions of a given atom are independent, the segments in the above example are not orthogonal! Thus, this method underestimates somewhat the appropriate second cumulant.

In practice, triangle paths have low scattering amplitudes relative to the other types, so fits are particularly insensitive to which scheme is used. In fact, many researchers don't include triangle paths at all; since the difference between schemes for parameterizing the second cumulant can be 100%, this is not an unreasonable approach. Nevertheless, since the proper parameterization is probably between that given by the two techniques given here, either one will generally be somewhat of an improvement over nothing at all.

C.3.5 Flattened

Figure C.5: Flattened multiple-scattering path

Although this path looks superficially like the focused path, it originates on the middle atom. (Other authors do refer to both kinds of paths as focused, but they often require distinct constraint strategies.) If one of the scatterers is crystallographically equivalent to the absorbing atom, then it can be treated as a focused path originating at the scatterer.

If this is not the case, then the path is more closely allied with the triangle path type, and the additive technique is appropriate.

C.3.6 Reverse

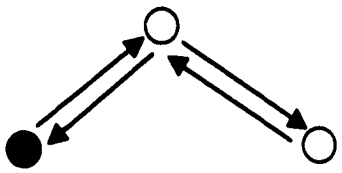

Figure C.6: Reverse multiple-scattering path

In this kind of path, the photoelectron travels from the absorber to one scatterer, then on to another, and then retraces its path. If the first scattering atom is crystallographically equivalent to the absorber, this can be handled as a conjoined path originating at the scatterer. If not, constraining it like the related triangle path is a reasonable approach, although the geometry is somewhat different. Fortunately, reverse paths are generally of low amplitude.

C.3.7 Other path types

Variants on the above types are occasionally encountered, but can generally be treated by similar approaches. Most high amplitude multiple-scattering paths fall into one of the above categories.

Appendix D

USING K-DEPENDENCE TO REDUCE CORRELATIONS

One of the difficulties inherent in analyzing EXAFS data by the curve-fitting method is the high correlations between certain fitted variables. As can be seen from equation 3.11, certain pairs of variables tend to have similar effects on a spectrum. The most common sets are those that dominate the determination of amplitude (S_0^2 and the second cumulants) and those that dominate the determination of phase (ΔE_0, the first cumulant, and the third cumulant). The correlations are most often between parameters affecting a single scattering path (usually the first and third cumulants for the same path) or between a parameter affecting a single path and a global parameter (S_0^2 and the second cumulant for a particular path or (ΔE_0 and the first or third cumulant for a particular path). Ironically, it is generally the path that contributes the most to the signal that shows the most persistent correlations; if the second cumulant of the most prominent path can be determined, for example, the value of S_0^2 tends to become easily fit, and the second cumulants of other paths then fall into place.

Several techniques have been used in this work to try to minimize these correlations:

- Where possible, values for correlated parameters are fixed. For example, the Ti-Ti bond lengths in titanium sesquioxide were fixed by temperature-dependent x-ray diffraction data.
- By fitting temperatures series simultaneously, S_0^2 and ΔE_0 could be constrained to be constant as a function of temperature. This often reduces substantially correlation with the temperature-dependent path parameters.

- Where practical, fits were extended in r-range. By including more paths, contributions between global and path-specific variables were reduced.

Nevertheless, high correlations often persisted, particularly when one path was a dominant contributor to the EXAFS spectrum. To address this, a technique based on the k-dependence of the parameters was used. This technique has been promoted by Ravel [56].

The idea of this technique is that the k-dependence of correlated variables is generally quite different: the first cumulant's effect on the phase appears weighted by k in the EXAFS equation, the second cumulant's amplitude effect by k^2, the third cumulant's phase effect by k^3, and the effect of S_0^2 is independent of k. Therefore emphasizing different regions of k-space should cause the parameters to contribute to the fit in different proportions. A simple way to accomplish this is to change the k-weighting (Appendix A).

Using this idea, the following analysis protocol is used for pairs of correlated variables:

- One of the correlated variables is set to a specific value, and fits then performed at k-weights 1, 2, and 3. The values obtained for the other correlated parameter are recorded.
- The previous step is repeated for different values of the first variable over a range encompassing its probable values; typically 0.6 to 1.1 for S_0^2 and -10 eV to 10 eV for ΔE_0.

- For each *k*-weight, the results are graphed and best-fit lines drawn through the points.
- Generally, the three lines intersect at or near a single point. Since the correct values for the parameters should be independent of *k*-weight, this point represents the true fit, and the value of the controlled parameter at that point can be taken as correct. With three lines, there will generally be multiple intersections over a small region; the spread between these intersections can be used to estimate the uncertainty.
- The controlled parameter is now constrained to its value at the intersection point, and the fitting procedure proceeds normally.

For example, S_0^2 and the second cumulant for the nearest-neighbor in nickel were highly correlated in preliminary fits. Figure D.1 shows the protocol described above applied to these two variables. In Figure D.1a, it can be seen that the second cumulant found is independent of *k*-weight when S_0^2 is approximately 0.88, so S_0^2 was constrained to that value for the remainder of the fitting process. As can be seen from Figure D.1b, intersections between the three lines actually begin at 0.873 and continue through 0.882. Thus, S_0^2 is reported as 0.88(1).

a)

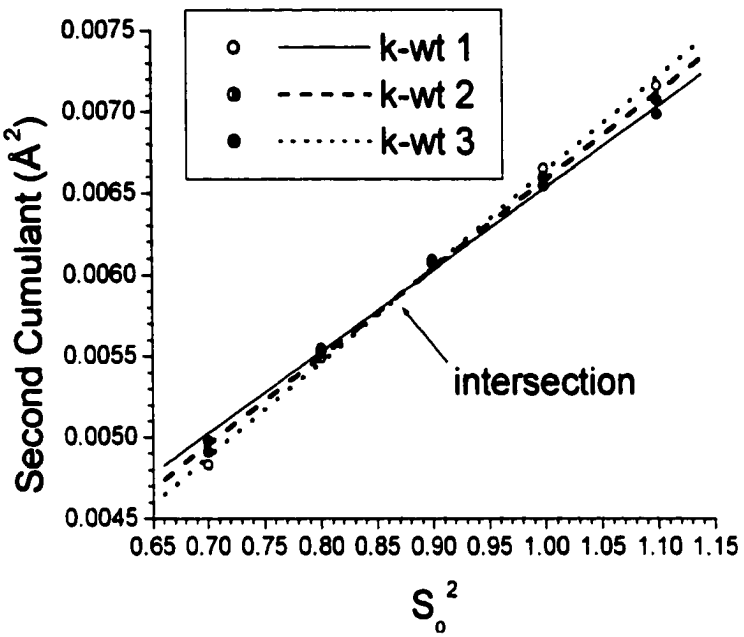

b)

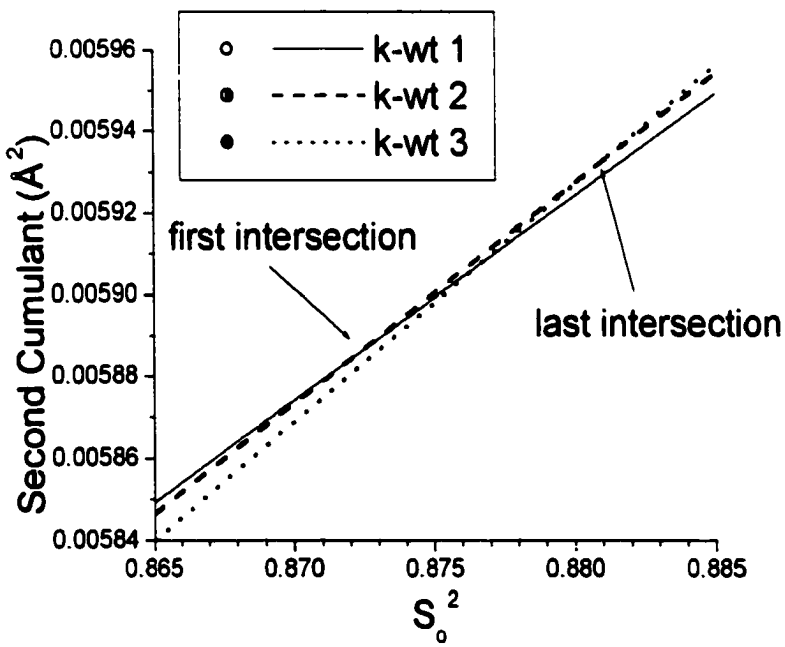

Figure D.1: Correlation chart for S_0^2 vs. nearest-neighbor second cumulant (nickel)

BIBLIOGRAPHY

1. J. C. Scott, *Science* **278**, 2071 (1997).

2. K. P. C. Vollhardt & N. E. Schore, *Organic Chemistry* 2nd ed., (W.H. Freeman, New York, 1994), P. 207.

3. Y. Apeloig, P v. R. Schleyer, J. A. Pope, *J. Am. Chem. Soc.* **99**, 5901 (1977).

4. R. S. Mulliken, *J. Am. Chem. Soc.* **74**, 811 (1952).

5. N. W. Ashcroft & N. D. Mermin, *Solid State Physics*, (Harcourt Brace, Fort Worth, 1976), Ch. 25.

6. W. H. McMaster, K. Kerr-Del Grande, J. H Mallett, & J. H. Hubell, *Compilation of X-ray Cross Sections, Lawrence Laboratory Report UCRL-50174* (National Bureau of Standards, Springield VA, 1969).

7. J. J. Rehr, J. Mustre de Leon, S. I. Zabinsky, & R. C. Albers, *J. Am. Chem. Soc.* **113**, 5135 (1991).

8. B. D. Ravel, Ph.D. thesis, University of Washington, 1997.

9. P. Bouguer, *Essai d'optique sur la gradation de la lumiere*, Paris (1729).

10 . A. L. Ankudinov *et al.*, *Phys. Rev.* B **58**, 7565 (1998).

11. J. J. Rehr, E. A. Stern, R. L. Martin, & E. R. Davidson, *Phys. Rev.* **B 17**, 560 (1978).

12. E. A. Stern, B. A. Bunker, & S. M. Heald, *Phys. Rev.* **B**, 5521 (1980).

13. J. J. Rehr & R. C. Albers, *Rev. Mod. Phys.* **72**, 621 (2000).

14. M. G. Newville, Ph.D. thesis, University of Washington, 1995.

15. M. Newville *et al.*, *Phys. Rev.* B **47**, 14126 (1993).

16. M. Newville *et al.*, *Physica* **B 208&209**, 154 (1995).

17. http://cars9.uchicago.edu/~newville/feffit, accessed August 1, 2001.

18. J. J. Rehr *et al.*, *Phys. Rev.* **B 49**, 12347 (1994).

19. G. Bunker, *Nucl. Instrum. & Methods* **207**, 437 (1983).

20. M. Newville, FEFFIT documentation, available at http://cars9.uchicago.edu/~newville/feffit, accessed August 1, 2001.

21 . E. A. Stern, *Phys. Rev.* **B 48**, 9825 (1993).

22. T. Miyanaga & T. Fujikawa, *J. Phys. Soc. Japan* **63**, 1036 (1994).

23. N. Van Hung, & J. J. Rehr, *Phys. Rev.* B **56**, 43 (1997).

24. A. Frenkel *et al.*, *Phys. Rev. Lett.* **71**, 3485 (1993).

25. A. J. Frenkel & J. J. Rehr, *Phys. Rev.* **B 48**, 585 (1993).

26. G. Dalba, P. Fornasini, R. Grisenti, & J. Purans, *Phys. Rev. Lett* **82**, 4240 (1999).

27. E. A. Stern, D. E. Sayers, and F. W. Lytle, *Phys. Rev.* **B 11**, 4836 (1975).

28. E. A. Stern, P. Livins, & Z. Zhang, *Phys. Rev.* **B 43**, 8850 (1990).

29. T. Yokoyama, K. Kobayashi, T. Ohta, & A. Ugawa, *Phys. Rev.* **B 53**, 6111 (1996).

30. T. Yokoyama, Y. Yonamoto, T. Ohta, & A. Ugawa, *Phys. Rev.* **B 54**, 6921 (1996).

31. Y. Soldo *et al.*, *Phys. Rev.* **B 57**, 258 (1998).

32. G. Dalba *et al.*, *Phys. Rev.* **B 58**, 4793 (1998).

33. H. E. Swanson & E. Tatge, *Acta Cryst.* 7, 464 (1954).

34. H. E. Swanson & E. Tatge, *Nat. Bureau of Stand. Circ.* **359**, 1 (1953).

35. L. A. Girifalco & V. G. Weizer, *Phys. Rev.* **114**, 687 (1959).

36. F. Milstein, *J. Appl. Phys.* **44**, 3825 (1973).

37. K. Mohammed *et al.*, *Phys. Rev.* **B** 29, 3117 (1984).

38. A.F. Wells, *Structural Inorganic Chemistry*, 5th Edition (Oxford University Press, New York), (1984).

39. J. B. Goodenough, *Phys. Rev.* **117**, 1442 (1960).

40. R. A. Neiser, J. P. Kirkland, W. T. Elam, and S. Sampath, *Nucl. Instrum. & Methods* In *Phys. Res.* **A 266**, 220 (1988).

41. C. E. Rice & W. R. Robinson, *Materials Research Bull.* **11**, 1355 (1976).

42. C. E. Rice & W. R. Robinson, *J. Solid State Chem.* **21**, 145 (1977).

43. P. A. Cox, *Transition Metal Oxides* (Oxford University Press, New York, 1992), p. 238.

44. J. M. Honig & T. B. Reed, *Phys. Rev.* 174, 1020, (1968).

45. Y. Fujii *et. al.*, *Phys. Rev. Lett.* **58**, 796 (1987).

46. F. von Bolhuis, P. B. Koster, T. Migchelsen, *Acta Cryst.* **23**, 90 (1967).

47. A. Anderson and T. S. Sun, *Chem. Phys. Lett.* **6**, 611 (1970).

48. N. Muller and R. S. Mulliken, *J. Am. Chem. Soc.* **80**, 3489 (1958).

49. T. Laube & T. Ha, *J. Am. Chem. Soc.* **110**, 5511 (1988).

50. J. I. Brauman & L. K. Blair, *J. Am. Chem. Soc.* **92**, 5986 (1970).

51. E. E. Carpenter (private communication).

52. K. W. Egger & A. T. Cocks, *Helv. Chim. Acta* **56**, 1516 (1973).

53. P. A. Lee, P. H. Citrin, P. Eisenberger, & B. M. Kincaid, *Rev. Mod. Phys.* **53**, 769 (1981).

54. *CRC Handbook of Chemistry and Physics*, 75th edition, edited by D. R. Lide, (CRC Press, Boca Raton, 1994), p. 10-282.

55. E. M. Gullickson, *X-ray Data Booklet*, 2nd ed. (Lawrence Berkeley National Lab, Berkeley CA, 2001), p. 1-38.

56. B. D. Ravel, *EXAFS Analysis with FEFF and FEFFIT Part 2: Commentary* (unpublished).